Document Number:H2020-ICT-52/RISE-6G/D6.4

Project Name:

Reconfigurable **I**ntelligent **S**ustainable **E**nvironments for **6G** Wireless Networks

(RISE-6G)

Deliverable D6.4

Sustainable RIS solutions design for EE, EMFEU and SSE (Final Specifications)

Date of delivery:	30/09/2023	Version:	VF
Start date of Project:	01/01/2021	Duration:	36 months

Deliverable D6.4

Sustainable RIS solutions design for EE, EMFEU and SSE (Final Specifications)

Project Number:	101017011
Project Name:	**R**econfigurable **I**ntelligent **S**ustainable **E**nvironments for **6G** Wireless Networks

Document Number:	H2020-ICT-52/RISE-6G/D6.4
Document Title:	Sustainable RIS solutions design for EE, EMFEU and SSE (Final Specifications)
Editor(s):	D.-T. Phan Huy (ORA)
Authors:	R. Ibrahim, D.-T. Phan Huy, P. Ratajczak, Y. Yu (ORA) N. Awarkeh, S. Jeong, M. Di Renzo (CNRS) G. Gradoni, G. Tanner (UNOT) L. Bastianelli, E. Colella, V. Mariani Primiani, F. Moglie (CNIT) E. Calvanese Strinati, F.-E. Fairod, M. Merluzzi (CEA) H. Guo, T. Svensson (CHAL) R. Kotaba, P. Popovski (AAU) G. C. Alexandropoulos, K. D. Katsanos (NKUA). M. Crozzoli, D. Micheli (TIM)
Dissemination Level:	PU
Contractual Date of Delivery:	30/09/2023
Security:	Public
Status:	FINAL
Version:	VF
File Name:	RISE-6G_WP6_D6.4_final.docx

Abstract

In this deliverable, we summarize the final results of Task 6.2 on Sustainable RIS Solutions Design for EE, EMFEU and SSE and Task 6.3 on assessment methods of EE, EMFEU and SSE Improvements.

We present twenty solutions and innovations to boost the EE, EMFEU or SSE metrics and five new methods to assess these metrics.

Keywords

Beyond-5G; 6G; RIS; Secrecy, Security; EMF exposure; Energy-Efficiency

Contents

List of Figures

List of Tables

List of Acronyms

2D	Two-Dimension
3D	Three-Dimension
4G	Fourth Generation
5G	Fifth Generation
6G	Sixth Generation
AESR	Approximate Ergodic Secrecy Rate
AN	Artificial Noise
AO	Alternating Optimization
AP	Access Point
ARES	Autonomous RIS with Energy harvesting and Self-configuration
BA	Binary Amplitude
BC	Boundary Conditions
BF	Beamforming
BOA	Blue Optimization Algorithm
BRT	Battery Recharging Time
BS	Base Station
CDF	Cumulative Distribution Function
CPU	Central Processing Unit
CRKG	Channel Reciprocity-based Key Generation
CSI	Channel State Information
DFT	Discrete Fourier Transform
DL	Downlink
DMA	Dynamic Metasurface Antenna
E2E	End-To-End
ECSI	Eve's CSI
EE	Energy Efficiency
EH	Energy Harvesting
EIRP	Effective Isotropic Radiated Power
EMC	Electromagnetic Compatibility
EMF	Electromagnetic-Field
EMFE	Electromagnetic-Field Exposure

EMFEU	EMFE Utility
ER	Energy Receivers
FDTD	Finite-Difference Time-Domain
GNU	GNU Scientific Library
GPP	Ginibre Point Process
GSTCs	Generalized Sheet Transition Conditions
H2020	Horizon 2020
His	Hardware Impairments
H-PPP	Homogeneous Poisson Point Process
HRIS	Hybrid Reconfigurable Intelligent Surface
I	Intended
ICNIRP	International Commission on Non-Ionizing Radiation Protection
IoS	Internet of Surfaces
IoT	Internet of Things
IPD	Incident Power Density
I-PPP	Inhomogeneous Poisson Point Process
IU	Intended User
I-UE	Intended User Equipment
LOS	Line-of-sight
LP	Lorentzian-constrained Phase
MAC	Medium Access Control
MEC	Multi-access Edge Computing
MEH	Mobile Edge Host
MIMO	Multiple Input Multiple Output
MMIMO	Massive Multiple-Input Multiple-Output
mmWave	Millimeter Wave
MRC	Maximum Ratio Combining
MRT	Maximum Ratio Transmission
MU-MIMO	Multi-User MIMO
NI	Non Intended
NIU	Non Intended User
NI-UE	Non Intended User Equipment

NLOS	Non line-of-sight
OFDM	Orthogonal Frequency Division Multiplexing
P&P	Plug and Play
PEC	Perfect Electric Conductor
PHY	Physical
PL	Path Loss
PLS	Physical Layer Security
PP	Point Processes
PPP	Public Private Partnership
QoS	Quality-of-Service
RC	Reverberating Chamber
RFEH	Radio Frequency energy harvesting
RIS	Reconfigurable Intelligent Surface
SAR	Specific Absorption Rate
SE	Spectral Efficiency
SG	Stochastic Geometry
SINR	Signal-to-Interference-and-Noise Ratio
SNR	Signal-to-Noise Ratio
SoC	State of charge
SOP	secrecy outage probability
SSE	Secrecy Spectral Efficiency
TDD	Time Division Duplex
UE	User Equipment
UL	Uplink
UT	User Terminal
VNA	Vector Network Analyzer
WMAESR	Weighted Minimum Approximate Ergodic Secrecy Rate
WP	Workpackage
WPT	Wireless Power Transfer
ZF	Zero-Forcing
β-GPP	β-Ginibre Point Process

1 Introduction

RISE-6G is a 5th Generation (5G) Public Private Partnership Project (PPP) funded by the European Commission under the Horizon 2020 (H2020) framework. The project's vision hinges on the latest advances on reconfigurable intelligent surfaces (RISs) technology for radio wave propagation control, with the aim of improving this technology, and conceiving sustainable, programmable, and goal-oriented wireless environments, for the future 6th Generation (6G) networks. The main objectives of RISE-6G are: (i) the definition of novel architectures and control strategies incorporating multiple RISs; (ii) the study of the fundamental limits of the RIS technology based on realistic and validated radio wave propagation models; (iii) the design, by three different workpackages (WPs), of algorithmic frameworks based on RIS-empowered smart wireless environments providing enhanced connectivity and reliability (WP4), enhanced localization accuracy (WP5), and enhanced sustainability and security (WP6); (iv) the prototyping of the proposed innovation via two complementary trials with verticals. Deployment scenarios and use cases are defined by WP2.

Within RISE-6G, WP6 proposes innovative Physical (PHY) layer and Medium Access Control (MAC) layer technical enablers to improve the sustainability and security of wireless networks. More precisely, WP6 proposes solutions to boost the performance of wireless networks in terms of energy-efficiency (EE), electromagnetic field exposure utility (EMFEU), and secrecy spectral efficiency (SSE) metrics, as defined in Deliverable [D2.4]. WP6 aims at improving these metrics focusing on spatially localised areas. Such performance "boosted areas" have been defined in Deliverable [D2.3] and identified for various deployment scenarios and use cases listed in the same deliverable. It is expected that the EE, EMFEU, and SSE metrics require specific and novel network architectures and deployment strategies with RISs, as well as novel assessment methods of their consideration.

Current deliverable D6.4 provides the final results from WP6, on new PHY-MAC schemes with RIS to boost the EMFEU and SSE metrics defined in Deliverable [D2.4], for the use cases listed in [D2.3].

Current deliverable D6.4 also provides the final results from WP6, on new methods for the modelling and assessment of EE, EMFEU and SSE.

Note that current deliverable D6.4 is the final version of [D6.2]. Therefore, D6.4 does contain some text, already present and stable in [D6.2].

To summarize, the following concepts apply to both EMFEU- and SSE-boosted networks and guide the way we design our solutions:

- Radio waves are *desirable* at the position of an *intended* entity (device, user, person, or object), because this entity is receiving data from the network or is sensed by the network.
- Radio waves are *undesirable* at the position of a *non-intended* entity (device, user, person, or object) which can be either an *exposed* entity for which electromagnetic field exposure (EMFE) is undesirable, or an *eavesdropper* towards whom signal reception is undesirable.
- A *non-intended* entity (device, user, person, or object) can be either *not helping* or *helping* the network to boost the EMFEU or the SSE.
- In the case of EMFEU, the *helping non-intended* entity can help *intentionally* by participating to the protocol reducing the EMFE.
- In the case of SSE, the *non-intended* entity is always helping in a *non-intentional* manner. The network simply exploits an existing connection and the corresponding control information exchanged between the *non-intended* entity and itself.

1.1 Deliverable objectives & methodology

This document provides the final results from WP6, on **Task 6.2 and 6.3.**

In **Task 6.2,** we design **innovations in PHY-MAC layers** to reach the target objectives in the target "EE/EMFEU/SSE boosted areas". We also propose innovative schemes to optimize the trade-off between EE and EMFEU or the trade-off between EE and SSE, in the particular cases where EMFEU and/or SSE is improved at the expense of EE. We recall that the EE, EMFEU, SSE metrics and the boosted areas have been defined in [D2.3] (deployment scenarios and use cases) and [D2.4] (metrics), and [D6.1] (initial views on architecture and control signaling aspects).

The main objective of **Task 6.3** is to propose **new models** to assess the improvement in terms of EE, EMFEU and SSE brought by RISE networks based on advanced realistic models provided by WP3. To do so, we exploit our measurements of actual RIS (built by the project) and a true 5G Base Station (BS) in a Reverberating Chamber (RC), advanced modelling tools developed in WP3, Finite-Difference Time-Domain (FDTD) or Finite Elements simulations, and new mathematical frameworks, exploiting a Random Coupling Model (RCM).

Each of the proposed schemes (in Task 6.1) aimed at boosting EMFEU, is based on general principles explained in [D6.1] and recalled hereafter.

First of all, the control of EMFE towards humans, other living beings as well as certain objects that should have a limited EMFE needs to be reflected in specific protocol operations that take place in a RIS-aided communication system. In general, the communication system needs to differentiate between spatial points where the radiation is *desirable* and *undesirable*. The spatial points with *desirable* radiation are the ones occupied by an *intended* entity: an *intended* receiver (for instance held by an *intended user* of the communication link) that will receive the radio waves, an *intended* object or person that needs to be illuminated by radio waves in order to be sensed by the network. Hence, radio waves are *desirable* at the position of *intended* receivers, *intended* users and *intended* sensed humans or objects. At the spatial points with *undesirable* radiation, the EMFE needs to be kept below a certain value. The International Commission on Non-Ionizing Radiation Protection (ICNIRP) [ICN20][D6.1] provides recommendation regarding such threshold, based on the analysis of scientific studies. However, it can happen that some countries or cities adopt more constraining limits than the ICNIRP guidelines [GSMA]. Also, some use cases presented in [D2.3] and [D2.4] propose to provide "EMFEU boosted areas" as a service, for instance, in a Train Station. Therefore, **the threshold can be set arbitrarily low**, either by a city, a country, or a building owner. Note that according to the local regulation, the threshold usually must be ensured in a statistical sense (for instance on average and during a given pre-defined period) [ICN20]. The spatial points with *undesirable* radiation are the ones occupied by a *non-intended exposed* entity: a *non-intended exposed* user (a user of the communication network having subscribed to a low EMFE service), a *non-intended exposed* person or object. There are two main ways in which the communication system can detect and control *undesirable* EMFE at the *non-intended exposed* entity (user, person, or object), depending on the level of participation of *non-intended exposed* entity to the communication system protocol:

- The *non-intended exposed* entity is *not helping:* In this case the *non-intended* entity does not provide information about its positioning or status of EMFE, such that the communication system needs to infer it based on its own sensing capabilities, or by interfacing to application programming interface (APIs) and systems that can provide such information. For example, there could be a different system that measures room occupancy and based on that information the communication system can adjust the calculation of the induced EMFE.
- The *non-intended exposed* entity is *intentionally helping:* This is the case in which the *non-intended exposed* entity explicitly provides information to the communication system to assist the control of EMFE. For example, the device associated with a *non-intended exposed* user can use some of its signaling messages to indicate the level of EMFE or, simply, to make itself known to the communication system in order to force it to limit the EMFE at that spatial location. Such active methods for EMFE control may require dedicated protocol messages that can initiate certain action, such as change of the RIS pattern or decrease of the transmit power.
- Note that there could also be a non-intended exposed user helping non-intentionally (similarly as eavesdropper, i.e. limited to the control information).

Our proposed design solutions for boosted SSE are based upon the same general principles as for EMFEU boosting. Indeed, an *eavesdropper* is similar to a *non-intended exposed* user. Again, there are two main ways in which the communication system can detect and control *undesirable* signal at the *eavesdropper*, depending on the level of participation of the *eavesdropper* to the communication system protocol:

- The *eavesdropper* is *not helping:* In this case the *eavesdropper* does not provide information about its positioning or status of received signal, such that, as for the exposed user, the communication system needs to infer it based on its own sensing capabilities. In the worst case, i.e., without any knowledge regarding the eavesdropper, the network would simply try to reduce the level of signal in general; note that such eavesdropper is complex.
- The *eavesdropper* is *non-intentionally helping:* This is the case in which the *eavesdropper* is itself a User Equipment (UE), such as a smartphone, connected to the communication network. In this case, like any UE connected to the network, the eavesdropper exchanges data, control signals and pilots with the network. However, contrary to a normal UE, the eavesdropper tries to demodulate messages sent over radio resources allocated to another user equipment. To avoid such type of eavesdropping, the network could use pilot, control and data signals circulating between itself and the eavesdropper. In this case, the eavesdropper *non-intentionally helps* the network to improve its SSE; note that such eavesdropper is less complex as it is very close to a standard commercial device.

Figure 1-1 below illustrates the aforementioned concepts with one example where a RISE network emits radio waves with the Intended User as a target, in the presence of four Non-Intended entities:

1. A *Non-Intended User* who uses his/her UE (connected to the network) to *eavesdrop*; the network uses the connection with the *eavesdropper* to avoid eavesdropping, and thus the eavesdropper *unintentionally helps* the network.
2. A *Non-Intended User* who is *exposed* to the radio waves emitted by the RISE network, and who uses his/her UE (connected to the network) to *help intentionally*, the network to reduce his/her exposition.
3. A *Non-Intended* person, who is *exposed* to the radio waves emitted by the RISE network but is *not helping* the network to reduce his/her exposition.
4. A *Non-Intended* person, who uses a device (which is not connected to the network) to *eavesdrop*, *without helping* the network to prevent him/her from eavesdropping.

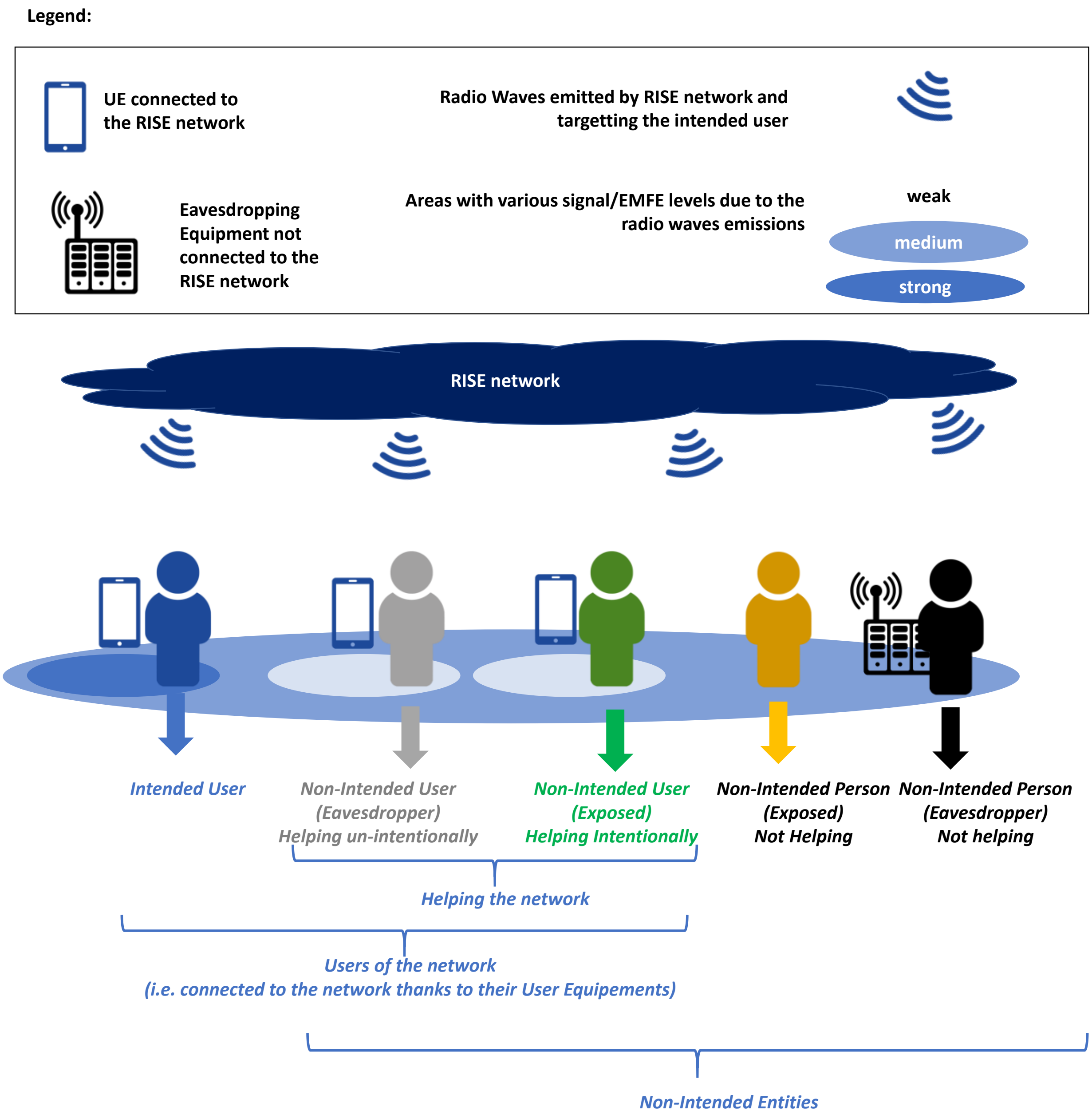

Figure 1-1 Example where the RISE network emits radio waves with the Intended User as a target, in the presence of four different types of Non-Intended entities (Figure extracted from [D6.1]).

Finally, we recall that there are two types of EMFE and EMFEU (as defined in [D2.4]):

- Inter-EMFE (**I-EMFE**): exposure of a Non Intended User to waves, in uplink (UL) or downlink (DL) transporting data for another Intended User. The corresponding utility metric is the Inter-EMFEU (**I-EMFEU**).

- Self-EMFE (**S-EMFE**): exposure of a User to waves (in UL or DL) transporting his/her own data (in this case the user is at the same time Intended and Non Intended). The corresponding utility metric is the Self-EMFEU (**S-EMFEU**).

1.2 Deliverable structure

The deliverable is organized as follows:

- In Section 2, for each of the various PHY-MAC solutions or innovations proposed by WP6, Task 6.2, to boost SSE or EMFEU, a brief description is provided.
- Section 3 provides progress status on new models, which were developed within Task 6.3.
- Section 4 concludes this deliverable.

2 Sustainable RIS Solutions Design for EMFEU and SSE

In this section, we summarize the work performed within Task 6.2. For each of the various contributions, the following brief description is provided:

- Introduction.
- System model.
- Results.
- Conclusion.

Note that, the proposed schemes have been identified to have an impact on the metrics of EE, EMFEU and SSE as defined in [D2.4].

All studied schemes of the project can be classified in the following six categories according to their main objectives:

- **Category A schemes boost the DL-EMFEU:** the network serves an intended user with downlink data. By doing so it exposes another non intended user to electromagnetic field (EMF). The **DL I-EMFEU** is defined as the ratio of the achieved SE at the intended user divided by the exposure of the non-intended user.
- **Category B schemes boost the UL I-EMFEU:** the intended user is transmitting data to the network in the UL. By doing so it exposes another non intended user to EMF. The **UL I-EMFEU** is defined as the ratio of the achieved SE at the intended user divided by the exposure of the non-intended user.
- **Category C schemes boost the S-EMFEU:** the intended user is transmitting data to the network in the UL. By doing so it exposes itself to its own EMF. The **S-EMFEU** is defined as the ratio of the achieved SE at the intended user divided by the exposure of the intended user.
- **Category D schemes boost the UL SSE:** the intended user is transmitting data to the network in the UL. An eavesdropper nearby intercepts the data. The **UL SSE** is defined as the difference between the SE at the intended user and the SE at the eavesdropper.
- **Category E schemes boost the DL SSE:** the network serves an intended user with downlink data. An eavesdropper nearby intercepts the data. The **DL SSE** is defined as the difference between the SE at the intended user and the SE at the eavesdropper.
- **Category F boost the DL EE:** the network serves an intended user with downlink data. The **DL EE** is defined as the SE at the intended user divided by the energy spent in the network.

Figure 2-1 below illustrates Categories A/B/C/D/F.

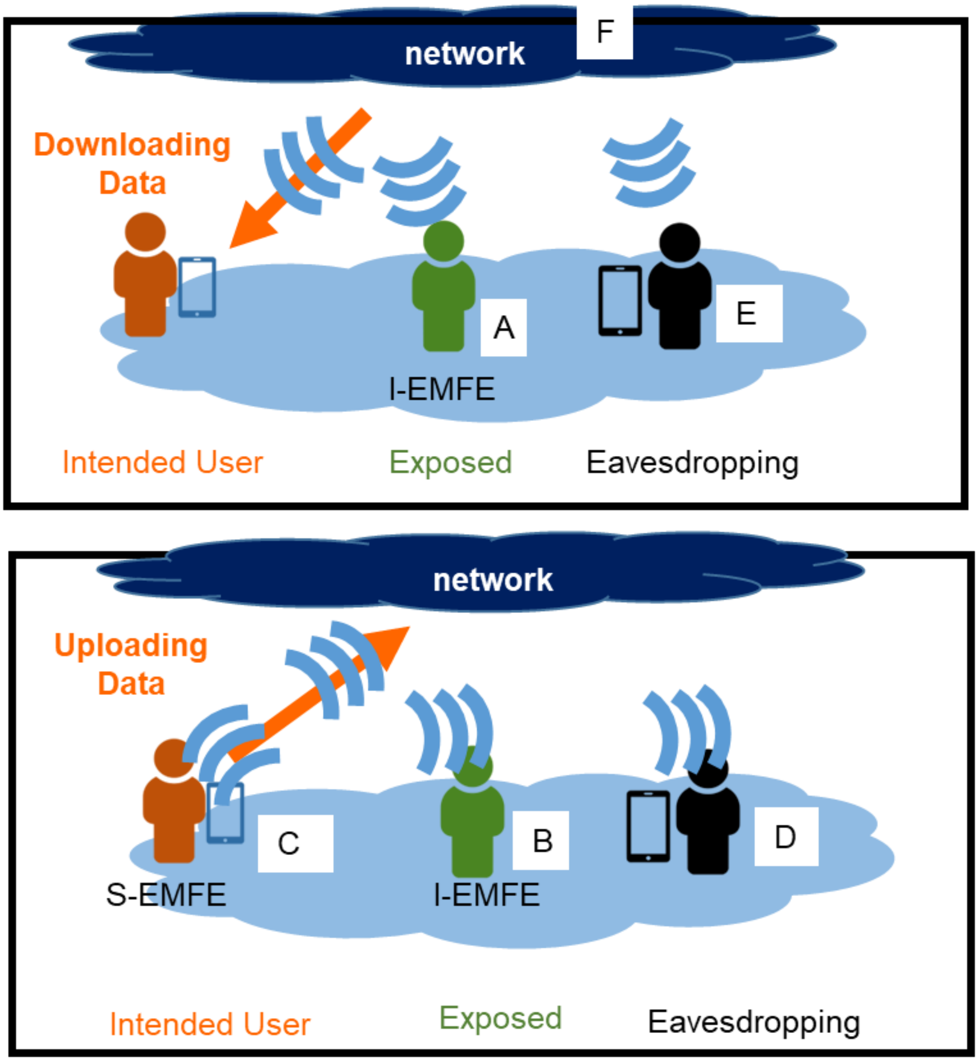

Category	Main Objective
A	Inter-EMFEU Boosting, DL
B	Inter-EMFEU Boosting, UL
C	Self-EMFEU Boosting & Device EE Boosting, UL
D	SSE Boosting, UL
E	SSE Boosting, DL
F	EE Boosting, Network

Figure 2-1 Categories (A/B/C/D/E/F) of WP6 proposed schemes.

Table 2-1 below lists all schemes proposed by the project.

For each scheme, a **boosting gain** in EMFEU, SSE or EE, due to the introduction of RIS is provided. This gain is the ratio of the value of the metric (EE, EMFEU or SSE) for the proposed **RIS-aided scheme** divided by the value of the metric for a reference scheme **without RIS**.

In some cases, the value of the metric for the reference scheme without RIS can be zero. In this case, the gain is **infinite**. EMFEU can typically happen to be zero when there is a very strong direct propagation path between the transmitter and the exposed person. In this case, the EMF constrain cannot be met, unless the transmitter does not transmit any data, i.e. unless the SE is zero. As the EMFEU is the ratio between the SE and the EMF constrain, in this case the EMFEU is zero as well. Similarly, SSE can typically reach zero when there is a very strong direct propagation path between the transmitter and the eavesdropper. In this case, the eavesdropper intercepts all the data, and the SSE is hence zero. In particular cases where the EMFEU gain is **infinite**, the RIS **enables a data communication under EMFE constrain, which would be impossible without RIS**. In particular cases where the SSE gain is infinite, the RIS **enables a secured communication, which would be impossible without RIS**. In these cases, we report **'enabler'** in the table below.

In some cases, the proposed scheme is an enabler, for with particular assumptions (such as position of the user, etc.), and a booster, with other assumptions. In this case, we report **'enabler'** and the **gain factor** in the table below.

#	Name	Enabler or boosting gain factor	Section, Reference(s)
Category A Schemes: I-EMFEU Boosting, DL			
A1	A Novel RIS-Aided EMF-Aware Beamforming (BF) Using Directional Spreading, Truncation and Boosting.	x2.05-x3.45	2.1.1 [APV21] [APV+22-1]
A2	A Novel RIS-Aided EMFE Aware Approach using an Angularly Equalized Virtual Propagation Channel.	x2.05-x3.45	2.1.2 [APV+22-2]
A3	EMF-Aware multi-user multiple input multiple output (MU-MIMO) BF in RIS-Aided Cellular Networks.	x1.07	2.1.3 [YIP22-1][YIP22-2]
A4	EMFE Avoidance thanks to Non-Intended User Equipment and RIS.	Enabler & x1.2	2.1.4 [GPHS22]
A5	EMFE Avoidance thanks to Non-collaborative Non-Intended User Equipment and RIS.	Enabler & x1.2	2.1.5 [GPHS23]
A6	EMF Exposure Mitigation in RIS-Assisted Multi-Beam Communications.	One order of magnitude	2.1.6 [SVK+23]
Category B Schemes: I-EMFEU Boosting, UL			
B1	Blue Communications for Edge Computing the RISs Opportunity.	x7	2.2.1 [AMC+22]
B2	Achievable offloading rate in RIS-assisted Multi-access Edge Computing (MEC) scenarios with power and EMF exposure constraints.	Up to >x4	2.2.2
Category C Schemes: S-EMFEU Boosting & Device EE Boosting, UL			
C1	EE Optimization of RISs with EMFE Constraints.	Enabler	2.3.1 [ZR22][ZRS+21]
C2	Creating and Operating Areas With Reduced Self-EMFE Thanks to RIS.	Enabler & x100	2.3.2 [PBH22]
Category D Schemes: SSE Boosting, UL			
D1	On Maximizing the Sum Secret Key Rate for RIS-Assisted Multiuser Systems.	Enabler	2.4.1 [LSX+22]
Category E Schemes: SSE Boosting, DL			
E1	Safeguarding multiple input multiple output (MIMO) communications with reconfigurable metasurfaces and artificial noise.	Enabler	2.5.1 [AKW+21]
E2	Counteracting eavesdropper attacks through RISs: A new threat model and secrecy rate optimization.	Enabler & x7	2.5.2 [AKW+23]
E3	Reconfiguring wireless environment via intelligent surfaces for 6G, Reflection, modulation, and security.	Enabler	2.5.3 [XYH+23]
E4	Surface-Based Techniques for Internet of things (IoT) Networks: Opportunities and Challenges.	x7	2.5.4 [ZRF+22]
E5	Spatial Secrecy Spectral Efficiency Optimization Enabled by RISs.	> x1.5	2.5.5 [KA23]
E6	Robust Transmission Design for RIS-assisted Secure Multiuser Communication Systems in the Presence of Hardware Impairments (His).	> x2.8	2.5.6 [PWP+23]
Category F Schemes: EE Boosting, Network side			
F1	EE maximization of Massive MIMO (MMIMO) communications with dynamic metasurface antennas.	> x1.75	2.6.1 [YXA+21-1][YXA+21-2]
F2	EE Maximization in RIS-aided Networks With Global Reflection Constraints.	x14	2.6.2 [FZR+23]
F3	ARES, Autonomous RIS solution with Energy Harvesting and Self-configuration towards 6G.	Enabler	2.6.3 [ADS+23]

Table 2-1 Summary Table of Proposed Schemes.

2.1 Category A: I-EMFEU Boosting in Downlink

2.1.1 A1: A Novel RIS-Aided EMF-Aware Beamforming (BF) Using Directional Spreading, Truncation and Boosting

The current sub-section summarizes a study that is detailed in [APV21] and [APV+22-1].

Introduction

MMIMO systems and adaptive BF enable mobile networks to deliver high throughput [MHM+18] [R+13]. As an example, a BS transmitting with its maximum power maximizes the received power and the delivered data rate at the target UE thanks to Maximum Ratio Transmission (MRT) BF scheme [L99] and a MMIMO antenna [VGT14]. Additionally, the regulation specifies a maximum EMFE threshold. This threshold must not be exceeded, beyond a limit region (typically a circle in environment without obstacles close to the BS), with a given probability or on average, during a time window, depending on the regulation. However, when the BS must serve the same user for a long period, in some cases, MMIMO and MRT BF could generate an over-exposed area exceeding the limit circle, in some directions, and cannot be used or deployed as such [TFC+17] [DTT16] [XZY+19] [PCE+18] [C+19] [CEA21]. As illustrated in Figure 2-2-a), these strong directions correspond to prime propagation paths between the antenna and the receiver. Also, we foresee that in the future, even arbitrarily larger limit circles and more stringent thresholds could be requested in the future by some cities. One simple solution to comply with the EMFE constraint consists in using a reduced transmit power at the BS (whilst keeping using MRT BF that ensures that the entire over-exposed area gets inside the circle, even in its strongest directions, and for a long period. Unfortunately, as illustrated in Figure 2-2-b), such a Reduced MRT BF scheme reduces the received power at the target UE and degrades the received Quality of Service (QoS). To overcome this drawback, we propose at first new EMF aware BF scheme, named Truncated MRT. It truncates the MRT BF radiation pattern, only in the directions where the over-exposed area would exceed the limit circle otherwise. The other directions already inside the circle are not impacted by the truncation. Compared to the Reduced MRT BF scheme, the Truncated MRT BF scheme uses a transmit power that is higher and delivers a received power at the target UE that is stronger, whilst remaining compliant with the EMFE constrain. To further improve the performance, we propose a second novel RIS-aided scheme, named Truncated and Boosted MRT BF scheme. As illustrated in Figure 2-2-d), this scheme boosts the remaining directions inside the circle until they meet the circle. Finally, to further enhance the performance of the aforementioned BF schemes, we propose to exploit the nascent concept of smart radio environments for the future 6G, by shaping the propagation environment itself (according to some Channel State Information (CSI)) thanks to RISs [R+19] [BRR+19] [S+21] [IEA+22] [ZR22] [R+21-1]. Note that in [IEA+22] [ZR22], RISs are used to reduce self-EMFE due to the smartphone UL, whereas we use RISs for EMFE reduction in the DL. More precisely, a RIS with continuous (instead of discrete) phase-shifting capability as in [R+21-1] [R+21-2] and sensing capability, first measures the propagation channel between the target UE and itself, and then, self-configures to 'turn itself electronically' in the direction of the target UE. Several sensing and self-tuning RISs of such type are deployed in the environment. Hence, without any communication with the RISs, MRT BF, Reduced MRT BF, and Truncated MRT BF schemes (all derived from MRT) naturally spread their radiation patterns in additional directions. As illustrated in Figure 2-2-a), b) and c), these directions are the directions of the RISs.

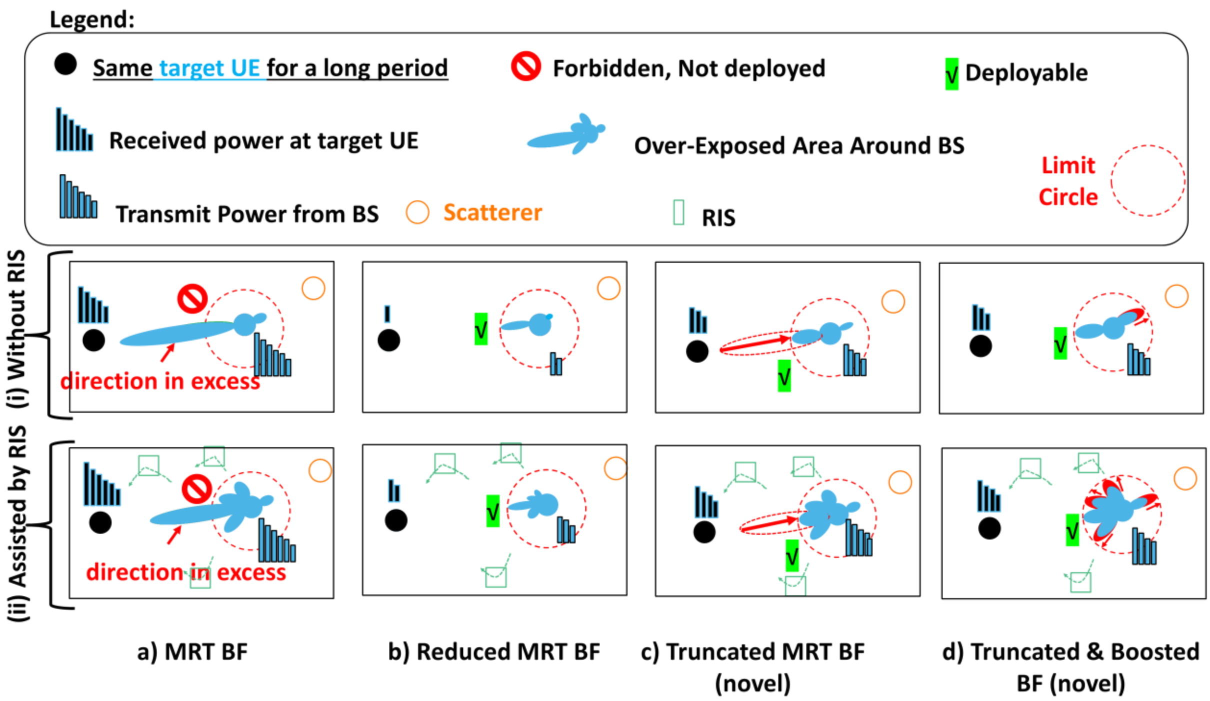

Figure 2-2 Studied BFs and corresponding over-exposed areas, assuming that the same UE is served by the BS for a long period.

System Model

In this study, we consider the DL data transmission between a MMIMO BS equipped with 64 antenna elements and a target UE. The BS is aided by 3 RISs randomly positioned, of 16 elements each. We consider a multipath propagation environment with 3 random scatterers. The propagation channel between the BS, the RIS and the target UE is modelled using the planar wave approximation, as illustrated in Figure 2-3-a). The propagation between the BS and a point Q close to the BS, is modelled using spherical waves, assuming free space propagation. As illustrated in Figure 2-3-b), the following two-step procedure applies:

- during the RIS Self-Configure procedure, the target UE sends pilots, and the RIS estimates the UE-to-RIS channel phases and self-configures its weight to “turn itself electronically” towards the UE.
- During the BS BF procedure, the target UE sends pilots again, and the BS estimates the UE-to-BS channel (under the influence of the RIS) and computes the MRT BF scheme.

The propagation between the BS and any point onto the limit circle is assumed to be perfectly known by the BS (for instance, thanks to previous measurements). Hence, knowing the BF precoder expression, the BS can predict the exposure onto the limit circle.

For reduced BF scheme, the BS uses the MRT BF scheme with a reduced transmit power ensuring that the EMFE target constraint is met onto the limit circle. For the truncated BF scheme, the BS projects the MRT BF scheme onto a codebook of Discrete Fourier Transform (DFT) beams to enable a per-beam (and per-direction) control of the radiation pattern of the BF precoder. Then, the BS truncates beams that exceed the limit circle. For the truncated and boosted BF scheme, the BS modifies the truncated BF precoder, by boosting the beams (directions) remaining inside the circle, until they meet the limit circle.

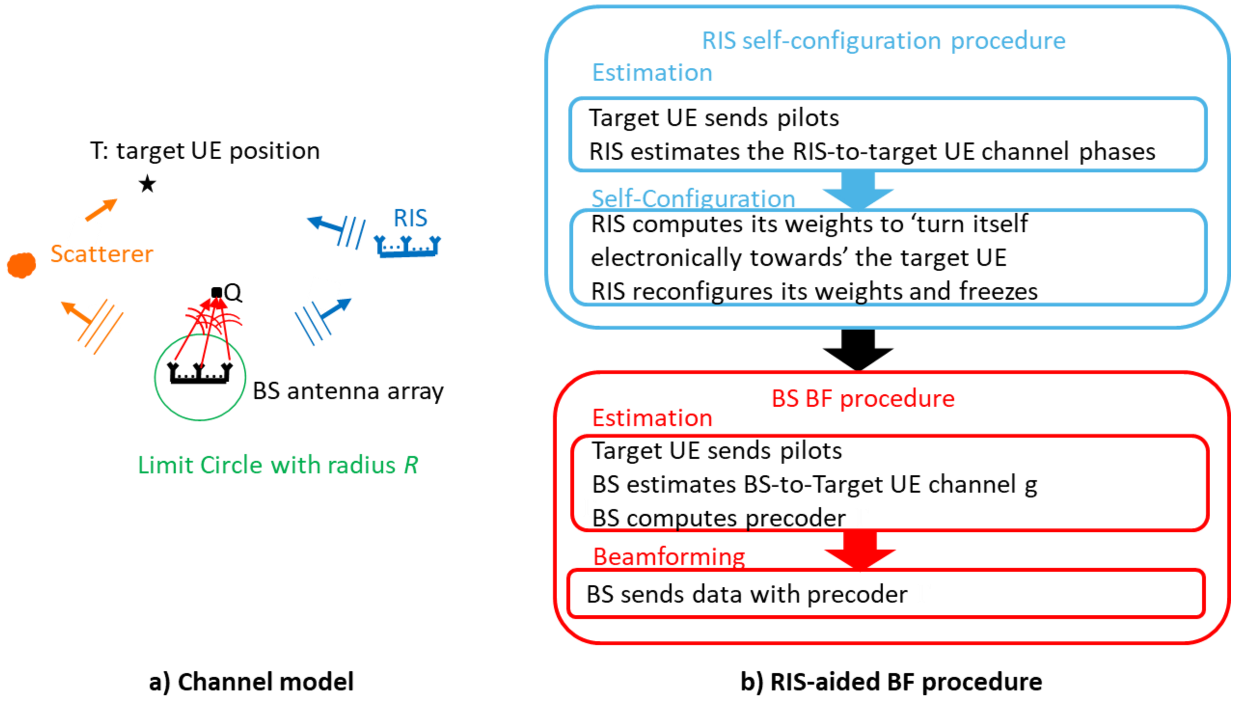

Figure 2-3 System Model.

The channel random parameters are drawn, and for each simulation sample, the following performance metrics are computed:

- The received power at the target UE.
- The BS transmit power.
- The percentage of positions exceeding the EMFE constraint beyond the limit circle (calculated inside a square surrounding the circle).

The mathematical details of the channel model and the procedures and simulation assumptions are provided in [APV21] and [APV+22-1].

Results

Figure 2-4 illustrates the statistics of the performance metrics introduced in 2.1.3, over random channels. Figure 2-4-a) illustrates the Cummulative Density Function (CDF) of the percentage of positions exceeding the EMFE constraint (assuming the same UE is targeted for a long period), beyond the limit circle. Figure 2-4-b) illustrates the CDF of the BS transmit power and Figure 2-4-c) illustrates the CDF of received power at the target UE. Performance with and without RIS assistance is plotted. MRT BF alone is not deployable. Reduced BF is compliant with the EMFE constrains but provides a low received power at the target UE. The Truncated and Boosted BF scheme maximizes the received power at the target UE and better matches the constrain. However, it uses a large transmit power at the BS side. The truncated BF scheme alone perfectly matches the constraint and is more energy-efficient. Detailed results and assumptions are available in [APV21] and [APV+22-1].

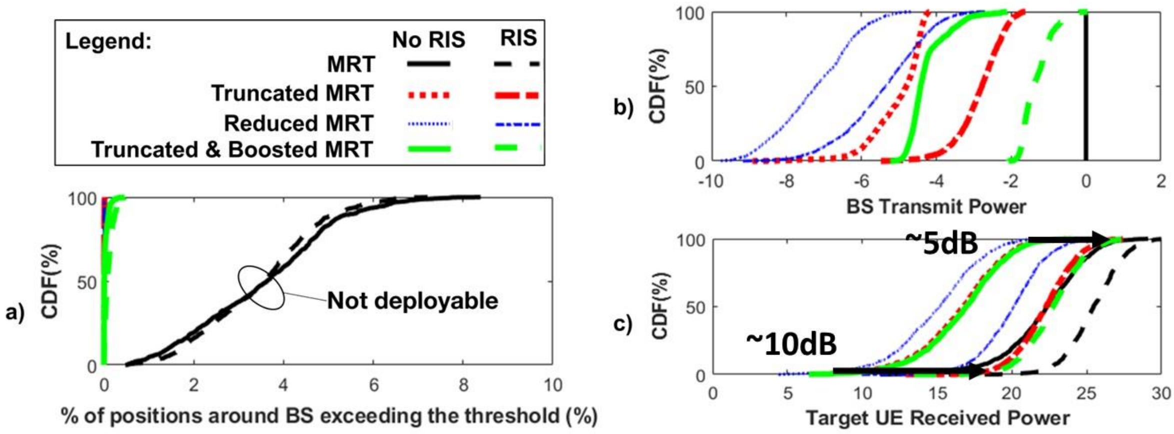

Figure 2-4 System Model CDFs of a) positions around BS (inside a square around the BS) exceeding the threshold b) BS transmit power and c) target UE received, assuming the same UE is targeted for a long period.

Compared to the reference Reduced BF scheme, the proposed Truncated and boosted scheme **boosts the received power at the target UE, by 5 to 10 dB**, under the same EMFE constrain. These statistical gains are obtained for a given average radio condition: i.e. a given average BS-to-UE channel power, a given average BS-to-RIS power, and a given average RIS-to-UE power target UE, and therefore a given average SNR. In these simulations, only the fast fading parameters vary in a random manner. Hence, if simulations were run with another average SNR, the same gains would be observed.

Assuming the target UE experiences the worse case SNR of 0dB with the reference Reduced BF scheme, it would reach a SE of 1 bit/s/Hz. With a received power gain of 10dB, the UE would reach a SE of 3.45 bit/s/Hz. With a received power gain of 5dB, the UE would reach a SE of 2.05 bit/s/Hz. Taking into account that these SEs are reached, under the same EMFE constrain, the **EMFEU minimum gain factor would be SE_min/SE_ref, i.e. a factor of x2.05 and the EMFEU maximum gain factor would be SE_max/SE_ref, i.e. a factor of x3.45.**

Conclusion

In this study, we propose two novel RIS-aided BF schemes called Truncated BF scheme and Truncated and Boosted BF scheme. They are built based on the projection of the MRT BF on the DFT codebook to allow truncation and boosting of individual beams (directions). We compare them to the MRT BF scheme (which is exceeds the EMFE constrain, when the same UE is targeted for a long period) and the Reduced MRT BF scheme (which delivers a poor received power at the target UE). Truncated BF scheme provides a better throughput than Reduced BF scheme, it perfectly matches the EMFE constrain, and it is more energy efficient than Truncated and Boosted BF scheme. **Therefore, the Truncated BF scheme boosts the I-EMFEU and the EE.** Compared to the reference Reduced BF scheme, the proposed Truncated and boosted scheme **boosts EMFEU by a factor of x2.05 to 3.45. This example of gain value is reported in the summary Table 2-1**.

2.1.2 A2: A Novel RIS-Aided EMFE Aware Approach using an Angularly Equalized Virtual Propagation Channel

The current sub-section summarizes a study that is detailed in [APV+22-2].

Introduction

In this study, we address the same problem as already presented in Section 2.2.1. However, we propose another novel RIS-aided BF scheme, named Equalized BF scheme, exploiting the channel sounding capability of the MMIMO BS [WK14][TP16][W+20] to provide high throughput under EMFE constraint. In this study, instead of the using the CSI of the true channel, to compute the MRT BF precoder, we propose to use the CSI of a virtual propagation. The virtual propagation channel is computed based on a sounding of the true channel. Compared to the true channel, the virtual channel, has the same scatterers, in the same directions. However, the virtual channel, is equalized in the angular domain: the path gain of all scatterers is set to 1. As a consequence, the radiation pattern of the MRT BF will also be equalized in the angular domain. The BS computes the transmit power to ensure that the EMFE constraint is met on the limit circle. The same self-configuring RISs as those used in Section 2.2.1 are added in the environment to spread the radiation pattern of the BS in the angular domain, and provide additional propagation paths in the environment, to reach the target UE. As illustrated in Figure 2-5, we compare the Equalized BF scheme to the MRT BF and the Reduced BF scheme (introduced in Section 2.2.1).

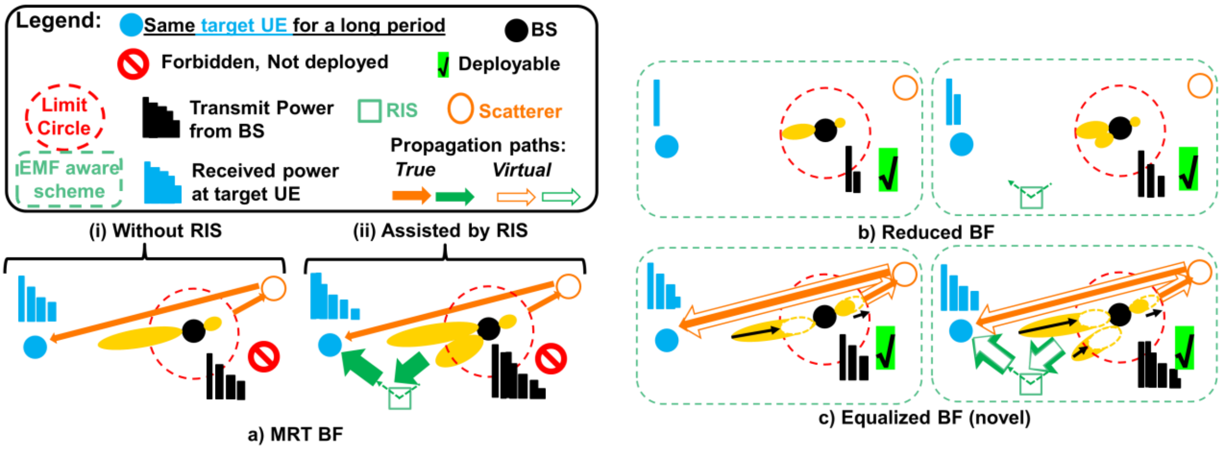

Figure 2-5 Studied BF schemes.

System Model

The same propagation model and RIS-aided BF procedures as in Section 2.1 are used. However, the RIS-aided BF procedure is slightly modified as follows, for the Equalized BF scheme. Instead of using the true CSI, the BS computes a virtual propagation channel as follows. As illustrated in Figure 2-6, the virtual propagation channel is computed based on a sounding of the true channel. Compared to the true channel, the virtual channel, has the same scatterers, in the same directions. However, the virtual channel, is equalized in the angular domain: the path gain of all scatterers is set to 1. As a consequence, the radiation pattern of the MRT BF will also be equalized in the angular domain. As in Section 2.1, the BS is assumed to perfectly know the channel between itself and locations on the limit circle. The BS therefore computes the transmit power to ensure that the EMFE constraint is met on the limit circle, with the Equalized BF precoder.

As in Section 2.1, the channel parameters are randomly drawn, and for each simulation sample, the following performance metrics are computed:

- The received power at the target UE.

- The BS transmit power.
- The percentage of positions exceeding the EMFE constraint beyond the limit circle (calculated inside a square surrounding the circle).

The mathematical details of the channel model and the procedures and simulation assumptions are provided in [APV+22-2].

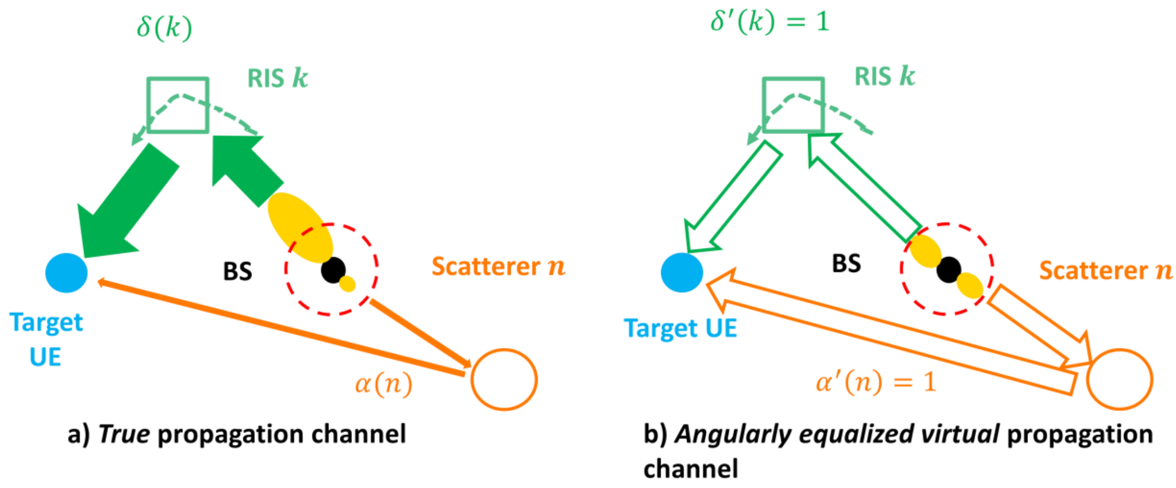

Figure 2-6 Angularly equalized virtual propagation model.

Results

Figure 2-7 illustrates the statistics of the performance metrics introduced in 2.1.3, over random channels. Figure 2-7-a) illustrates the CDF of the percentage of positions exceeding the EMFE constraint (assuming the same UE is targeted for a long period), beyond the limit circle. Figure 2-7-b) illustrates the CDF of the BS transmit power and Figure 2-7-c illustrates the CDF of received power at the target UE. Performance with and without RIS assistance is plotted. MRT BF alone is not deployable. Reduced BF is compliant with the EMFE constrains but provides a low received power at the target UE. The Equalized BF scheme maximizes the received power at the target UE and perfectly matches the constrain.

Detailed results and assumptions are available in [APV+22-2].

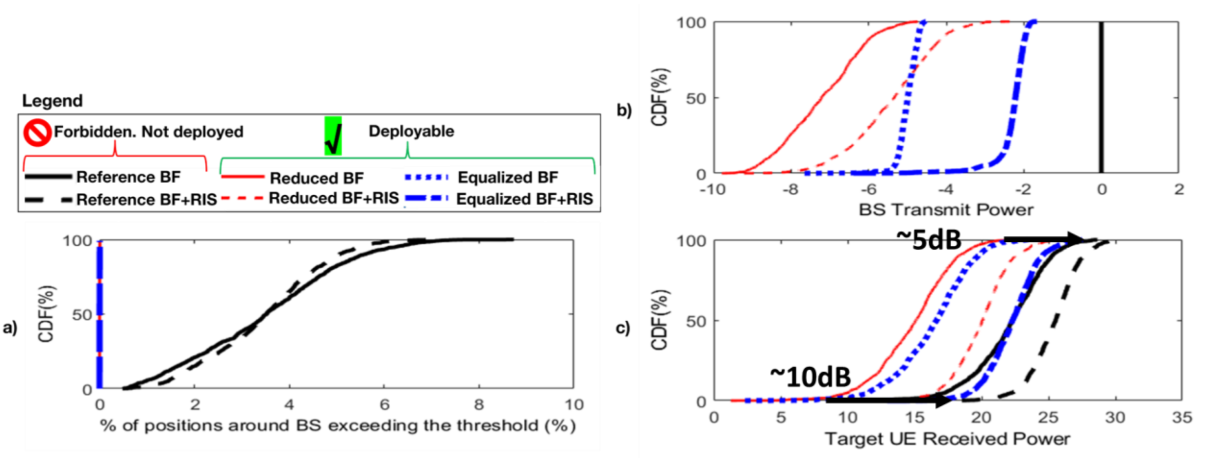

Figure 2-7 Results.

As in Section 2.1.1, compared to the reference Reduced BF scheme, the proposed scheme boosts the received power at the UE by **5 dB** to **10 dB**. As in Section 2.1.1, compared to the reference Reduced BF scheme, the proposed scheme **boosts EMFEU by a factor of x2.05 to 3.45.**

Conclusion

In this study, we propose a novel RIS-aided BF scheme called Equalized BF. It is built based on a virtual angularly equalized propagation channel. Equalized BF scheme provides a better throughput than Reduced BF scheme, and perfectly matches the EMFE constrain. **Therefore, the proposed scheme boosts the I-EMFEU.** Compared to the reference Reduced BF scheme, the proposed scheme **boosts EMFEU by a factor of x2.05 to 3.45. This gain is reported in the summary Table 2-1**.

2.1.3 A3: EMF-Aware MU-MIMO BF in RIS-Aided Cellular Networks

This section summarizes the work detailed in [YIP22-1]. Note that an improved version of this algorithm is also available and detailed in [YP22-2].

Introduction

RISs are one of the key emerging 6G technologies that are expected to improve the link budgets between transmitters and receivers by adding artificial propagation paths. In such re-configured propagation environment, DL MU-MIMO brings capacity improvement to cellular networks. It benefits from the spatial dimension offered by MIMO systems to enable simultaneous transmission of independent data streams to multiple users on the same Radio Resources (RRs) by applying appropriate BF schemes. However, in some cases, serving the same subset of users for a long period of time may cause some undesired regions where the average EMFE exceeds the regulatory limits. To address this challenge, we propose a novel inter-EMF aware MU-MIMO BF scheme that aims to optimize the overall capacity under EMFE constraints in RIS-aided cellular networks.

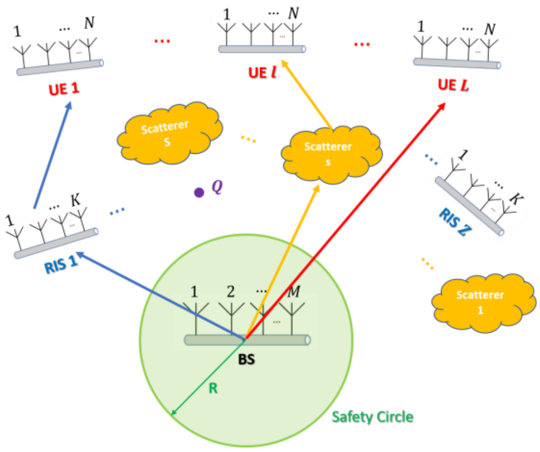

Figure 2-8 A MU-MIMO RIS-aided network model.

System Model

We consider the DL communication of a RIS-aided MU-MIMO network. As depicted in Figure 2-8, there are a BS and L different UEs in the cellular network, they are all equipped with multiple antennas. Assume that the BS has a linear antenna array of M antenna elements and each UE has N antenna elements. Thus, the total number of received antennas is $N_t = LN$. Those antenna elements are spaced by 0.5λ to the adjacent ones either on the BS or a single UE side, where λ indicates the wavelength of the carrier frequency. We assume that the BS must serve the UEs for a long period with the same BF scheme and power allocation, during the entire period. Therefore, the EMFE constrains must also be met instantaneously, to be met in average.

Besides, there are S scatterers and Z RISs randomly located in the given space, respectively. Each RIS has a linear array of K elements with a spacing of 0.5λ. For simplicity, we consider here the far-field calculation method, i.e., both scatterers and RISs are far from the BS and the UEs. In the far-field, the electromagnetic waves propagate at the speed of light and electric and magnetic fields are mutually perpendicular.

Here, we consider an Orthogonal Frequency Division Multiplexing (OFDM) waveform and random Rayleigh fading. With spatial multiplexing, multiple streams are sent from the BS to distinct active UEs simultaneously, which are separated by using precoding schemes. In our case, the Zero-Forcing (ZF) linear precoding scheme adapted to multiple receiving antennas is applied. The network adopts Time Division Duplex (TDD) mode and thus the channel reciprocity is feasible.

First, the BF at the RIS side is selected based on the following procedure: (i) each UE sends some pilots which allow the RIS to estimate the UE-to-RIS channels, (ii) then based on this channel estimation, each RIS computes the BF reflection weight $w^z = \mathbb{C}^{K\times 1}$, reconfigures the weights and freezes. The phase shift weight is multiplied by a reflection amplitude r_{ris}, where $0 \leq r_{ris} \leq 1$ is a constant value depending on the hardware structure of the RIS. Here we set $r_{ris} = 1/K$. $r_{ris} = 1$ means that the RIS is reflecting as much as a natural scatterer. Once the RIS is configured, the UE sends pilots again, the BS can estimate the DL channel considering the RIS configuration and determine the appropriate BS BF to be used for data transmission.

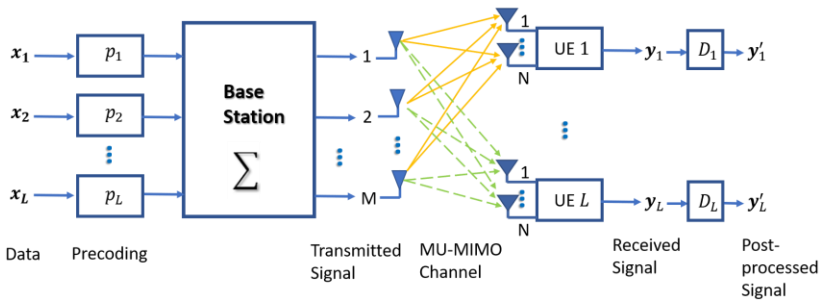

Figure 2-9 DL MU-MIMO Scheme.

Results

In this work, we focus on RIS-aided MU-MIMO scenario and aim to design efficient BF scheme to optimize the DL network capacity while satisfying EMFE constraints. In our scenarios, some RISs are randomly distributed as reflective surfaces to work on transmitting the incident signal to specified UE. First, we examine the “reference” MU-MIMO BF scheme that maximizes the DL capacity with full power transmission and without any EMFE constraint. It corresponds to a ZF precoding with a water-filling power allocation strategy. Then, we propose the “reduced” EMF-aware BF which consists of decreasing the overall transmit power until the EMFE limits are fulfilled. Moreover, we propose a novel “enhanced” EMF-aware BF with a per layer power control mechanism that is designed to meet EMFE constraints and achieve higher capacity performance. Here, we numerically evaluate the performance of the reduced and the enhanced EMF-aware BF schemes.

Name	Symbol	Value
Number of antenna elements at BS	M	64
Number of antennas at each UE	N	4
Number of RISs	Z	3
Number of Scatterers	S	3
Number of antennas at each RIS	K	4
Maximum transmit power	P_{max}	200 Watt
Radius of Safety Circle	R	50 m
EMFE threshold	EMF_{th}	-5 dBm

Table 2-2 Simulation Parameters.

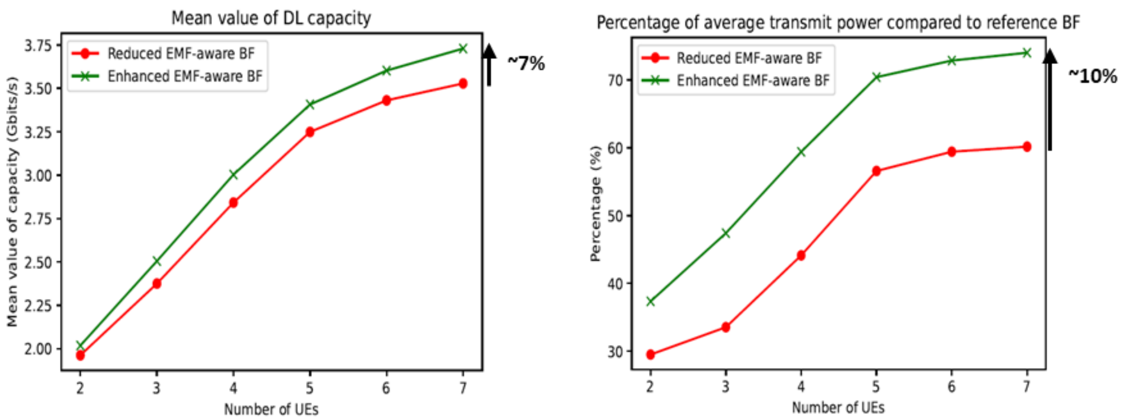

Figure 2-10 Numerical results.

We consider different number of UEs, i.e., from $L = 2$, to 7. There are 1000 samples of channels corresponding to each number L in the simulation. In Figure 2-10, the left figure plots the average DL capacity of the cellular network with respect to different BF schemes. The enhanced EMF-aware BF can maintain more than 70% of the capacity, which **is 7% higher than the reduced BF, with the same EMFE constrain**. The gain in EMFEU of the proposed scheme wrt to the reduced scheme, is therefore of **x1.07.**

The right figure presents the percentage of average transmit power at the BS for the two proposed BF schemes compared to the reference BF. The enhanced EMF-aware BF can still guarantee the EMFE limits with about 10% higher transmit power than the reduced one.

Conclusion

In this work, we modelled the DL communication in a RIS-aided MU-MIMO systems. Two BF schemes are proposed to address EMFE regulation: (i) reduced and (ii) enhanced EMF-aware MU-MIMO BF. We compare the simulation performance of these two schemes. The enhanced EMF-aware scheme achieves a higher system capacity compared to the reduced one which has a lower average transmit power. In the near future, we will jointly optimize the transmit precoding weight and the power allocation scheme in order to achieve higher capacity performance while satisfying EMFE regulation. **Therefore, the proposed scheme boosts the I-EMFEU.** Compared to the reference Reduced BF scheme, **the proposed scheme boosts the EMFEU by a gain factor of x1.07. This gain is reported in the summary Table 2-1**.

2.1.4 A4: EMFE Avoidance thanks to Non-Intended User Equipment and RIS

This section summarizes a study that will be detailed in the paper under preparation [GPHS22].

Introduction

5G and beyond systems call for improved service qualities in terms of, e.g., data rate, EE, and latency. With more radio resources at millimeter wave (mmWave) or even THz frequencies, more opportunities have been revealed to improve the end-to-end throughput and at the same time, reach good trade-off with EE. However, signals at high frequencies can be significantly affected by the penetration loss, together with severe path loss and BF mismatch. State-of-the-art research studies on, e.g., advanced MMIMO BF, deploying small cells, and various spatial and temporal resource allocation methods, could reach different performance-complexity trade-offs. From another perspective, these advanced wireless communication schemes trigger renewed attention to EMFE from both regulation authorities and populations. Although currently there is no scientific evidence that EMFE could have adverse effects on the environment and the population health at levels below what is already regulated, it is becoming more and more important to design sustainable and health-guaranteed wireless systems to satisfy both current and potential strict regulations due to increasing public acceptance requirements.

RIS has emerged as a promising future technical candidate thanks to its capabilities to program the radio environment and utilizing the desired propagation paths. It is extremely helpful when the direct link from the access point (AP) to a user faces deep fading and/or blockage. Moreover, with a proper deployment, RIS can cover different areas with different service requirements, which makes it possible to bypass certain blockage/users with no need for handover, backhauling, and wired energy supply. Inspired by these features, with the EMF aspect being considered, one can use RIS to create additional paths to avoid exceeding EMF powers in certain area or directions.

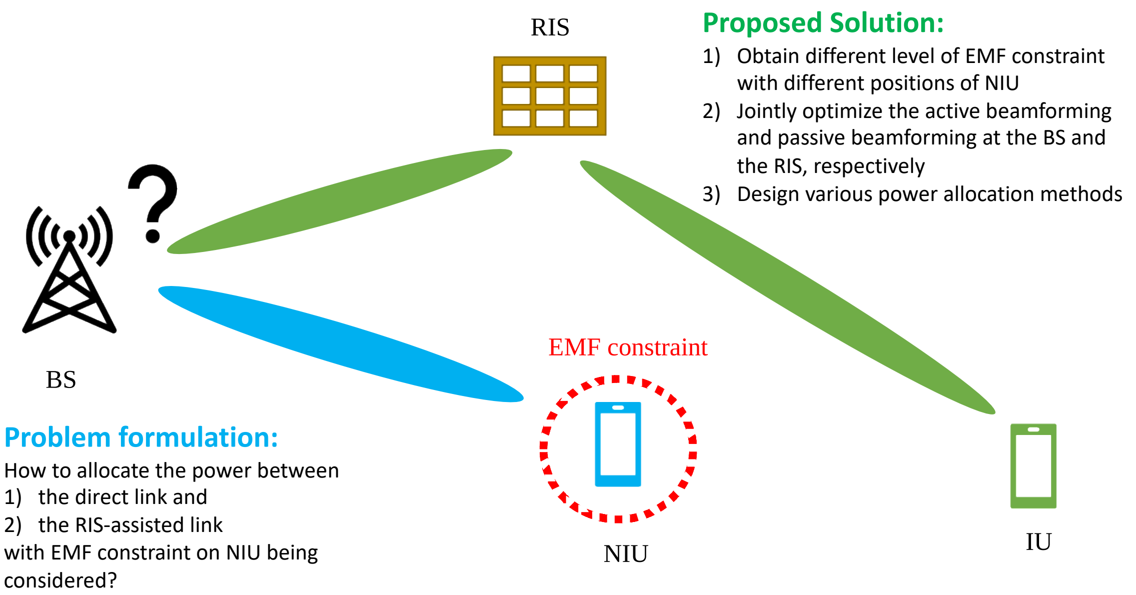

Figure 2-11 Problem and proposed solution.

Recent research studies have addressed the BF design at both the BS and the RIS with limited beam power requirements as EMF constraints. In this work, we consider various cases, where the relative positions of the non-intended user (noted NIU in this current sub-section) with respect to the intended user (noted IU in this current sub-section) are different. Specifically, we investigate the potential of EMF-constrained RIS-assisted networks with proper power allocation between the direct BS-IU and the in-direct BS-RIS-IU paths. The problem formulation and the contributions can be seen in Figure 2-11.

System Model

We consider a small cell outdoor BS/AP operating with mmWave carrier frequencies. As illustrated in Figure 2-12, we consider an RIS-assisted DL MIMO network with one BS (N_T antennas), one RIS (N elements) and a pair of single-antenna IU and NIU. Here, IU is the user who wants to receive service from the BS while the NIU has no need to connect to the BS. More importantly, NIU prefers to have limited EMFE given that it has no communication service. The NIU moves between the BS and the IU. Depending on the location of the NIU and the beam width from the BS, at some points/areas the NIU and IU receive the same transmission from the BS. We assume that the NIU does not decode the message or absorb the energy from the BS. RIS is assumed to be in the far field of target UEs and the BS. TDD mode is assumed, where perfect CSI could be obtained from channel reciprocity.

As illustrated in Figure 2-12, we jointly optimize the RIS and the BS BF for the intended user, given that a non-intended user moves between the BS to the intended user along the x-axis, with some EMF constraints. Targeting on maximizing the data rate at the IU with limited power budget, we propose a closed-loop scheme based on the feedback from NIU with the direct link being considered, in order to fully explore the potential of RIS-assisted systems with EMF constraints. Hence, this scheme aims at improving the EMFEU metric.

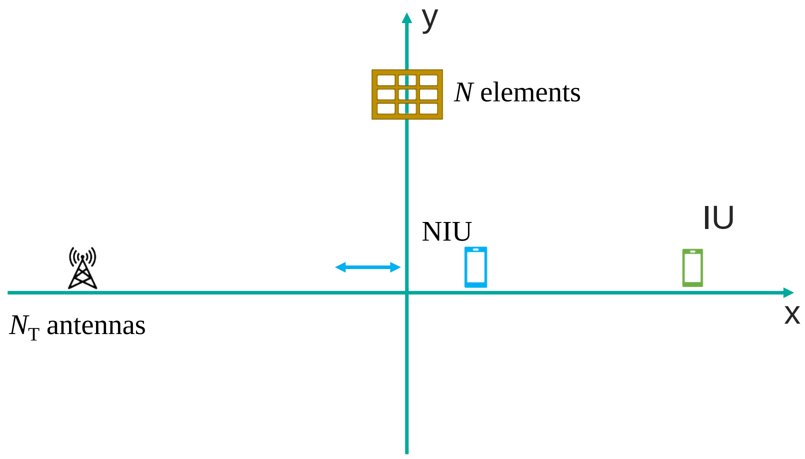

Figure 2-12 System Model.

In some scenarios, especially with large number of elements in RISs, computing the phase coefficients at the RIS and precoder at the BS with explicit CSI may not be practical. Inspired by the precoding scheme with predefined codebooks, we propose to use a DFT codebook-based beam optimization where the RIS beam is selected from the pre-defined beam patterns while only the BS-RIS-IU concatenated channel is required to obtain the optimal beam. We compare the proposed DFT-based beam optimization with the state-of-the-art AO scheme where the full knowledge of CSI is required.

Results

Here, we present the numerical results of considered power allocation schemes:

- Method 1: Allocate all power to the BS-RIS-IU link (DFT optimization);
- Method 2: Allocate all power to the direct link, with respect to the EMF constraint;
- Method 3: First fill the direct link with the maximum possible power with respect to the EMF constraint, then transmit the remaining power to the BS-RIS-IU;
- Method 4: Exhaustively find the best power allocation considering the EMF constraint;
- Upper bound: No EMF constraint and transmit with the direct link.

Name	Symbol	Value
Transmit antenna at BS	N_T	32
RIS elements	N	100
Carrier frequency	f_c	28 GHz
Bandwidth	B	100 MHz
Noise power	N_0	-174 dBm/Hz with 10 dB noise figure
EMF constraint	$\bar{P}$	0.1 mW
Total power	P	43 dBm
BS position	-	[-80m, 0]
RIS position	-	[0, 50m]
IU position	-	[80m, 0]

Table 2-3 Simulation Parameters.

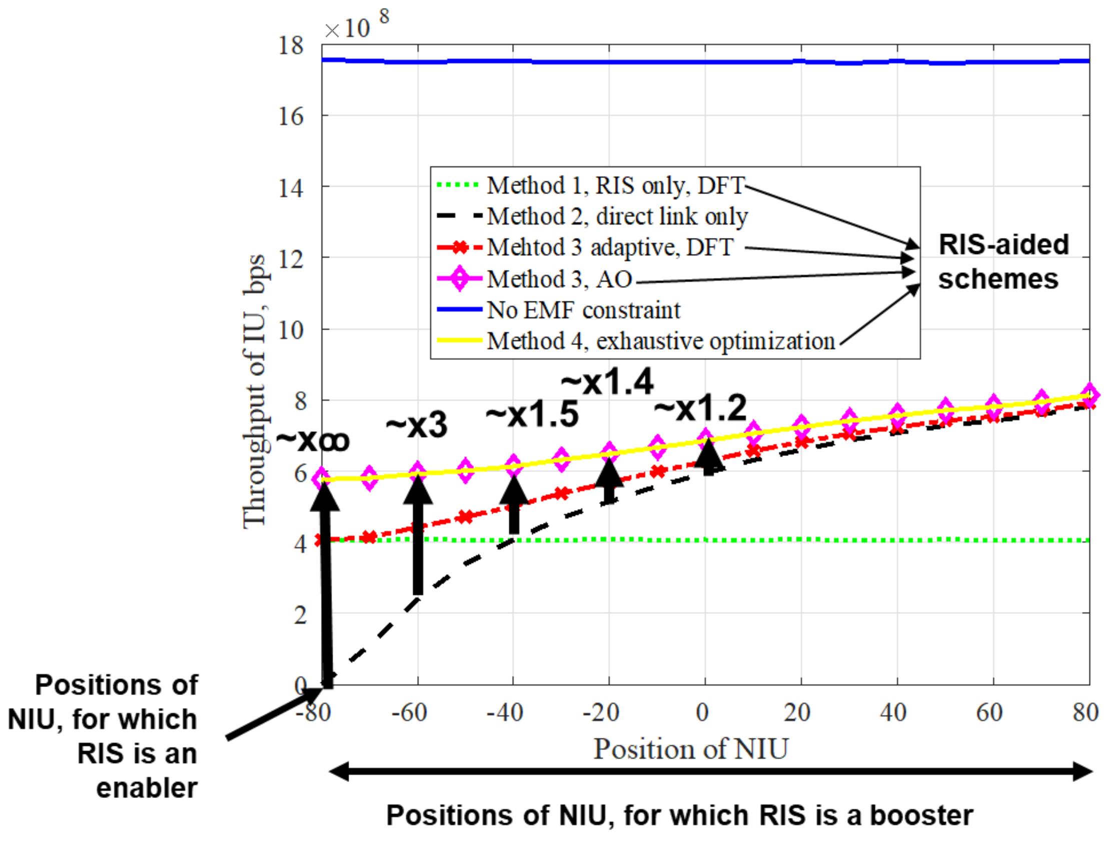

Figure 2-13 Results.

Our results indicate that, although the EMF constraint would strongly benefit from an additional RIS link to meet the performance requirements of the IU, depending on the position of the NIU, the direct link is still useful to further improve the performance.

In the particular case where the NIU is at position -80, the reference scheme (without RIS) is forbidden to transmit to meet the EMFE, and the attained throughput is zero bps. The gain in EMFEU of RIS-aided schemes over the reference scheme without RIS is therefore **infinite**. In this case, the RIS-aided schemes are “**enablers**”, that is, they make the service feasible under EMFE constrains.

For other locations of the NIU proposed RIS-aided scheme boost the SE wrt to the scheme without RIS, under the same EMFE. They provide finite gains.

Therefore, the proposed schemes boost the I-EMFEU. The proposed schemes even enable the service in some scenarios, compared to the case with no RIS.

Conclusion

We designed an RIS-assisted EMF-constrained system with the same beam for both IU and NIU, and we designed different power allocation methods for the direct and RIS-assisted links. To optimize the RIS, we designed both AO- and DFT-based methods that can reach similar performance with full/limited CSI. **Therefore, the proposed schemes boost the I-EMFEU**. The proposed schemes even enable the service in some scenarios, compared to the case with no RIS. **These advantages are reported in the summary Table 2-1**.

2.1.5 A5: EMFE Avoidance thanks to Non-collaborative Non-Intended User Equipment and RIS

This section summarizes a study that will be detailed in the paper under preparation [GPHS23].

Introduction

In our previous work [GPHS22] (presented in Sub-Section 2.1.4), we consider various cases, where the relative positions of the non-intended user (noted NIU in this current sub-section) with respect to the intended user (noted IU in this current sub-section) are different. Specifically, we investigate the potential of EMF-constrained RIS-assisted networks with proper power allocation between the direct BS-IU and the in-direct BS-RIS-IU paths, under the assumption that NIU is fully cooperative, i.e., the location and EMF level of NIU is fully aware by the BS. In this study, we consider non-collaborative NIU with unknown location/channel and EMF level, and design an integrated sensing and communication (ISAC) system to detect NIU and communicate with IU.

System Model

We consider a small cell outdoor BS/AP operating with mmWave carrier frequencies. As illustrated in Figure 2-14, we consider an RIS-assisted DL MIMO network with one BS (M antennas), one RIS (N elements) and a pair of single-antenna IU and non-collaborative NIU. Here, IU is the user who wants to receive service from the BS while the NIU has no need to connect to the BS. More importantly, NIU prefers to have limited EMFE given that it has no communication service. The NIU moves between the BS and the IU. Depending on the location of the NIU and the beam width from the BS, at some points/areas the NIU and IU receive the same transmission from the BS. We assume that the NIU does not decode the message or absorb the energy from the BS. RIS is assumed to be in the far field of target UEs and the BS. TDD mode is assumed, where perfect CSI could be obtained from channel reciprocity. With non-collaborative NIU, since the reflected power of radar and communication systems have similar components, i.e., channel and BF vector with path loss being dominant, the reflected power of NIU sensing can be a reference for the transmit power limitation at the BS. Note that we assume sensing and communication do not interfere with each other by, e.g., allocating different time slots, which is a fair assumption given the collaborative NIU would also need overhead to report essential information. Also, due to the nature of the considered problem setup, the BS has to acquire information first before deciding the power level.

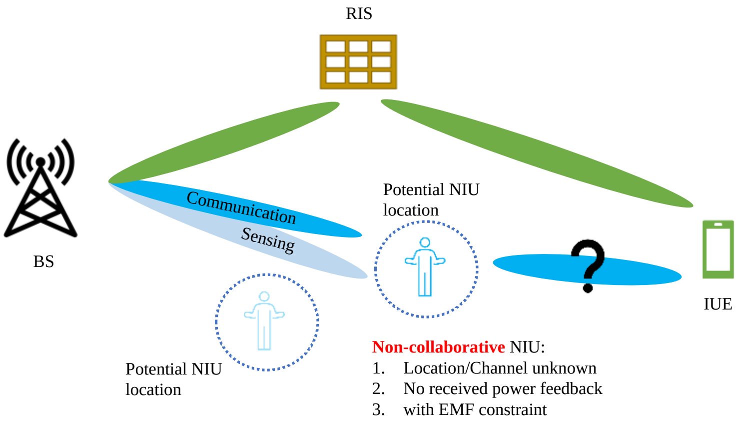

Figure 2-14 Problem and proposed solution.

As illustrated in Figure 2-14, we jointly optimize the RIS and the BS BF for the intended user, given that a non-intended user moves between the BS to the intended user along the x-axis, with some EMF constraints. Here, the BS BF needs to consider three aspects: direct link sensing beam (to NIU), direct link communication beam (to IU, but affect NIU), and indirect communication beam (to IU through RIS). Targeting on maximizing the data rate at the IU with limited power budget, we propose a closed-loop scheme based on the feedback from NIU with the direct link being considered, in order to fully explore the potential of RIS-assisted systems with EMF constraints. Hence, this scheme aims at improving the EMFEU metric. To optimize the sensing beam without any channel information, we propose a genetic algorithm (GA)-based method to achieve the proper solution.

Expected Results

Here, we present the numerical results of the considered power allocation schemes. Alternating Optimization (AO) is used for all RIS optimization as presented in [GPHS22]:

- All RIS: With collaborative NIU, allocate all power to the BS-RIS-IU link
- All direct: With collaborative NIU, allocate all power to the direct link, with respect to the EMF constraint
- Hybrid: With collaborative NIU, first fill the direct link with the maximum possible power with respect to the EMF constraint, then transmit the remaining power to the BS-RIS-IU
- ISAC-GA: With non-collaborative NIU, using GA to optimize the sensing beam
- ISAC, random beam: With non-collaborative NIU, using random the sensing beam
- Upper bound: No EMF constraint and transmission with the direct link

Name	Symbol	Value
Transmit antenna at BS	M	32
RIS elements	N	100
Carrier frequency	f_c	28 GHz
Bandwidth	B	100 MHz
Noise power	N_0	-174 dBm/Hz with 10 dB noise figure
EMF constraint	$\bar{P}$	0.1 mW
Total power	P	43 dBm
BS position	-	[-80m, 0]

RIS position	-	[0, 50m]
IU position	-	[80m, 0]

Table 2-4 Simulation Parameters.

Figure 2-15 Simulation results for different considered schemes.

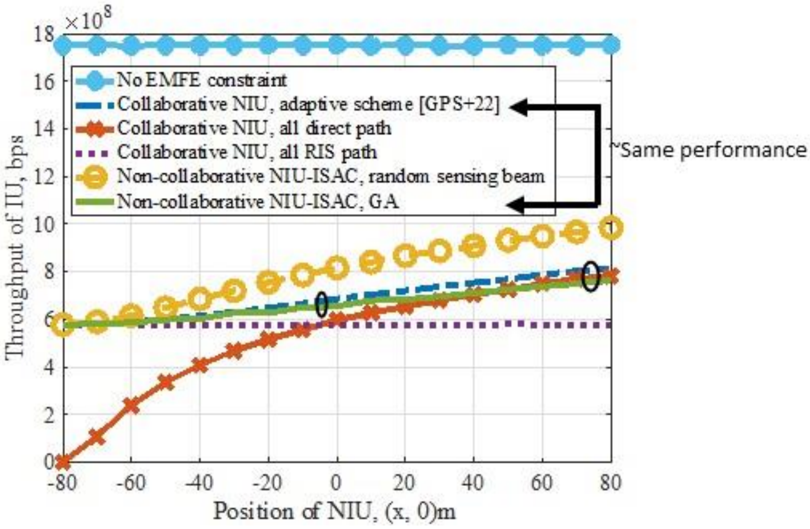

Figure 2-16 Simulation results on the received power of NIU.

Discussion and Conclusion

We designed an RIS-assisted EMF-constrained system with the same beam for both IU and NIU, and we designed different power allocation methods for the direct and RIS-assisted links. To tackle non-collaborative NIU, we designed an ISAC system and propose a GA-based scheme to jointly optimize BS beams with various constraints. Our results indicate that, the proposed method can reach the same performance compared with collaborative NIU. **Therefore, compared to a scheme without RIS, the proposed scheme has the same advantages (regarding EMFEU) than the scheme presented in 2.1.5. This is reported in the summary Table 2-1.**

2.1.6 A6: EMFE Mitigation in RIS-Assisted Multi-Beam Communications

This section summarizes a study that detailed in the paper [SVK+23] designed for I-EMFEU improvement, at mmWaves.

Introduction

Exposure to EMF recently became a field of interest in many applications due to the expected exponential increase in the number of devices. Providing sustainable communications is an objective as the 6G moves forward. Technologies like RIS and mmWave are key enablers of 6G and become useful for EMFE-aware applications. We exploit the multiple propagation paths provided by the RIS along with mmWave high directivity to avoid excessive exposure to non-intended users (NUEs). However, when NUEs block the communication path in both direct and reflected paths, the BS may not be able effectively communicate with UEs without a sophisticated strategy for BF. Figure 2-17 exemplifies the study case.

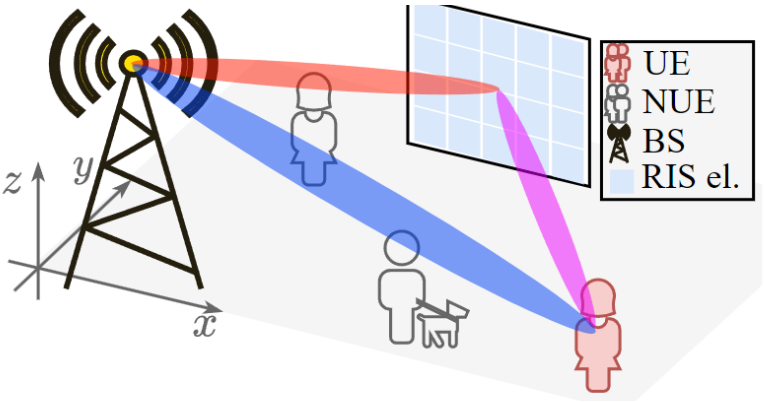

Figure 2-17 Considered deployment scenario.

System Model

We consider a mmWave TDD MIMO system where a BS equipped with M antennas communicates in DL with a single-antenna UE aided by an RIS composed of N reflective elements. Along with the active UE, there is a set of NUEs that are not communicating with the BS and should not be exposed to excessive EMF. We consider the Rayleigh channel model with the channel coefficients described as a factor of the path-loss (PL), specifically mmMAGIC urban line-of-sight (LOS) model, and small-scale fading accounting for multi-path propagation. The PL is dependent on the three-dimension (3D) Euclidean distance, the carrier frequency, and stochastic shadow fading.

We aim to develop a downlink communication method to minimize the EMFE at NUEs constrained to a minimum spectral efficiency (SE). The BF and reflection coefficient calculations for both BS and RIS are constrained to a predefined DFT-based orthogonal words codebook and we apply a Multi-Beam Power Equalization through genetic algorithm (MB-GA) to calculate the power of each codeword at the BS, subject to a restricted power pool, and select the codeword at the RIS, assessing the quality of the communication channel at the UE and minimizing the EMFE at the NUEs. The method is evaluated in 2-D (RIS-BS-NUE-UE has the same height) and 3-D (heights: BS > RIS > NUE = UE) scenarios with either CSI knowledge or in a localization-based framework. The results are compared with a power-constrained MRT precoder.

The interested reader can refer to [SVK+23] for all the details on the system model, problem formulation, and algorithmic solutions.

Results

We evaluate our contributions using ten thousand Monte Carlo simulations with random realizations of channel coefficients and different NUE-BS distances. Figure 2-18 presents the obtained SE and EMFE for 2-D and 3-D scenarios, under perfect CSI. By exploiting the multiple propagation paths in various codewords, our method is able to surpass the MRT in both SE and EMFE using 0.79% of the power used by the MRT. Next, assuming only the localization knowledge of both UE and NUE, Figure 2-19 presents the obtained SE and EMFE. Although the SEs are slightly lower for the proposed method, the EMFE is considerably lower, leading to a higher Rate/Exposure ratio.

Name	Symbol	Value
Transmit antenna at BS	N_T	36

RIS elements	N	100
Carrier frequency	f_c	28 GHz
Bandwidth	B	100 MHz
Noise power	N_0	-174 dBm/Hz with 10 dB noise figure
Available power	P	43 dBm
BS position	-	I. [-80, 0, 1.5] II. [-80, 0, 10]
RIS position	-	I. [0, 50, 1.5], II. [0, 50, 5]
IU position	-	[80, 0, 1.5]
Shadow fading	σ_{SF}	2 dB

Table 2-5 Simulation Parameters.

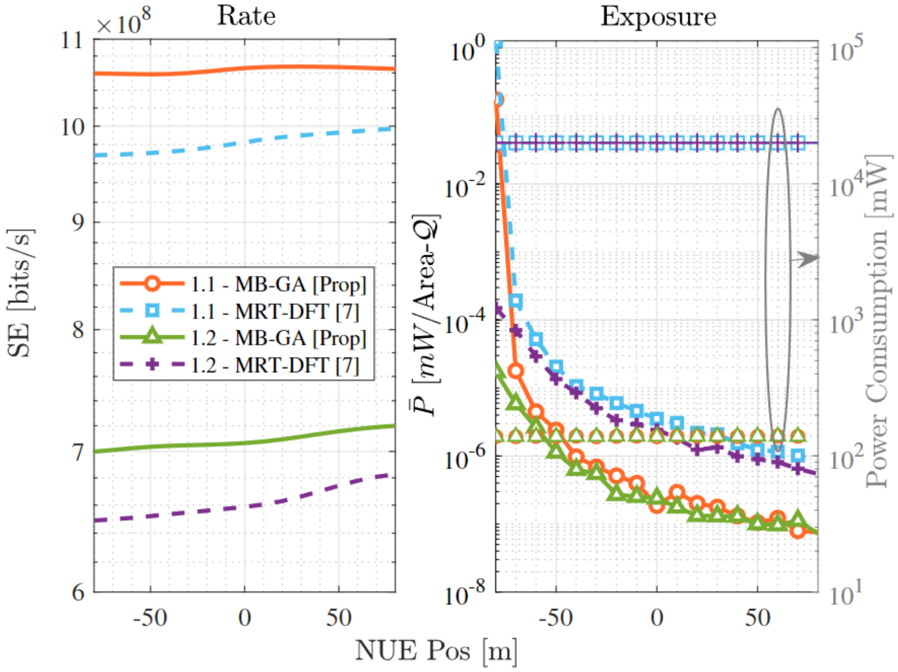

Figure 2-18 Achieved rate (left) and exposure (right) performance under perfect CSI for Scenario 1.1 with two-dimension (2D) and 1.2 with 3D. The NUE is positioned at the origin of the y-axis and moves from −80 meters (BS position) to 80 meters (UE position).

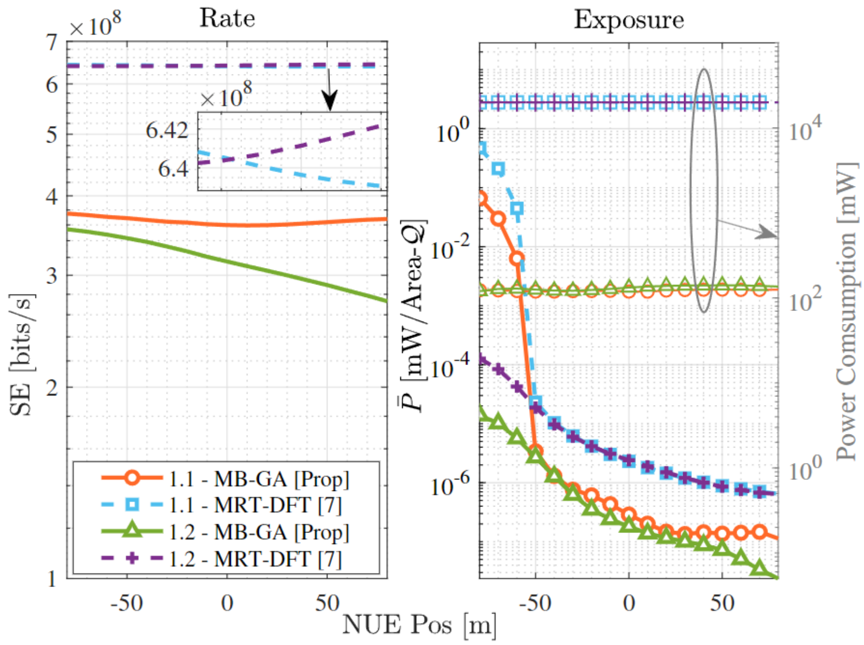

Figure 2-19 Achieved rate (left) and exposure (right) performance under localization for 1.1 (2D) and 1.2 (3D). The NUE is positioned at the origin of the y-axis and moves from −80 meters (BS position) to 80 meters (UE position).

Conclusion

This work assessed the potential of multi-beam transmission with mmWave directivity and RIS multi-path enhancement. Our results reveal that, thanks to the physical characteristics of next-generation technologies, it is possible to exploit multiple propagation paths to improve the QoS and reduce EMFE. Specifically, assuming perfect CSI, the MB-GA method overcomes MRT-based solution in every metric at a complexity cost, while assuming localization it has degraded SE performance but with lesser exposure. **In particular, the main metric of interest, i.e. I-EMFEU, can be decreased by around one order of magnitude. This gain is reported in the summary Table 2-1.**

2.2 Category B: I-EMFEU Boosting in Uplink

2.2.1 B1: Blue Communications for Edge Computing: the RISs Opportunity

This section summarizes the work detailed in the submitted paper [AMC+22].

Introduction

In this study, we investigate the synergy between RISs and multi-access edge computing (MEC)-aided wireless networks for enabling computation offloading tasks via low EMF communications.

We consider for this purpose an RIS-assisted scenario of MIMO system aware BF. We focus on the typical case of computation offloading, i.e., the UL traffic, which generally pertains to the continuous transfer of capillary data from extreme edge devices such as sensors and cars, to enable computational demanding services in real-time, at the edge of wireless communication networks. This drastic growth calls indeed, for new optimization metrics that include energy, service delay, and EMFE.

In line with this, we deal in this analysis with the EMFE under end-to-end delay constraints of a computation offloading service. We formulate thus, the blue (i.e. low EMFE) communications edge computing problem as a long-term optimization aiming to minimize the average EMFE, as per ICNIRP recommendations, under MEC service delay constraints. We design an online algorithm able to dynamically configure RIS parameters, transmitter precoding, receiver combiner, and transmit power, with theoretical guarantees on system stability and asymptotic EMFE optimality. Note that, precoding, combining, and RIS parameters are selected from generic codebooks.

Description and objective

System Model

We consider a MIMO system where a single user aims to offload his computation tasks to a mobile edge host (MEH) collocated at his serving AP, through an RIS-aided wireless link. We consider time as organized in slots 1, 2, . . . of equal duration τ. At the beginning of each slot, new offloading data are generated, new radio channels are observed and, based on these and other observations, a new resource allocation decision is taken. Accordingly, while instantaneous instances of the EMFE may reach high values, the long-term average is finally minimized to achieve low exposure, under service delay guarantees.

General optimization problem

As illustrated in Figure 2-20, for EMFE evaluation, space is considered as divided in pixels of equal size. Then, assuming that humans possibly exist in one or more of these pixels, our objective is to minimize a weighted sum of the EMFE in each pixel. In this way, if humans are not generally present in one pixel, the EMFE problem can be neglected in that particular location in space, assigning weight 0. This way, it is possible to customize on a case-by-case need.

- **The p-th pixel EMFE:**

In this case, we deal with the scenario of one human placed in pixel p, then, the objective becomes the p-th pixel EMFE, to achieve a blue communication area. Note that, this is the example represented in the numerical results. Otherwise, the overall method is more general and applies to multiple humans sojourning in multiple pixels. To cope with ICNIRP recommendations [ICN20], we consider the incident power density, as a metric for EMFE evaluation. Then, taking into account, the impact of both the direct and the reflected paths, we represent the overall instantaneous power density as

$$P_{d,p}(t) = \frac{4\pi}{\lambda^2} P_{tx}(t) \left| h_p(t) w_u(t) \right|^2$$

Where $h_p(t) = h_{d,p}(t) + h_{r,p}(t)\Theta(t)H_{u,r}(t)$ is representing the overall channel between the user and pixel p, comprising both the direct channel vector between the UE and pixel p and the channel vector between the RIS and pixel p. w_u is the user precoding vector and P_{tx} is the user transmit power at time t. As already mentioned, the goal of this investigation is to minimize the long-term average EMFE in selected areas across space under service delay constraints, by dynamically and adaptively controlling the user precoding vector, the transmit power, the RIS reflectivity parameters, and the combining vector.

Then, thanks to the theoretical foundations of Lyapunov stochastic optimization, we decompose a long-term complex optimization problem and solve it in a per-slot basis, thus performing an exhaustive search over the codebooks (designed for the precoder, the combiner, and the RIS parameters), with corresponding closed form solutions for the transmit power. This is possible thanks to the definition of a suitable function (an instantaneous objective that weights service queue states and EMFE) to be minimized in each time slot, based only on instantaneous observations. This guarantees the queue stability constraints (communication and computation buffers), while asymptotically approaching the global optimal solution through one tuning parameter that trades off average EMFE optimality and service delay.

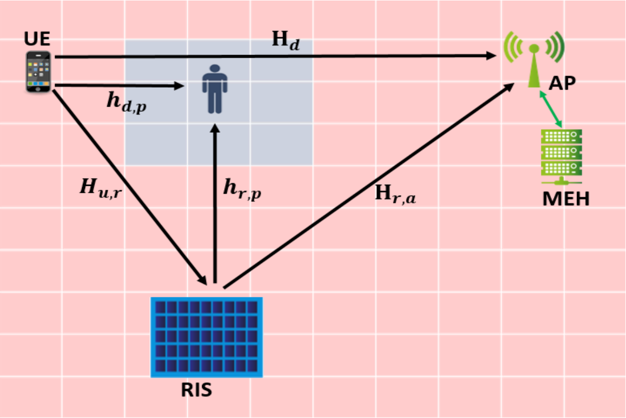

Figure 2-20 System Model.

Results

The antenna patterns used to build w_u, w_a, and T (respectively, the precoder, the combiner, and the RIS codebooks), are taken from [RH10], with each element modelled as in [CLS+12]. A range of -60° to 60°, with a step of 10° is considered for the UE and the AP, while a range of -30° to 30° with a step of 5° is considered for the RIS, with 0° the direction perpendicular to the array. At the MEC side, we assume the MEH to be able to accommodate all requests on average, however with an instantaneous random f(t) (the amount of resources in central processing unit (CPU) cycles/s) uniformly distributed. In particular, denoting by (x, y, z) the 3D coordinates of an element, we model the scenario deployment depicted in Figure 2-20 using the following positions: the AP at (50,50,1), the UE at (0,50,1), the RIS at (4,48,1), and the person at (1,50,1).

Name	Symbol	Value
Bandwidth	B	800 MHz
Carrier frequency	f	28 Ghz
Noise power spectral density	N0	-174 dBm/Hz
Slot duration	τ	10 ms
Arrival rate	$A_k(t)/s$	10 Gbps
The user maximum transmit power	P_{tx}^{max}	100 mw
Transmit and receive antennas	N_u and N_a	8
RIS elements	M	20

Table 2-6 Simulation Parameters.

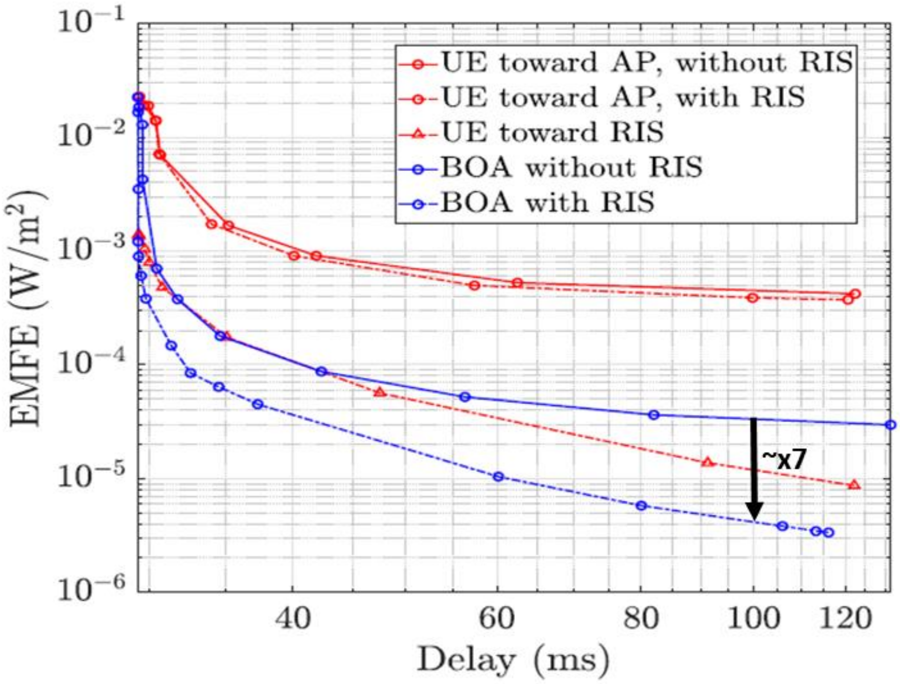

Figure 2-21 Results.

Numerical results show the effectiveness of our method and the benefits of the RIS in enabling blue communications for computation offloading services, due to which the UL direction of communication will be exploding in future 6G systems.

For instance, as one of obtained results, Figure 2-21, shows the trade-off between the EMFE and the average end-to-end (E2E) delay. For this simulation, we consider four different benchmark comparisons: i) the no RIS case, with the UE always transmitting towards the AP, and with transmit power optimized; ii) the RIS-aided case, with the UE always transmitting towards the AP, and with transmit power optimized; iii) the RIS-aided case, with the UE always transmitting towards the RIS, and with transmit power optimized; iv) the case without the RIS, but applying our optimization method. Finally, we term our full optimization algorithm as BOA (blue optimization algorithm). Results show how the use of the RIS offers the opportunity to reduce the level of EMFE for a given service delay, also in the case the UE always transmits towards the RIS. However, this gain is considerably enhanced when BOA is applied, due to the increased degrees of freedom introduced by the adaptive selection of precoding, combining, and RIS parameters. In the considered scenario, our proposed solution with RIS achieves around x7 of EMF reduction with respect to the best benchmark scheme without RIS, for a fixed E2E delay of 100 ms. Hence, the EMFEU gain due to the introduction of RIS is x7.

Conclusion

We proposed an online method able to adaptively and jointly optimize precoding, combining, RIS parameters, and transmit power in a RIS-aided MEC offloading scenario. As objective, we considered the average EMFE in selected areas within the service coverage, with constraints on the E2E service delay. We reduced a long-term problem to a per slot optimization, which allowed us to solve it through a low complexity procedure involving an exhaustive search over low cardinality sets, coupled with a closed form solution for the transmit power.

Therefore, the proposed scheme boosts the I-EMFEU. In the considered scenario, our proposed solution with RIS achieves around x7 EMF reduction with respect to the best benchmark scheme without RIS, for a fixed E2E delay of 100 ms. Hence, the EMFEU gain due to the introduction of RIS is around x7. **This gain is reported in the summary Table 2-1**.

2.2.2 B2: Achievable offloading rate in RIS-assisted MEC scenarios with power and EMF exposure constraints

Introduction

MEC comes with several facets and challenges into future mobile networks. First, MEC networks will bond communication and computing into a unique system that will benefit from a joint optimization of wireless and computing resources, including scheduling, transmit power, bandwidth, and, ultimately, RIS configuration whenever available in the network. Second, edge computing will increase the wireless UL traffic, since the enabled services generally require a continuous exchange of capillary data from end devices to edge cloud servers. The effects of UL traffic increase have been already mentioned in Sub-Section 2.2.1, and they involve, among the others, the need for a control of EMF exposure, both for meeting more or less strict recommendations and for, e.g., enhanced secrecy. We indeed claim that RISs can be beneficial in creating boosted areas (in terms of, e.g., energy-efficiency, secrecy, EMF exposure, etc.), also for edge computing services. In Sub-Section 2.2.1, with technical details in [AMC+22], we proposed an optimization problem that involves the end device wireless transmit power, the precoding, decoding, and RIS reconfiguration. The problem was cast in a stochastic environment in which radio channels and data arrivals vary over time, so that a dynamic reconfiguration of these parameters is required to adapt the network to such changes. The goal was to minimize the EMF exposure in certain zones in space, under E2E delay constraints of the edge computing service. In this section, we propose a dual problem, in which the data offloading rate is maximized under received power constraints in a selected zone in space, in particular where a non-intended user is located. Differently from [AMC+22] and Sub-Section 2.2.1, , and building on the results proposed in [MBC22] and [Hexa-X-D7.2], [Hexa-X-D7.3], we consider both radio and compute resource allocation (including energy consumption, EMF exposure, and offloading rate), investigating a typical question that arise in such connect-compute context: *where is the bottleneck of the service? Is it the compute resource availability (given predefined energy constraints), or the EMF exposure across space and time?*

Description and objective

System Model

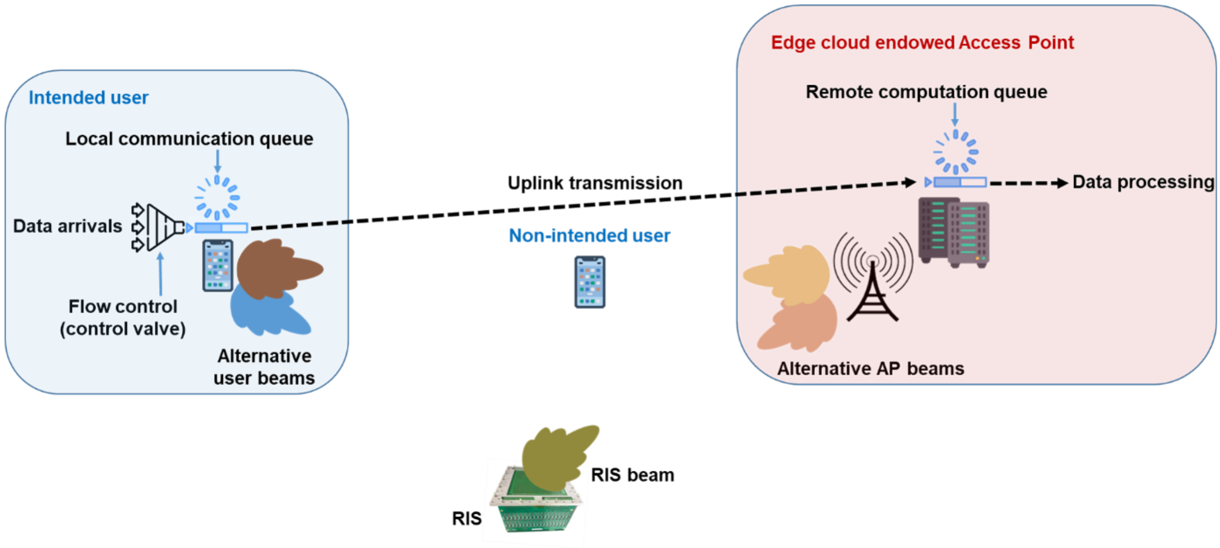

Figure 2-22 Scenario under investigation.

As in Sub-Section 2.2.1, we consider a MIMO system, in which a single user aims to offload its computation tasks to an edge cloud server, collocated at its serving AP, possibly through an RIS-aided wireless link. The system is very similar to [AMC+22], with one (intended) user offloading computations to the edge server, and a non-intended user [GPHS22], whose measurements can be exploited to keep the received power lower than a threshold in a specific location in space, i.e., its position. To do so, the user can choose to transmit either directly towards the AP, or to transmit towards the RIS, with the latter properly reconfigured to reflect the signal towards the AP. Additionally, the user can dynamically select its transmit power. We employ the queueing model used in [MBC22] with a fictitious control valve that can be used by the user to dynamically control data arrivals. In particular, based on buffer states, the user can decide to proactively drop data arrivals to avoid queue congestion, i.e., infinite service delay. The role of this fictitious control valve is to limit arrivals to keep the overall offloading system stable. Once data are transmitted, they are buffered before computation. The computing frequency is also dynamically selected by the edge cloud server to balance buffer stability and dynamic computing power consumption. The overall chain is depicted in Figure 2-22, and the steps can be summarized as follows:

1. The user generates (or collects) data (see *data arrivals* in Figure 2-22);
2. The user decides whether to store or discard these data, based on the current local queue state, and based on network conditions and constraints violation status (see *control valve* in Figure 2-22);
3. The user transmits data that were previously buffered (see *UL transmission* in Figure 2-22);
4. Data are buffered at the edge cloud server before computation (see *computation queue* in Figure 2-22);
5. Data are processed (see *data processing* in Figure 2-22).

Steps 1-5 are repeated for the whole duration of the service. For this investigation, it is assumes that the service lasts an infinite time, i.e. we deal with long-term statistics and performance.

General optimization problem

The general questions we aim to answer are: *i) what is the arrival delivery ratio that can be sustained by the connect-compute network, based on power and EMF exposure constraints? ii) Is the presence of the RIS beneficial in such context (and under which conditions)?*

To answer the above questions, we can formulate a general long-term problem, whose goal is to maximize the data arrivals accepted into the communication queue (thus, the arrival delivery ratio) under *i)* (communication and computation) queue stability, *ii)* average received power at the non-intended user location below a threshold, and *iii)* average power consumption of the edge cloud server. For the UL data rate, we consider the Shannon capacity as in [AMC+22]. For the received power at the AP and non-intended user, we consider the overall RIS-aided channel, with direct and reflected path, with the latter affected by the RIS reconfiguration [AMC+22]. Differently from [AMC+22], we consider the non-isotropic antenna element response. in the channel model. Finally, the dynamic power consumption of the edge cloud server is modelled through the typical cubic law, with respect to the CPU cycle frequency [MBC22].

The control variables that we aim to optimize in a per-slot fashion are *i)* the accepted data arrivals, constrained between 0 and the actual arrivals at time t; *ii)* the user precoding, AP combining, and RIS phase reconfiguration vectors, all selected from a predefined codebook as in [AMC+22]; *iii)* the user transmit power, constrained between 0 and a maximum value $P_{\max}$; *iv)* the CPU clock frequency of the edge server, constrained between 0 and a maximum value $f_{\max}$. As in [AMC+22], our method is based on stochastic optimization, and it requires to solve a sequence of deterministic problems, based on the observation of channel realizations, data arrivals, and properly defined state variables that track the behaviour of the system in terms of (long-term) constraint violations.

Results

As in [AMC+22], the antenna patterns used to build precoding, combining and RIS configuration vectors are taken from [RH10], with each element modelled as in [CDS12]. We consider planar arrays at all network nodes (user, AP, RIS). The user is equipped with a 4×4 array, the AP with a 10×10 array, and the RIS is a 20×20 array. Denoting by (x, y, z) the 3D coordinates of a generic network node, we model the scenario deployment depicted in Figure 2-22 using the following positions: the AP at (20,10,1), the UE at (0,10,1), the RIS at (10,0,1), and the non-intended user at (10,10,1). Other simulation parameters are reported in Table 2-7.

Name	Symbol	Value
Bandwidth	B	1 GHz
Carrier frequency	f	28 GHz
Path loss exponent	α	3
Additional blockage on direct link	β	30 dB
Rice factor	K	13 dB
Noise power spectral density	N_0	-174 dBm/Hz
Slot duration	τ	10 ms
Maximum arrival rate	$A_{\max}$	500 Mbps
User maximum transmit power	P_{tx}^{max}	100 mw
Number of CPU cycles per offloaded bit	J	100
Maximum edge server CPU frequency	$f_{\max}$	4.5 GHz
Number of CPU cores	N_c	10

Table 2-7 Simulation Parameters.

As a first result, we compare the proposed optimization method with two benchmarks: *i)* maximum transmit power in each slot (only constrained by the full queue drain) without RIS, and *ii)* power control without RIS, i.e., only the direct channel is used during transmission, but the transmit power is optimized. In Figure 2-23, we show, as a function of the target average received power reduction at the non-intended user location: *i)* the arrival delivery ratio, i.e., the ratio of data arrivals that are accepted into the local queue, based on the implemented flow control (Figure 2-23a); *ii)* the gain in terms of average received power at the non-intended user, with respect to the maximum transmit power benchmark (Figure 2-23b); *iii)* the edge cloud (MEC) power consumption reduction (Figure 2-23c); *iv)* the RIS utilization ratio, i.e., the percentage of time the user decides to use the indirect link to transmit data (Figure 2-23d). It should be noted that the average received power gain is imposed through the long-term constraint. All results are compared at the same E2E delay of 100 ms, and the edge cloud power consumption is adapted for the RIS-aided case to not exceed the scenario without the RIS. In this way, we compare the results with and without the RIS, for the same delay, MEC power consumption and average received power at the non-intended user location.

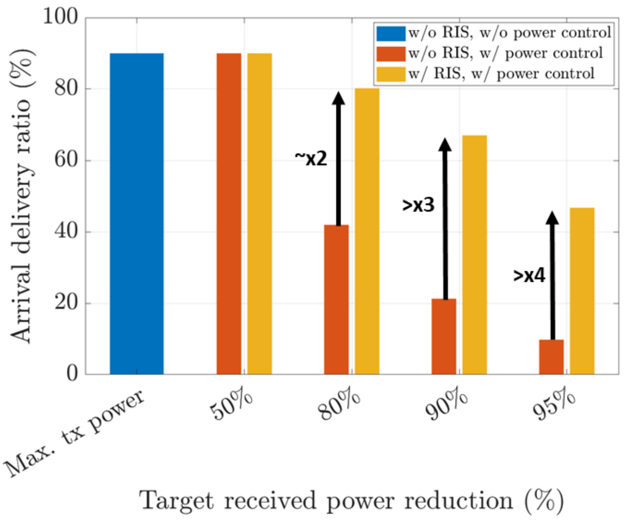

a) Arrival delivery ration vs. different target received power reduction at non-intended user

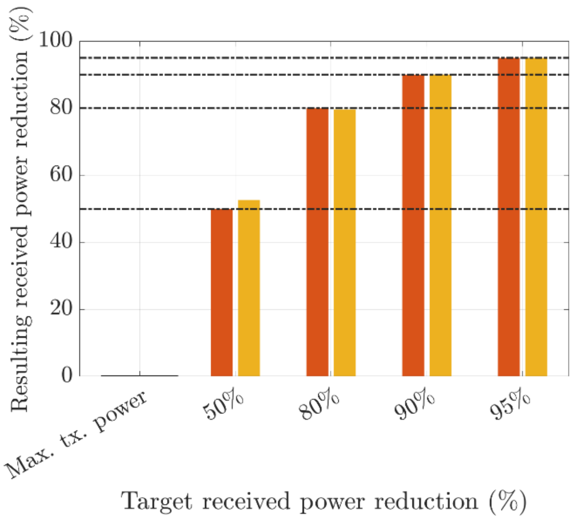

b) Resulting received power reduction vs. target received power reduction at non-intended user

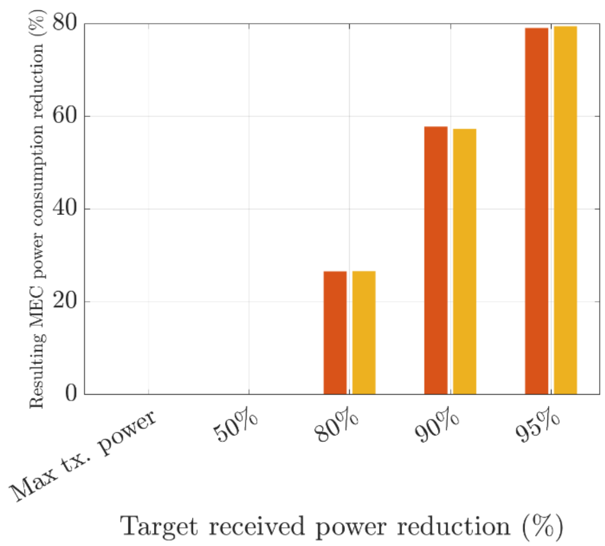

c) Resulting MEC power consumption reduction vs. target received power reduction at non-intended user

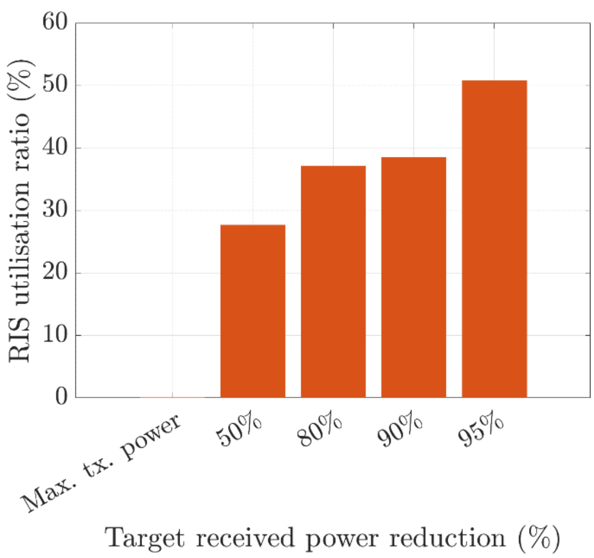

c) Resulting RIS utilization ratio vs. target received power reduction at non-intended

user

Figure 2-23 Trade-offs between arrival delivery ratio, EMF exposure, MEC power consumption, and RIS utilization.

First, we notice how our method is able to guarantee the average power constraint (Figure 2-23 b)), both with and without the RIS. Obviously, the maximum transmit power benchmark has zero gain, as it represents the maximum received power scenario. We can notice how, for less strict constraints (e.g., 50% of the maximum received power), having the RIS does not bring more benefit than a simple power control. This is due to the fact that the transmission can be differed without exceeding the delay constraint. However, with stricter constraints (e.g., 90% of gain), the presence of the RIS is fundamental to achieve better performance in terms of arrival delivery ratio. Indeed, while not having the RIS results in a severe degradation of the acceptance rate, the scenario with the RIS introduces an additional source of resilience to the system, allowing to keep the delivery ratio close to its maximum value. This, without increasing the edge cloud server power consumption with respect to the scenario without the RIS, as visible from Figure 2-23 b). Notably, the resulting arrival delivery ratio still exceeds the one without the RIS, proving that the RIS-aided scenario outperforms the non-RIS one in terms of arrival delivery ratio, average received power at the non-intended user location, and computation power consumption at the edge cloud server. Indeed, the convenience of using the RIS-aided link is visible from Figure 2-23 d), where we notice the increasing RIS utilization ratio, as a function of an increased target reduction of the received power at the non-intended user location.

As a final result, we run exhaustive simulations with different constraints on the received power gain, to evaluate what is the maximum received power reduction one can obtain with the RIS (in the proposed scenario) without decreasing the arrival delivery ratio below the value obtained with the maximum transmit power benchmark, i.e., 90%. By running such test, we obtained a maximum reduction of 75% with respect to the maximum transmit power benchmark, which decreases to 55% without the RIS, i.e. with the simple power control mechanism.

Conclusion

In this section, we proposed a method to jointly control precoding, combining, RIS reconfiguration, transmit power, and edge cloud resources, to maximize the arrival delivery ratio of a MEC service under constraints on EMF exposure (or, received power) at a non-intended user location, MEC power consumption, and E2E service delay. We showed how this joint optimization outperforms benchmark solutions that include a maximum transmit power and a power control mechanisms, both without an with RIS. Different performance assessments have been presented. **Therefore, the proposed scheme boosts the I-EMFEU**. Notably, a 75% received power reduction at the non-intended user location was obtained without any degradation of the service delivery ratio and the MEC power consumption, which also outperforms a simple power control mechanism in a scenario without the RIS. For a given EMF exposure cosntraint, the RIS-aided scheme is able to increase the arrival delivery ratio by a factor up to 4 in the investigated system setting.

2.3 Category C: S-EMFEU Boosting (Uplink)

2.3.1 C1: EE Optimization of RISs with EMFE Constraints

This sub-section summarizes the work detailed in [ZR22].

Introduction

In the area of radio resource allocation for RIS-aided networks, most contributions focus on maximizing the network rate, the EE, or on minimizing the power consumption. At the same time, a relevant issue for future wireless networks is the growing concern for electromagnetic pollution.

While all previous works considered the problem of EMFs aware wireless communications, an EMF-aware scheme for RIS-aided networks is proposed, which is aimed at minimizing the EMF exposure subject to quality-of-service (QoS) constraints. Instead, it is considered the different problem of maximizing the EE in a RIS-aided communication multiple-input multiple-output (MIMO) link, enforcing both maximum power constraints and maximum EMF exposure constraints.

The optimization problem is tackled with respect to the RIS phase shifts, the transmit BF, the linear receive filter, and the transmit power. The EMF constraints are formulated in terms of maximum acceptable values of the specific absorption rate (SAR), which measures the rate of electromagnetic energy absorption per unit mass of human body when it is exposed to a radio frequency EMF.

Two provably convergent algorithms are devised: One applies to the general system setup, but does not guarantee global optimality. The other is provably optimal in the notable special case of isotropic EMF constraints. The numerical results show that the use of an RIS ensures an EE of the same order of magnitude as when EMF constraints are not enforced.

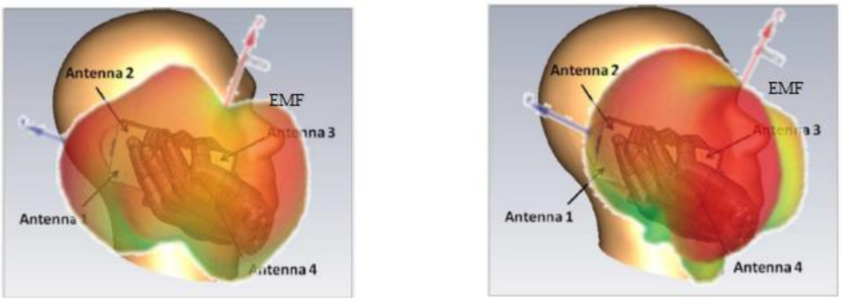

Figure 2-24 Example of EMF exposure for two BF vectors.

System Model

A single-user system in which a transmitter with multiple antennas and a receiver with multiple antennas communicate through an RIS as shown in Figure 2-27. The direct link between the transmitter and receiver is weak enough to be ignored. The RIS has *N* elementary nearly-passive scatterers with. It is assumed that reliable channel estimates are available and that the RIS phases can be set through an RIS controller with minimal signal processing, transmission/reception, and power storage capabilities.

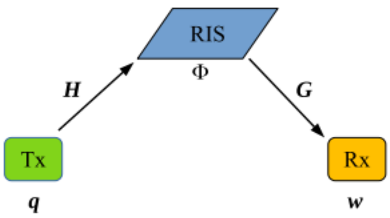

Figure 2-25 System model.

Results

The top of the Figure 2-26 shows the system EE (for *N*=100 RIS elements) as a function of the ratio (noted EMF/c or P_q/c) between the maximum allowed EMF exposure due to the transmit antennas (noted EMF or P_q) and half of the EMFE exposure that would be reached without EMF awareness (noted c and defined in [ZR22]), for all studied schemes (some with EMF awareness, and some others without). Therefore, when the ratio EMF/c=P_q/c is set to 2, it means that the chosen EMF constrain is already met, even without EMF awareness. In this case, there is no real EMF constrain. On the contrary, choosing values of EMF/c=P_q/c below 2, leads the chosen EMF constrain not to be reached without an EMF aware algorithm.

The bottom of the Figure 2-26 shows the EE (for EMF/c=P_q/c=2) as a function of the number of RIS elements, *N*. From Figure 2-26, it is observed that enforcing an EMF constraint on the SAR of the human body reduces the EE, since it narrows the feasible set of the problem. The use of RISs offers, however, the opportunity of achieving the desired EE while ensuring SAR-compliant communications. Figure 2-26 shows, in particular, that, by increasing N, we can attain the same EE as the benchmark system in the absence of EMF constraints, proposed in [ZRS+21]. Moreover, as expected, the SAR-constrained EE tends, for large values of $EMF/c = P_q/c$, to the benchmark EE in the absence of EMF constraints. This is because increasing $EMF/c = P_q/c$ makes the EMF constraint become less relevant.

As illustrated by the bottom part of Figure 2-26, when considering the proposed EMF-aware scheme (b) for a large RIS (i.e. N=700 RIS elements), a mini-RIS (i.e. N=10 elements) under the same EMF constrain (i.e. with $\frac{EMF}{c} = \frac{P_q}{c} = 0.85$) one observes a gain factor in SE of 4.8/3=1.6. This corresponds to a gain factor of 1.6 assuming [D2.4] definition of EMFEU (SE to exposure ratio). Note that **without RIS**, in this simulation scenario, the EMFE constrain would not be met unless zero data is transmitted. Therefore, without RIS, the EMFEU is zero. The EMFEU gain due to the introduction of a RIS is hence infinite and the RIS is an enabler of data communication under EMF constrain.

Finally, this is obtained by using nearly-passive RISs that do not increase the amount of electromagnetic radiation over the air. Comparing the computational complexity of the proposed algorithm to that of its benchmark, we can obtain the performance gain as

$$\mathrm{Gain} = \frac{O(I\ N_T^{\alpha} N_R^{\alpha} N)}{O(I\ N_T N_R N)},$$

where *I* is the number of iterations, α is in the order of the polynomial and it is not available in closed-form, but a known worst-case bound is $\alpha = 4$.

Name	Symbol	Value
Bandwidth	B	5 MHz
End-to-end path loss	δ	110 dB
Receive noise power	N_0	-174 dBm/Hz
The number of transmitter antennas	N_T	4
The number of receiver antennas	N_R	4
Static power consumption	P_c	30 W
Maximum transmit power	P_{max}	20 W

Table 2-8 Simulation Parameters.

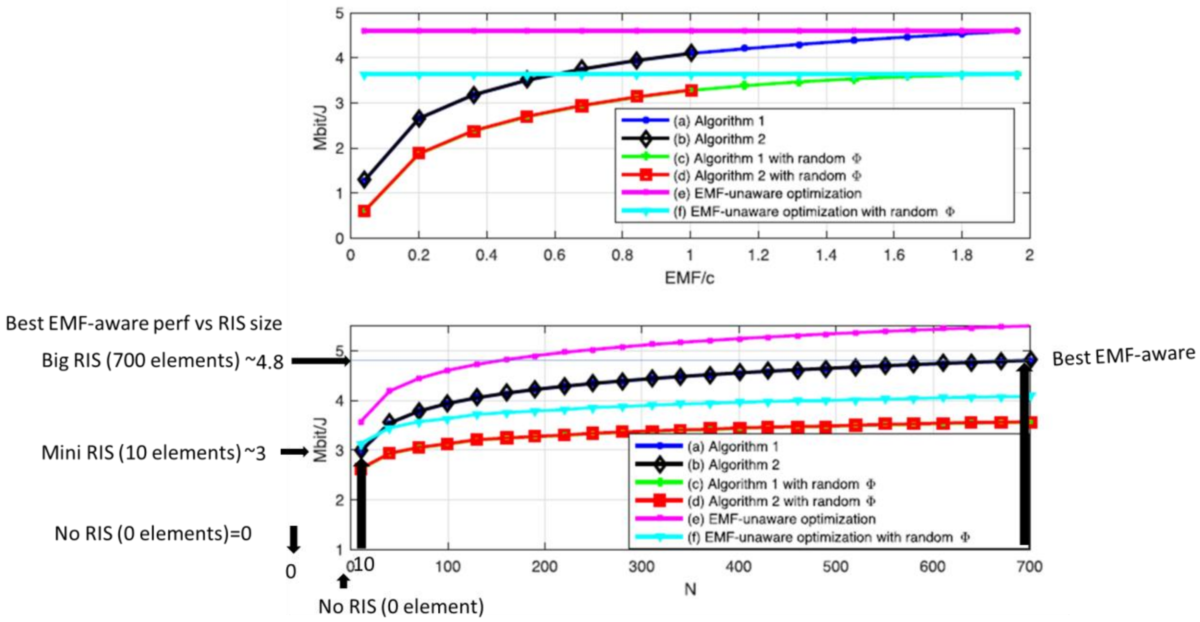

Figure 2-26 Average EE of the six considered schemes as a function of (top) ratio EMF/c for N = 100 and (bottom) as a function of N for P_q/c = 0.85.

Conclusion

Low-complexity optimization algorithms have been proposed for EE maximization subject to EMF constraints. The analysis has shown that the use of an RIS can keep under control the end-users' EMF exposure while ensuring the desired EE level.

In the simulated scenario, without the proposed schemes, the EMF constrain (which is set to 0.86/2=0.43 times the EMF that would be experienced without EMF awareness) cannot be met. In this simulation scenario, the best proposed scheme **enables** data communication under EMF constrain (which is set to 0.86/2=0.43 times the EMF that would be experienced without EMF awareness). By increasing the RIS size from 10 elements to 700 elements, a further S-EMFEU boost is obtained with a gain factor of 1.6. **This advantage (enabler of data communication under S-EMFEU constrain) is reported in the summary Table 2-1**.

2.3.2 C2: Creating and Operating Areas With Reduced Self-EMFE Thanks to RIS

This sub-section summarizes the work detailed in [PBH+22].

Introduction

A macro-cell deployment of MMIMO BSs operating with a sub-6GHz carrier frequency is considered. As illustrated in Figure 2-27, we consider an outdoor-to-indoor environment. The following type of propagation is considered: multiple walls, one single RIS, and non line-of-sight (NLOS). The RIS and walls are close to the target UE and far from the BS. Slow moving or steady UEs only are considered. TDD mode is assumed, such that channel reciprocity can be exploited to acquire full CSI.

RIS-aided Self-EMFE-Aware BF scheme [PBH+22] together with UL closed loop power control is proposed with the following objectives: to deliver an UL voice call with a target QoS from the UE to the BS with minimum transmit power from the target UE, and minimum self-exposure of the customer using the target UE. The proposed scheme is compared to the reference scheme, where no RIS is present.

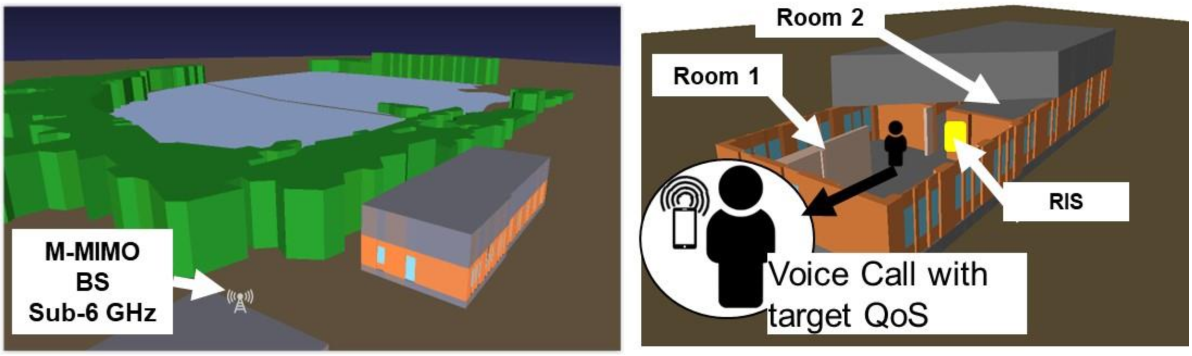

Figure 2-27 Considered deployment scenario.

System Model

The considered carrier frequency is 3.7 GHz. The BS has 32 antenna elements (4 columns and 8 lines) and applies Maximum Ratio Combining (MRC) at the receiver size to detect the UE, i.e. therefore applying a receive BF scheme that focuses on the UE. The RIS is a square array K by K unit-Cells (spaced by half a wavelength). The position of the RIS in Room 1 is illustrated on Figure 2-27. This location has been chosen because the propagation channel between this location and the BS is strong (see details in [PBH+22]) and the RIS is in good position to serve as a passive relay to the BS. The RIS self-configures to “turn itself in the direction of the UE”, following the same protocol as in Scheme A1 to A3, before the UE-to-BS communication starts. Once, the RIS is configured, the UE adapts its transmit power (thanks to an UL closed power mechanism) to reach a target rate for voice call. The service is a voice call of 30 kbps within a 30kHz sub-band (hence a SE of 1 bit/s/Hz), with QPSK modulation and a target signal-to-noise ratio (SNR) of 0 dB. The UE can only use transmit powers between 0 and 23 dBm, due to UE device limitations (due to HW for the minimum value, and due to the standard, for the maximum value). Orange internal Ray Tracing Tool is used to simulate the propagation between each element of the BS and each element of the RIS, the propagation between each element of the BS and each position in the building, and the propagation between each element of the RIS and each position in the building. For each position of the building, we therefore compute the UE transmit power in two scenarios: without and with RIS.

Figure 2-28 illustrates rays between one element of the BS and the center of the RIS. One can observe that waves bounce many times between the building of the BS and the building of the UE, before reaching the RIS. The propagation environment is therefore highly complex and can only be modelled realistically with a ray tracing tool.

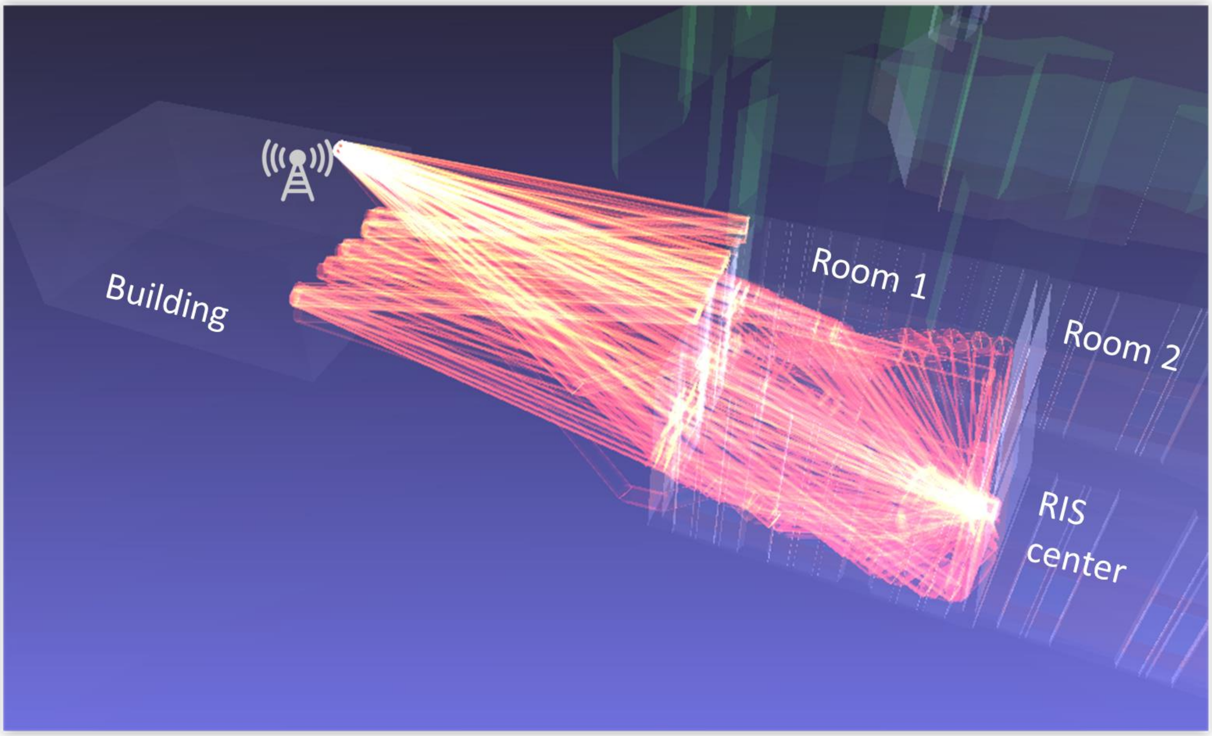

Figure 2-28 Visualization of Rays between one antenna element of the BS and one element at the center of the RIS.

Results

Figure 2-29 (a) plots the map of the UE transmit power as a function of its position in the building, in the absence of RIS. As expected, the UE is in so good radio conditions in room 1 that it reaches the target SNR even with the minimum transmit power of 0 dBm. On the contrary, in room 2, it reaches close to the maximum transmit power (20dBm). In areas where 20dBm is reached, the UE is actually out of coverage (it does not even reach the target SNR even with maximum power). Figure 2-29 (b) plots the map of UE transmit power reduction as a function of its position in the building. As expected, in room 1, as the UE already uses the minimum power it cannot be reduced. On the contrary, in room 2, thanks to the RIS which serves as a passive relay and the improves the UE-to-BS propagation, the UE can reduce its transmit power, and the customer experience a reduction in its self-exposure. Also, coverage is extended. The EMFEU is therefore boosted by a factor of up to 100. Figure 2-29 (c) illustrates the three types of observed areas: an area with no improvement (area where the UE already used minimum power before RIS introduction, or area where the UE is still out of coverage even after RIS introduction), an area with self-exposure reduction, and a coverage extension area (area where the UE was out of coverage before RIS introduction).

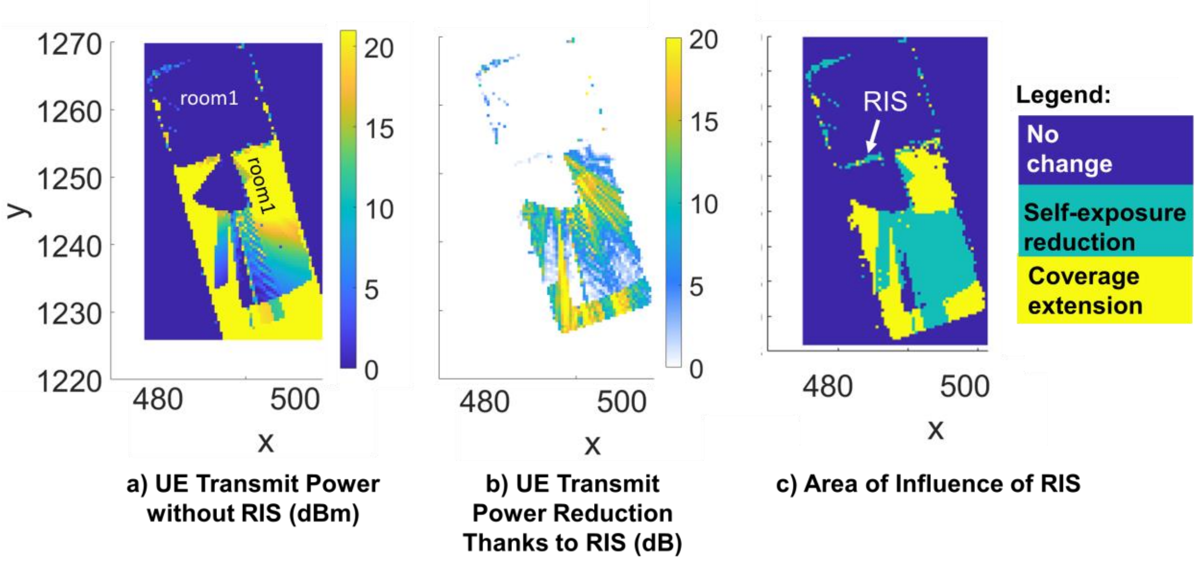

Figure 2-29 Results (maps): transmit power without RIS (a), transmit power reduction (b) and area of influence (c).

Conclusion

The proposed scheme enables to create an area with boosted S-EMFEU. **Therefore, the proposed scheme improves the S-EMFEU. In this boosted area,** S-EMFEU is boosted by a factor of **up to 100.** The RIS also extends the coverage. **In this extended coverage area,** the proposed scheme is **an enabler** of data communication under S-EMFEU constrain. **These advantages are reported in the summary Table 2-1**.

2.4 Category D: SSE boosting, Uplink

2.4.1 D1: On Maximizing the Sum Secret Key Rate for RIS-Assisted Multiuser Systems

This sub-section summarizes the work detailed in [LSX+22].

Introduction

Traditionally, data confidentiality is guaranteed by using encryption methods in existing upper layer protocols. Encryption methods require secret keys that are available only between legitimate parties, but the distribution of the keys is usually challenging, especially in resource-constrained large-scale mobile networks. Interestingly, the inherent stochastic and reciprocal nature of the physical propagation channel can be leveraged to tackle the problem of key distribution between two legitimate users, namely Alice and Bob, in a cost-effective manner. Further, due to spatial diversity, an eavesdropper, namely Eve, obtains no information about the key, if she is not in the vicinity of the legitimate users. This technique for ensuring data confidentiality is referred to as channel reciprocity-based key generation (CRKG) method.

The CRKG comprises four phases: channel sounding; quantization; information reconciliation; and privacy amplification. During the phase of channel sounding, Alice and Bob send pilots to each other in turn, they estimate the channels between them, and they extract appropriate channel features. These features are converted into binary sequences by using quantization algorithms. Then, possible disagreements between the two sequences are corrected during the information reconciliation phase. Finally, the privacy amplification phase is employed to distill the key and wipe out possible information leakage in the previous phases. The security of the CRKG method is ensured by the inherent randomness of the wireless channel. Thus, it may not guarantee the desired secret key rates in harsh propagation environments.

Previous works addressed this problem by utilizing a relay node to help forward the received signals between the two key generating parties, Alice and Bob. However, it is affected by design challenges. First, the relay may obtain partial or complete information about the secret key. Second, the randomness of the secret keys depends on the movement of the relay, but it is impractical and energy consuming to persuade a relay to move all the time.

Due to its feature of controlling the wireless environment, RIS may be a suitable solution for the synthesis of dynamic channels with high entropy, avoiding the mobility requirement for the relay nodes. RIS is viewed as a planar array of nearly-passive reflecting elements, which makes difficult to estimate the instantaneous channel information and derive the secret key. In addition, EE can be increased more than when a relay is used. These advantages of RIS make it a perfect helper to assist Alice and Bob in forming an RIS-induced fluctuating channel, which serves as the common randomness for generating secret keys.

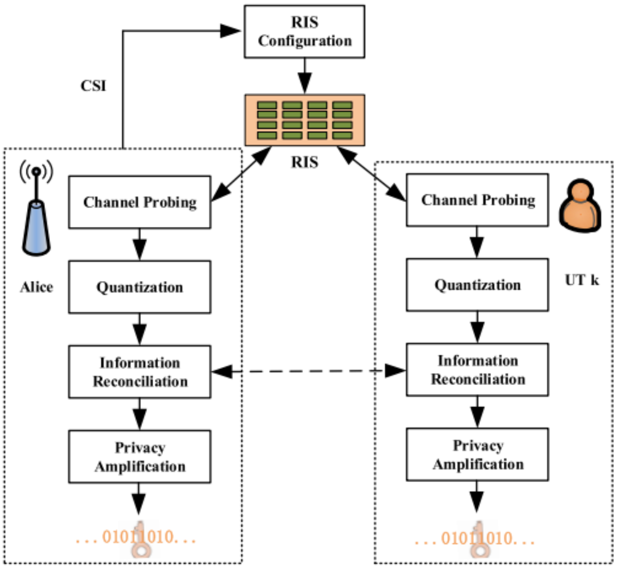

Figure 2-30 RIS-assisted CRKG process, with blockage between Alice and UT's.

System Model

An RIS-assisted multiuser key generation system, which comprises a wireless access point (Alice), an RIS, an eavesdropper (Eve) and multiple legitimate user terminals (UTs), is shown in Figure 2-31. All parties, including Alice, Eve and the UTs, are assumed to be equipped with a single antenna. Alice intends to generate secret keys with the UTs, from the wireless channels between them. A TDD protocol is assumed. The keys generated between Alice and the multiple UTs are not the same. It is assumed that **the direct wireless channels between Alice and the UTs are blocked**, therefore an RIS is deployed to enable the key generation. The phase shifts of the RIS are programmed and reconfigured via a controller.

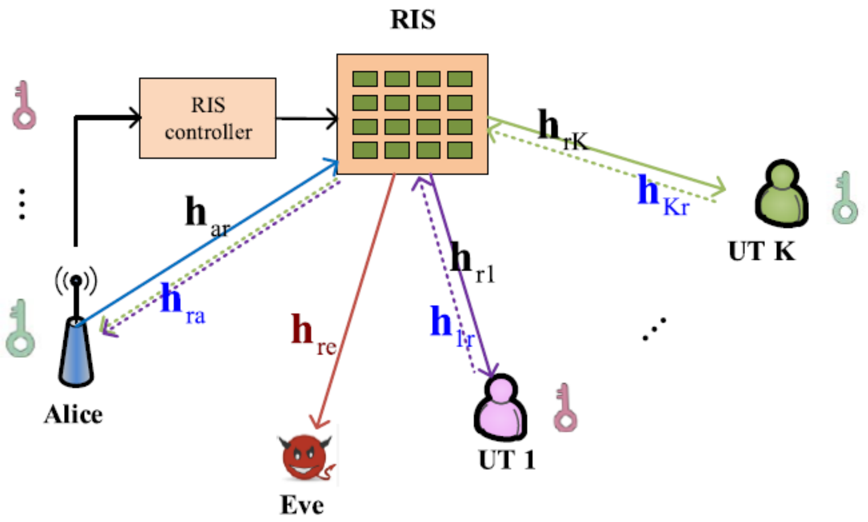

Figure 2-31 System model of an RIS-assisted CRKG scheme, with blockage between Alice and UT's.

Results

Figure 2-32 compares the sum secret key rates for different RIS configurations as a function of the number of UTs: the proposed RIS optimization scheme, the random RIS phase shift scheme, and the on-off switching scheme (turning on only one RIS element at the same time). From the results, the proposed CRKG algorithm with the aid of the RIS achieves the highest sum secret key rate, and the gap between the proposed Algorithm and other algorithms with other simple RIS configurations becomes larger for higher number of UTs. These results indicate that when the number of UTs increases, the advantage of the proposed algorithm is more significant. For instance, when the number of UTs is 8, the proposed algorithm shows the performance gain of about x1.4 compared to the random shifting method. By showing that a sum secret key rate can be improved by using RIS, it can be seen that EE can be also improved when using the RIS instead of relays.

Finally, as the direct paths between Alice and UT's are blocked, such secured communication would not be achievable without the RIS, and the SSE (as defined in [D2.4]) would be zero. Therefore, in this scenario, the RIS is an enabler of secured communication.

Name	Symbol	Value
Signal-to-Noise Ratio	none	10 dB
RIS elements	*M*	16

Table 2-1 Simulation Parameters.

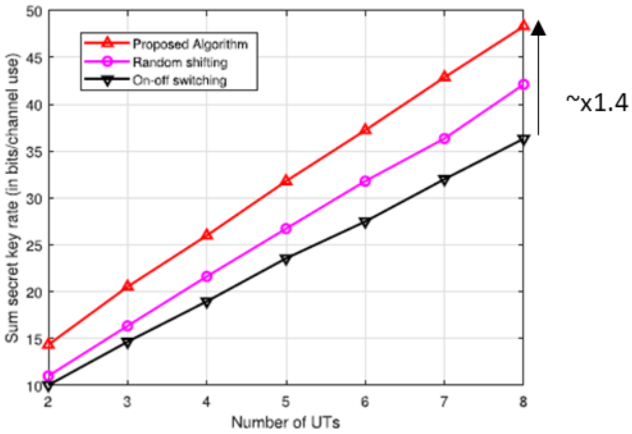

Figure 2-3 Comparison of the sum secret key rates for different RIS configurations versus different number of UTs.

Conclusion

A multiuser secret key generation scheme that capitalizes on the presence of RISs was proposed. The RIS-induced channel model was modeled, and based on this channel model, a general closed-form expression of the secret key rate was derived. In order to achieve the maximum sum secret key rate, we formulated and solved an optimization problem to obtain the optimal RIS configuration over independent and correlated channels among the UTs. Numerical results demonstrated that the proposed scheme provides the highest sum secret key rate as compared with existing benchmark schemes. Finally, as in the simulated scenario, the direct paths between Alice and UT's are blocked, the RIS is an **enabler of secured communication**. **This advantage is reported in the summary Table 2-1.**

2.5 Category E: SSE boosting, Downlink

2.5.1 E1: Safeguarding MIMO communications with reconfigurable metasurfaces and artificial noise

This sub-section summarizes the work detailed in [AKW+21].

Introduction

Physical layer security (PLS) belongs to one of the various applications that can certainly be enhanced by RISs in beyond 5G wireless networks, according to the recent literature. However, as each wireless technology can be utilized by the legitimate side to assist the target of achieving its objectives, likewise an RIS can also be used on behalf of an eavesdropper (Eve) to assist its attempt to decode the transmitted confidential messages between a legitimate transmitter-receiver pair. In this contribution, a multi-stream MIMO PLS system is studied, under the assumption that there exists a legitimate as well as an eavesdropping passive RIS. Focusing first on the eavesdropping subsystem, we present a joint design framework for the eavesdropper's combining matrix and the reflection coefficients of the eavesdropping RIS. Then, by formulating and solving a novel joint design problem for the legitimate subsystem, we propose a PLS scheme incorporating legitimate precoding and AN, receive combining, and passive BF from the legitimate RIS.

System Model

The considered system model (depicted in Figure 2-32) consists of a BS equipped with N antenna elements, a legitimate receiver (RX) possessing M antennas, a legitimate RIS with L unit cells, a multi-antenna Eve with K ($K \geq M$) and an eavesdropping RIS of Λ unit elements. Both RISs are assumed to be located close to the intended and non-intended receivers (RX and Eve, respectively). The transmission of confidential information is assumed to happen in the downlink direction. We assume that the legitimate RIS is connected to the legitimate node via dedicated hardware and control signaling for online reconfigurability; the same holds for E and the eavesdropping RIS. The BS knows about the existence of Eve and focuses on securing its confidential link with RX; however, it is unaware of the presence of the eavesdropping RIS. It is also assumed that the deployment of the legitimate RIS is transparent to Eve.

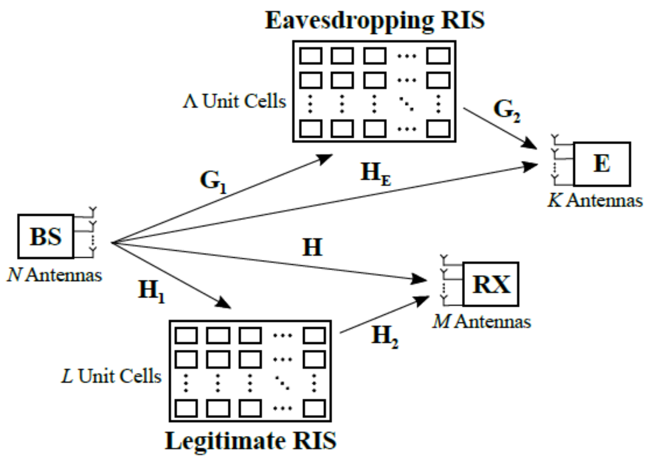

Figure 2-32 The considered PLS system comprising three multi-antenna nodes and two multi-element RISs.

In addition, it is assumed that perfect channel information is available at the BS and Eve sides via pilot-assisted channel estimation. Specifically, BS possesses the channels referring to the BS-RX, BS to legitimate RIS, and legitimate RIS links to RX. It is also assumed that BS and Eve cooperate in order to both estimate the BS-Eve channel, according to the following exchange of transmission signals: BS transmits pilot signals to Eve that estimate the channel matrix $\boldsymbol{H}_E$ and then feeds this estimation back to BS. This cooperation may apply to the case where Eve plays the dual role of a legitimate receiver and an eavesdropper. Since the BS is unaware of the existence of the eavesdropping RIS channel $\boldsymbol{G}_1$ and the eavesdropping RIS to Eve channel $\boldsymbol{G}_2$. However, the latter two channels are assumed at Eve's side based on various channel estimation techniques proposed in the literature. It is, finally, assumed that due to obstacles there are no actual channels between the legitimate RIS and Eve, and the eavesdropping RIS and RX.

Results

To evaluate the secrecy performance of the proposed PLS scheme, we considered frequency flat Rayleigh fading channels with zero mean and unit variance for all involved links. In the simulations, the BS was located in the in the origin of the xy plane, whereas RX and Eve lied on a circle of radius 10 m in the angles 45^o and 85^o , respectively, from the BS. The first unit element of the eavesdropping RIS was placed in the middle of the line connecting RX and Eve, and the other elements expand along the positive directions of the x and y axes. Similarly, the legitimate RIS is place in the same circle as RX and Eve, in the angle 20^o from BS. In addition, we have used the parameters' setting presented in Table 2-9.

Name	Symbol	Value
Transmit antennas at BS	N	{8,16}
Antennas at RX	M	4
Antennas at Eve	K	{4,8}
Legitimate RIS's elements	L	{20,30}
Eavesdropping RIS's elements	Λ	{30,50,100, 150}
Noise variance	σ^2	1

Table 2-9 Simulation Parameters.

In Figure 2-33, we have considered that the legitimate system does not include an RIS, and target at securing confidential transmissions with only BS precoding and artificial noise (AN). It can be observed that the rates follow a non-decreasing trend with increasing SNR for both the legitimate and eavesdropping links. It is illustrated that RX's rate is larger than Eve's rate for $\Lambda = 50$. However, when Lambda increases (for $\Lambda = 50$ and $\Lambda = 150$) Eve's rate is similar or larger than that of RX. Therefore, based on this behavior, it can be deduced that with the proposed schemes for RX and Eve, **the secrecy rate (or SSE) equals zero**. For such cases, BS precoding and AN are not sufficient to provide security to the legitimate link. The latter observation can be explained by the fact that BS is unaware of the presence of the eavesdropping RIS. Hence, it is crucial for the legitimate side to counteract this behavior.

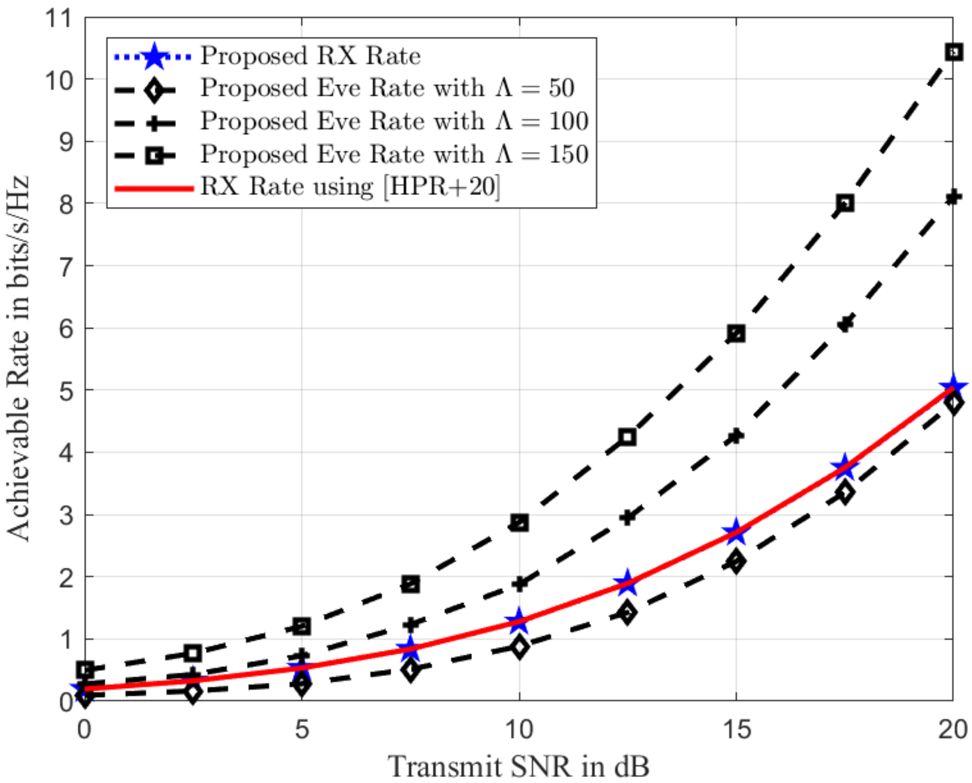

Figure 2-33 Achievable rates at the legitimate RX and Eve versus the transmit SNR in dB for N = 8 BS antennas and different numbers for the unit elements at the eavesdropping RIS.

In Figure 2-34, we consider that the legitimate system deploys an RIS with L unit elements and thus optimizes the RIS in order to maximize the achievable secrecy rate. In particular, in Figure 2-34 we have plotted the achievable secrecy rates versus the transmit SNR for different numbers of BS antennas and elements at both deployed RISs. As illustrated, using the proposed design and a baseline scheme from the recent literature, the deployment of the legitimate RIS with even more than 500% less elements than the eavesdropping one, results in **positive secrecy rates (SSEs)** for all considered SNR values. Therefore, in these simulations, the gain in SSE due to the introduction of a legitimate RIS is infinite. Hence, the proposed schemes with a **legitimate RIS**, **enable secured data communications.**

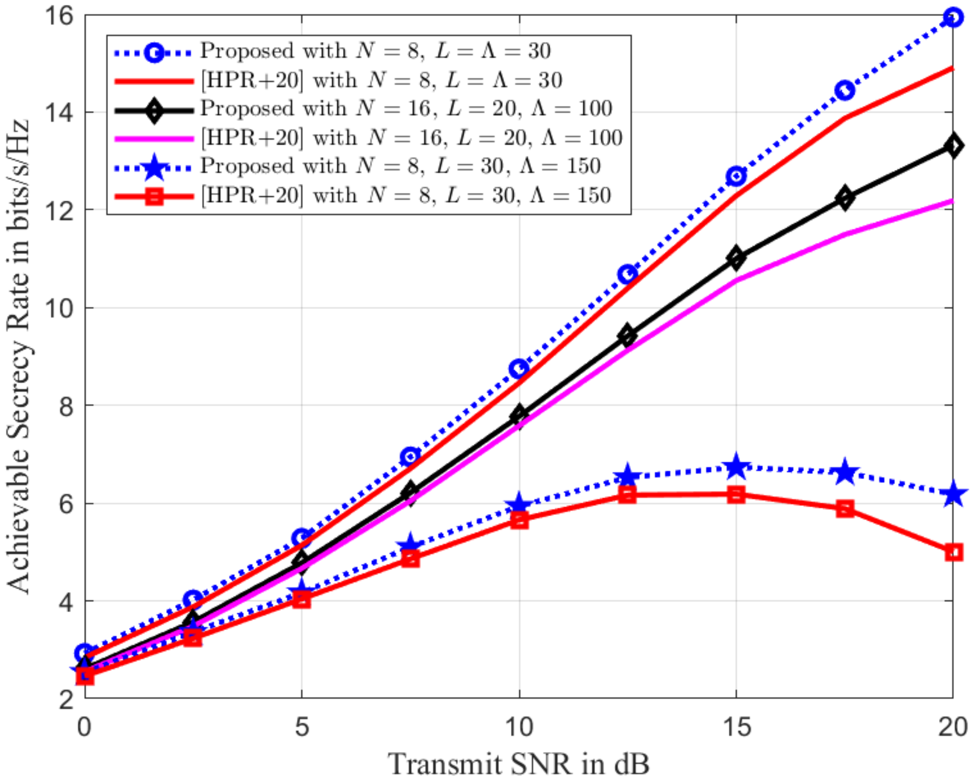

Figure 2-34 Achievable secrecy rates versus the transmit SNR in dB for various values of the number of antennas at the BS, RX, and Eve and numbers of elements for both RISs.

Conclusion

In this section, we proposed an RIS-empowered MIMO PLS communications system, where RISs are deployed from both the legitimate and eavesdropping systems. According to the numerical results, it was shown that the legitimate system was capable of safeguarding MIMO communication over much larger RIS on behalf of the eavesdropping side. The proposed schemes with a legitimate RIS **enable a secure data communication**. **This advantage is reported in the summary Table 2-1.**

2.5.2 E2: Counteracting eavesdropper attacks through RISs: A new threat model and secrecy rate optimization

This sub-section summarizes the work detailed in [AKW+23].

Introduction

In this section, we consider a multi-stream MIMO system operating in the vicinity of a multi-antenna eavesdropping system, where each side deploys a passive RIS which is transparent to the other system. We assume statistical CSI knowledge with respect to the eavesdropping links at the legitimate system, while partial CSI is available at the eavesdropping system. Each sub-system designs its free parameters according to the knowledge it has access to with respect to the other one. For instance, the eavesdropping system design the eavesdropper's combining matrix and the reflection coefficients of the malicious RIS aiming at maximizing its received rate, while for the legitimate one whose target is the maximization of secrecy rate the linear precoding and AN, as well as the receive combining and the reflective BF from the legitimate RIS are jointly designed. The proposed framework for the legitimate system explicitly optimizes the number of transmitted data streams.

System Model

The system model in Figure 2-35 consists of an N-antenna legitimate BS aiming to communicate in the downlink with a legitimate RX having M antennas. The transmission of the confidential streams is assumed to be further empowered by a legitimate RIS with L reflecting elements, which is placed either close to the BS or RX. In the vicinity of the legitimate BS-RX link exists a K-antenna eavesdropper (Eve) whose overhearing is assisted by an RIS equipped with Λ reflecting elements.

We assume that the legitimate RIS is connected to the legitimate node via dedicated hardware and control signaling for online reconfigurability; the same holds between Eve and the malicious RIS. The BS is assumed to know about the existence of Eve and focuses on securing its confidential link with RX; however, being unaware of the presence of the malicious RIS. The deployment of the legitimate RIS, to boost the performance of the legitimate side is also considered to be unknown to Eve. It is assumed (without loss of generality) that the malicious RIS is located close to Eve and in the LOS from the legitimate BS. Such an assumption is valid since the control of the malicious RIS by Eve eases eavesdropping capability because the channel between the malicious RIS and the legitimate BS can be easier estimated by Eve.

Based on this model, we design the receive combining matrix of Eve and the reflection coefficients of the malicious RIS. Then, focusing on the legitimate system, the maximization of the secrecy rate is subject to the legitimate precoding matrix and number of data streams, the AN covariance matrix and the reflective BF of the legitimate RIS.

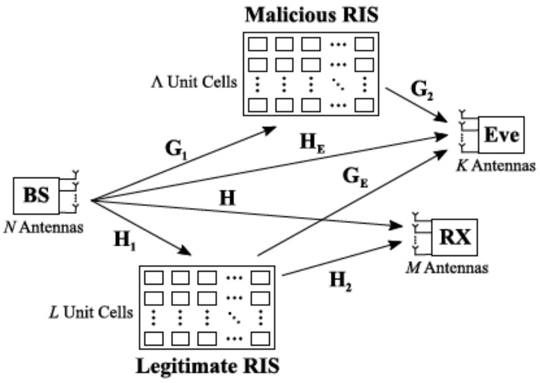

Figure 2-35 The considered RIS-empowered PLS communication system.

Results

The performance of the proposed PLS scheme was investigated by numerical evaluations of the actual achievable rates of the legitimate and eavesdropping links to provide the overall secrecy rate. All nodes were considered positioned on a 3-Dimensional coordinate system, whose xy plane is illustrated in Figure 2-36. In addition, for the various simulation parameters the values indicated in Table 2-10 were used.

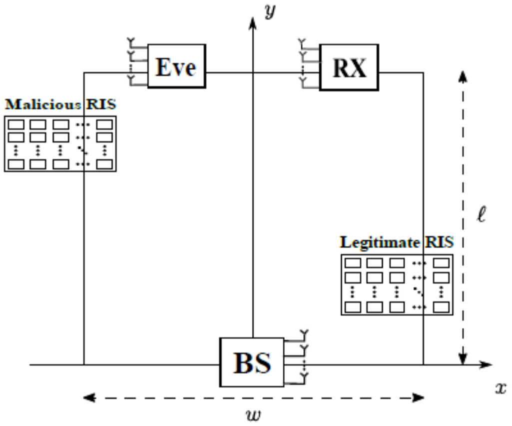

Figure 2-36 The xy plane of the simulated RIS-empowered MIMO PLS system.

Name	Symbol	Value
Transmit antennas at BS	*N*	{8,16}
Antennas at RX	*M*	4
Antennas at Eve	K	{4,8}
Legitimate RIS's elements	*L*	{10,20,50}
Eavesdropping RIS's elements	Λ	{20,50,100,150,200}
Noise variance	σ^2	-105 dBm
Transmit Power	*P*	∈ [10,40] dBm

Table 2-10 Simulation Parameters.

We first consider the case where **the legitimate system does not include an RIS** and attempts to guarantee secrecy with only BS precoding, AN and RX combining. In Figure 2-37, the achievable rates at both RX and Eve are depicted, as functions of the BS transmit power for various values Λ for the elements of the malicious RIS. It is shown that Eve's rate increases with increasing Λ, verifying that the malicious RIS can offer gains and boost its overhearing capabilities. For $P > 35$ though, the achievable rates at Eve saturate for any Λ value, which happens because the AN is transmitted with larger power. **For the particular case of $\boldsymbol{\Lambda = 50}$, without RIS, the proposed scheme has a null SSE for $\boldsymbol{P < 31.6}$ and positive SSEs for $\boldsymbol{P > 31.6}$.**

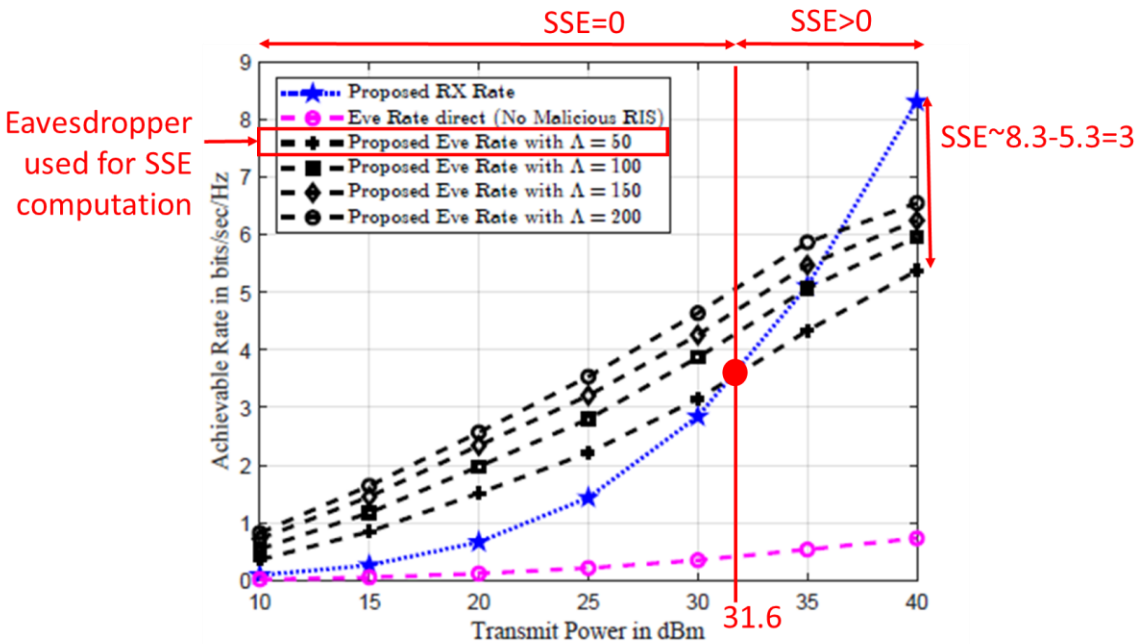

Figure 2-37 Achievable rates in bps/Hz at the legitimate RX and Eve versus the transmit Power P in dBm.

In Figure 2-38, the achievable secrecy rates for both Eve's CSI (ECSI) knowledge schemes are illustrated as function of P, considering different values for L and Λ. As it is shown, all rates follow a non-decreasing trend for increasing values of P. It can be also inferred that the statistical knowledge of the eavesdropping channels at the BS combined with the partial CSI knowledge for the channel between the BS and the malicious RIS, leads to larger secrecy rates compared to the perfect ECSI, where both the BS and Eve possess all channels perfectly. Interestingly, it is also illustrated that the proposed design outperforms the benchmark scheme [F+19] (indicated by the dash line). **For the particular case of $\Lambda = 50$, the proposed scheme achieves positive secrecy rates (or SSEs). Therefore, compared to the scheme without RIS, the proposed RIS-aided schemes enables secured data communication for $P < 31.6$, and boosts the SSE by up to a factor of x7, for $40 > P > 31.6$.**

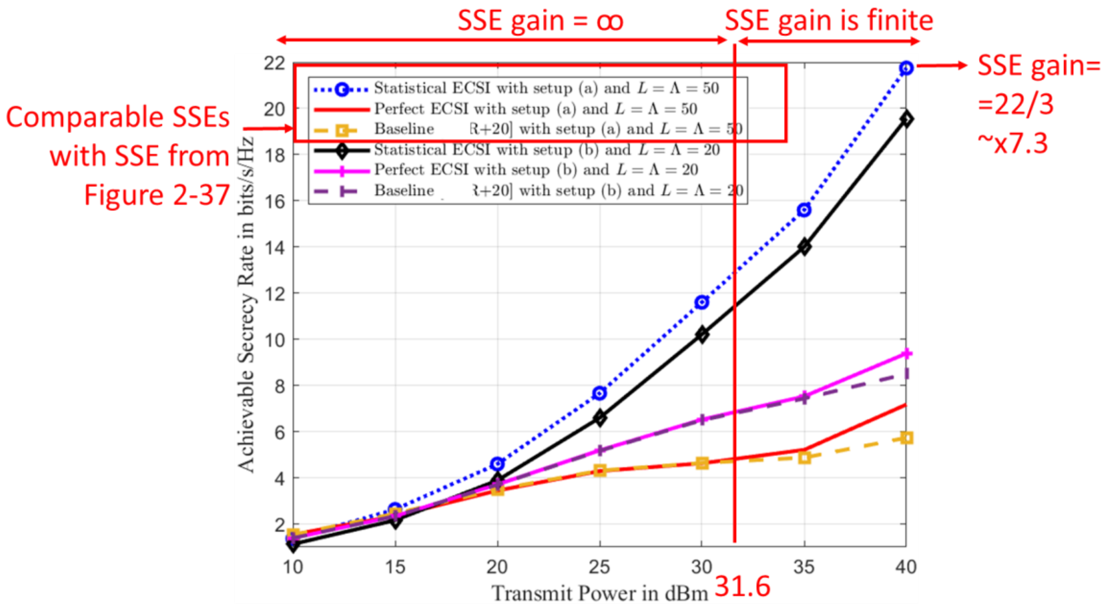

Figure 2-38 Achievable secrecy rates in bps/Hz versus the transmit power in dBm considering different number for L and Λ.

Conclusion

We studied an RIS-empowered multi-stream MIMO PLS communication system, with two RISs each dedicated to assist the legitimate and the eavesdropping systems, respectively, for the realistic case of limited CSI knowledge at both sides. Focusing on the case where the malicious RIS is placed close to Eve, we presented a novel threat model for RIS-boosted eavesdropping systems by designing the receive combining matrix and the reflection coefficients of the malicious RIS. Then, the emphasis was given to the legitimate system, by designing joint countermeasures such as the precoding matrix, the AN covariance matrix as well as the legitimate RIS. In the simulated scenarios, in some cases the proposed scheme enables a secure data communication, in other cases it boosts the SSE by a factor of up to x7. **These advantages are reported in the summary Table 2-1.**

2.5.3 E3: Reconfiguring wireless environment via intelligent surfaces for 6G: Reflection, modulation, and security

This sub-section summarizes the work detailed in [XYH+23].

Introduction

Communication security and EE have been attracting vast investigations for the future networks. With ubiquitous wireless services in multifarious areas, communications are becoming more vulnerable to eavesdropping in the future networks. However, strict secure communications are contrivable from the physical layer. The physical-layer security is designed by exploiting physical-layer characteristics like measurements of channel propagations. The physical-layer security has been shown achievable under high-frequency mmWave channels by developing a practical secure transmission scheme in the beam domain. Particularly, by using RIS, we can achieve the physical-layer security with more energy efficient ways instead of using cost-high hardware such as relays. Exploring this high-frequency spectrum, RIS can be utilized to reconfigure the propagation environment so that the physical-layer security is enhanced by improving the communication reliability of legitimate terminals while suppressing the leakage of information to eavesdroppers.

In [XYH+23], it is exposed that RIS provides a cost-and-power efficient solution to coverage extension and rate boosting for the 6G communications. Besides, we evince the paramount importance of security in the 6G network and highlight the significant contributions of RIS to guarantee secure communications at the physical layer.

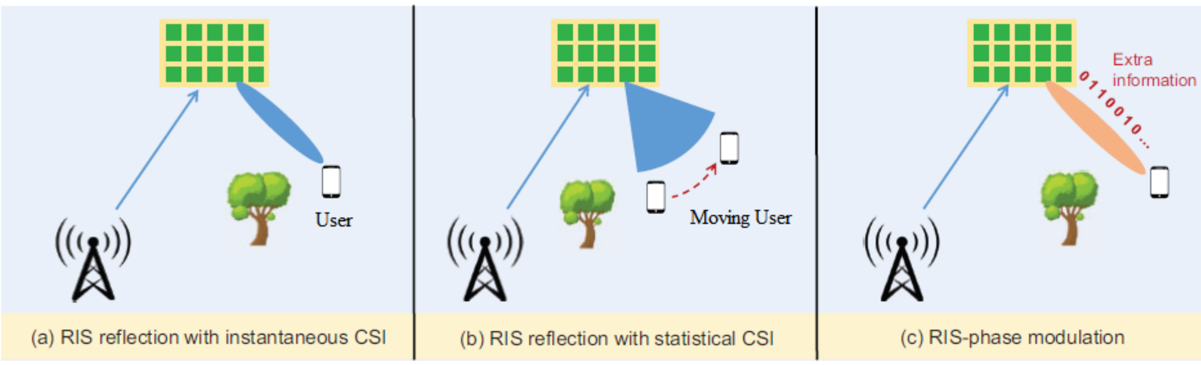

Figure 2-39 RIS reflection and modulation.

System Model

A typical three-terminal wiretap channel, where a multi-antenna transmitter (Alice) sends confidential signals to a desired receiver (Bob) in the presence of an eavesdropper (Eve), is shown in Figure 2-40. Under the assumption that the LOS path between Alice and Bob/Eve is blocked, an RIS is exploited to assist the secure communication. It is assumed that the RIS is equipped with multiple reflecting elements while Alice exploits multiple antennas. Bob and Eve are single-antenna receivers. Due to the spatial sparsity of mmWave MIMO channels, assume that all the channels in this system are dominated by LoS paths. The Alice-RIS, RIS-Bob, and RIS-Eve channels are defined with signature response vectors and large-scale fading.

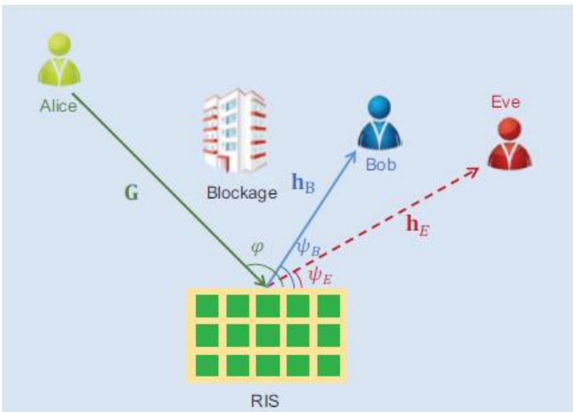

Figure 2-40 A secure mmWave communication system assisted with an RIS.

Results

Figure 2-41 verifies the tightness of the derived lower bound in [XYH+23]. The secrecy rate increases with the number of antennas at Alice, *M*, and finally tends saturated as shown in Figure 2-41 (a). A large number of transmit antennas provide more degrees of freedom at Alice, which is equally beneficial to both Bob and Eve. Its bonus to the secrecy rate is thus limited. On the other hand, the secrecy rate monotonically increases with the number of RIS elements, *N*, in Figure 2-41 (b). More efficient BF toward Bob can be realized by a larger number of reflecting elements at RIS, making it more challenging for Eve to wiretap.

Name	Symbol	Value
Transmit power	*P*	20 W
Noise spectral density	N_0	-174 dBm/Hz
Bandwidth	*B*	100 MHz
The number of RIS elements	*N*	8
The number of antennas at Alice	*M*	4 or 8

Table 2-11 Simulation Parameters.

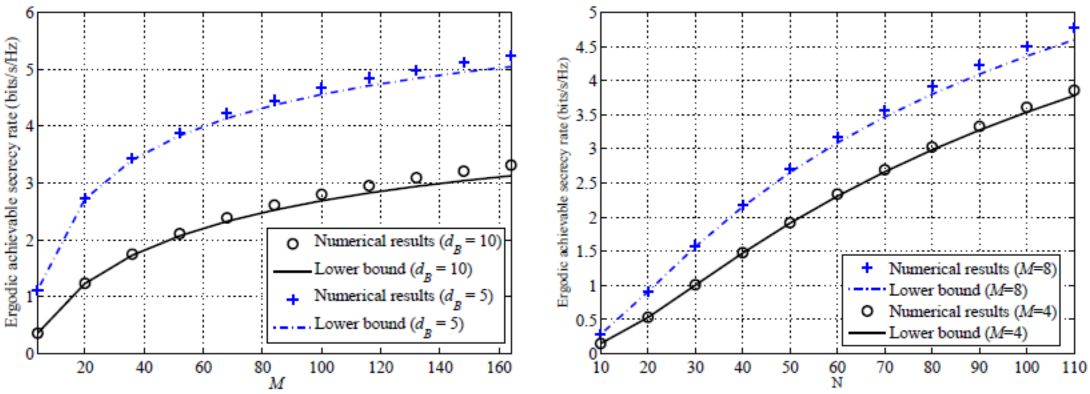

(a) $N = 8$, $d_A = 10$, and $d_E = 30$. (b) $d_A = 15$, $d_B = 20$, and $d_E = 30$.

Figure 2-41 Ergodic achievable secrecy rate versus *M* and *N*.

In the simulated scenario (in Figure 2-41 (b)) terms of Ergodic achievable secrecy rate, **without a RIS, the secrecy rate would be null**. Therefore the SSE gain due to the use of a RIS is infinite, and the RIS is an **enabler of secured data communication**.

Conclusion

To meet the prominent requirement in terms of secure communications in 6G networks, it was discussed on the contributions of RISs to enhance physical-layer security in terms of secrecy rate and (secrecy outage probability) SOP. In particular, we propose a typical case study exemplifying the benefits of RISs to secure communications. Both theoretical analysis and simulation results demonstrate the impact of RISs on the ergodic secrecy rate. Consequently, by the use of the RIS, the better physical-layer security can be achieved with low hardware cost and better EE compared to the use of other types of relaying hardware. In the simulated scenario, the RIS is an **enabler of secured data communication**. **This advantage is reported in the summary Table 2-1.**

2.5.4 E4: Surface-Based Techniques for IoT Networks: Opportunities and Challenges (EE and security)

This sub-section summarizes the work detailed in [ZRF+22].

Introduction

The 5G technologies focus primarily on increasing the network data rate and throughput. However, being simply able to transmit data at a faster rate does not ensure the flexibility required to accommodate diverse classes of end-users with heterogeneous service requirements such as in IoT. In particular, three major requirements of IoT applications, which 5G technologies are not able to properly address, are the need for: (1) EE; (2) intelligent communication and sensing; (3) wireless security.

The EE of wireless networks is traditionally defined as a benefit-cost ratio, where the benefit is the amount of reliably transferred information per unit of time, and the cost is the required power. Although the EE of 5G networks is higher compared to the fourth generation (4G) systems, the increase is not significant. As a result, EE is still a major issue, which has a negative impact on both environmental sustainability and maintenance costs of wireless networks. The energy crunch is even more significant in IoT applications, and it limits the use of mmWave, which has been envisioned for IoT in order not to overcrowd the sub-6GHz bandwidth. Indeed, mmWave require large antenna arrays to provide high BF gains and combat the high attenuation. Unfortunately, this is not feasible for IoT systems, because the use of large arrays of traditional antennas would inevitably lead to an unacceptable increase of the energy consumption.

While RISs are assumed to be nearly-passive devices with little energy requirement. When used to coat environmental objects, RISs provide a densification effect similar to the use of small-cells, but with a much lower energy consumption and hardware complexity. Similarly, if used close to a transceiver, RISs could provide a channel hardening effect similar to a MMIMO array by using a large number of reflecting elements, but with a much lower energy consumption and hardware complexity.

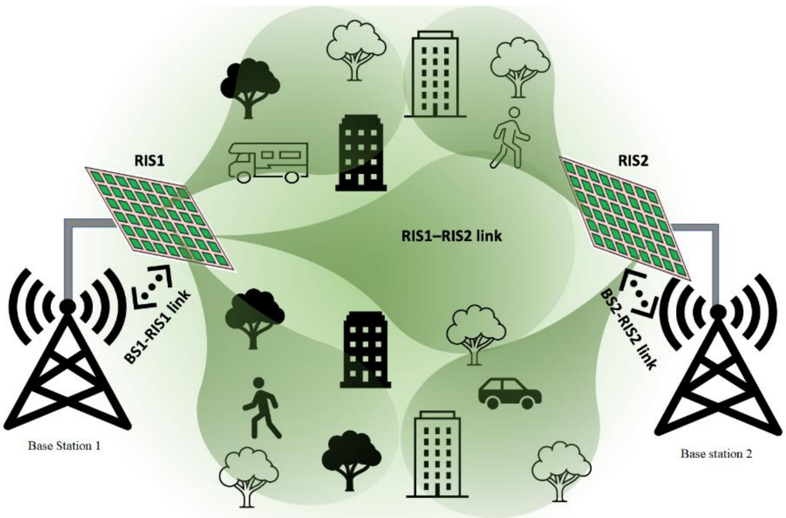

Figure 2-42 Use of holographic/RIS surface.

System Model

It is considered that a single-user system in which a RIS with N_T reflecting elements is deployed 5m away from the transmitter and another RIS with N_R elements is deployed 5m away from the receiver.

The transmitter and receiver are separated by 300 m. The fading component of the MIMO channel between the two RISs has been generated following the Rice model with the power of the direct path twice as large as the power of the multi-path component, while the path-loss of the MIMO channel as well as the channels from the transmit antenna to the transmit RIS and from the receive antenna to the receive RIS have been generated RIS-specific models.

Results

Figure 2-43 shows (a) the maximum EE obtained by the RIS-based holographic transceiver by optimizing the transmit and receive RIS phase shifts and the transmit power, as a function of the number of antennas/elements, *N*; and (b) the maximum EE obtained by the fully digital MIMO by optimizing the transmit and receive filters. Thus, *we consider that the digital MIMO system has a per antenna static power consumption ten times larger than the power consumption of each reflecting element of the holographic surfaces, due to the more complex hardware.* Interestingly, it is seen that the EE obtained by the holographic-based transceiver is significantly larger than that of the MIMO system with digital transmit and receiver filters for the whole considered range of *N*. Thus, the holographic-based transceiver is more energy-efficient and thus it allows for the possibility of deploying a larger number of reflecting elements than the number of active antennas, while maintaining a higher EE than the digital MIMO transceiver. Of course, as the trend of the figure shows, further increasing *N* will eventually cause the holographic-based system to become less energy-efficient than the digital MIMO system.

Name	Symbol	Value
Noise spectral density		174 dBm/Hz
Bandwidth	W	1 MHz
System static power consumption	$P_{c,0}$	10 dBW
Maximum transmit power	P_{max}	20 dBW

Table 2-12 Simulation Parameters.

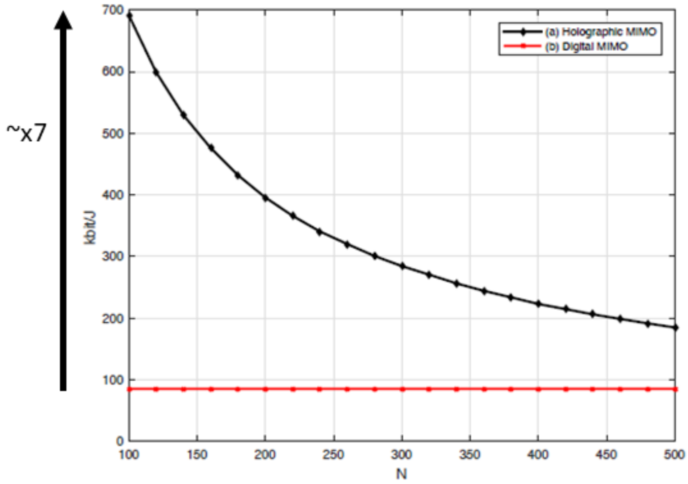

Figure 2-43 EE versus *N*.

The proposed scheme improves the EE by a factor of x7 compared to the reference scheme, and assuming 100 RIS elements.

Conclusion

Most research contributions focus on the optimization of the rate and throughput of surface-based networks, while the issue of EE has not received enough attention. This appears a crucial point to investigate, given the stringent energy requirement of IoT services.

The use of holographic surfaces poses the issue of developing energy consumption models tailored to this new scenario and the study of the channel models and multiplexing strategies for holographic-based transceivers should be deepened, as only preliminary results have been obtained. At the same time, the comparison between active and passive surfaces, especially in terms of EE should be addressed in more detail.

This work has shown how surface-based communications can provide a formidable tool for IoT applications, thanks to their reduced energy consumptions and programmability potential.

Therefore, the proposed scheme boosts the secrecy. The proposed scheme improves the EE by a factor of x7 compared to our reference scheme, and assuming 100 RIS elements. **This example of gain value is reported in the summary Table 2-1.**

2.5.5 E5: Spatial Secrecy Spectral Efficiency Optimization Enabled by RISs

This sub-section summarizes the work detailed in [KA23].

Introduction

According to many recent studies related to RISs, it is evident that they can provide significant advantages PLS systems, by enhancing the performance gains with respect to various performance metrics, such as secrecy rate, secrecy outage probability or their combination. However, most of the existing works rely on the assumption that the far-field positions of the receiving nodes are fixed, while evidently an RIS affects its surrounding area. In this section, we investigate the RIS-enabled secrecy performance under the consideration that all receivers belong to given geographical areas. To characterize the secrecy performance of an RIS, a new metric is introduced, termed as spatial secrecy spectral efficiency, which does not need the instantaneous knowledge of the receivers' exact positions. Then, aiming at the maximization of the proposed metric, which can be expressed as a function of the transmit digital BF and the RIS's phase configuration profile, a challenging optimization problem is formulated, whose solution can yield significant gains.

System Model

The considered system model consists of a BS equipped with $\boldsymbol{N}$ antenna elements whishing to communicate in the DL direction with a legitimate single-antenna RX. There also exists a single-antenna Eve, in the vicinity of the legitimate pair. However, the direct links between the BS and both (intended and non-intended) receivers are assumed to be blocked. To overcome this situation, an RIS with $\boldsymbol{L}$ unit cells is deployed near the receivers' area. It is further assumed that partial CSI knowledge is available for the wireless links. Specifically, the statistics of the channels between the RIS and the two receivers are known up to their second order statistics, while the channel between the BS and the RIS is perfectly known.

Taking into account that both RX and Eve are located within a given geographical area S, which is the union of each receiver's area (with their intersection equal to the empty set), we further assume that each point of S is associated with a probability density function (PDF) $u(S)$. Aiming at safeguarding communications for each placement of RX and Eve within their corresponding areas (S_{RX} and S_E, respectively) the proposed *spatial secrecy spectral efficiency* can be defined as the spatially averaged secrecy rate metric, integrated over all possible positions of the two nodes. Based on this definition and assigning it as the objective function of the optimization problem, whose free parameters are the BS's precoder and the RIS phase shift profile, the characterization of the RIS's impact on each area can be evaluated.

Results

The achievable rates of the legitimate and eavesdropping links can be evaluated based on the proposed design previously described. To simulate the system, a 3D Cartesian coordinate system was used. Assuming specific locations for the BS and the RIS, but not for RX and Eve, since the latter nodes belong to specific geographical areas with uniform distribution, we let similar pathloss properties for each of receiver, since this assumption serves as a worst-case scenario for the legitimate side. For comparison purposes we have implemented two baseline schemes: the “Random” scheme including random linear precoding and passive BF vectors; and the “RX Only” scheme, according to which the maximization of the spatial spectral efficiency only for RX is considered.

Name	Symbol	Value
Transmit antenna at BS	N	16
RIS elements	L	150
Rician factor	K_r	13.2
Noise variance	σ^2	-105 dBm
Transmit Power	P_T	35 dBm

Table 2-13 Simulation Parameters.

In Figure 2-44, the impact of the RIS at the entire regions is investigated, by evaluating the gain of the two optimized schemes with respect to the random setting scheme, as previously described. It can be observed from all subfigures that there exist regions where the RIS enhances or degrades the rate at both receiving nodes. It is also shown that the rate gains via both optimized schemes are more pronounced at the RX rather than at Eve, which is evident from the more yellow-colored areas that indicate larger gains with the optimized schemes. The proposed scheme can yield gains for an entire area, which can reach more than 50% close to sub-regions near the RIS. Compared to a scheme without RIS, the proposed scheme would provide an even larger gain, and therefore a gain larger than x1.5.

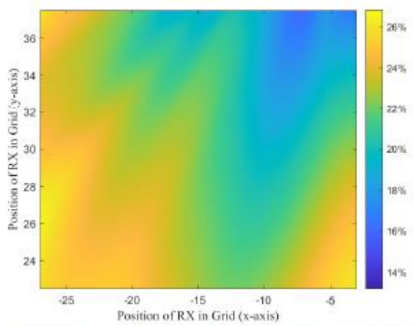

(a) Spatial rate gain at RX between the random configuration and the “RX Only” scheme.

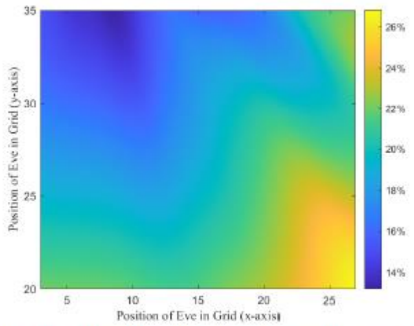

(b) Spatial rate gain at Eve between the random configuration and the “RX Only” scheme.

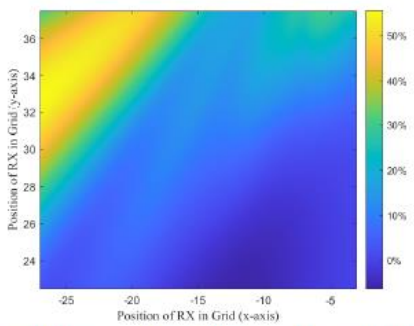

(c) Spatial rate gain at RX between the random configuration and the proposed secrecy spatial rate maximization scheme.

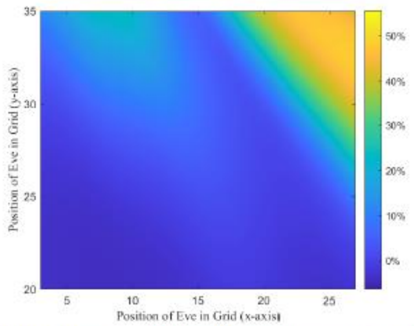

(d) Spatial rate gain at Eve between the random configuration and the proposed secrecy spatial rate maximization scheme.

Figure 2-44 Gain in percentage in the achievable spatial rates at the legitimate RX and Eve between the random BS/RIS BF and the proposed optimized schemes.

Conclusion

In this section, we investigated RIS-enabled MISO communication systems, where a passive RIS was deployed to extend the coverage of a legitimate link. By proposing a novel metric, that characterizes the spatial performance of the RIS in terms of secrecy over a targeted area, it was demonstrated that the proposed scheme can yield gains for an entire area, which can reach more than 50% close to sub-regions near the RIS. Compared to a scheme without RIS, the proposed scheme would provide an even larger gain, and therefore a gain **larger than x1.5. This gain is reported in the summary Table 2-1.**

2.5.6 E6: Robust Transmission Design for RIS-assisted Secure Multiuser Communication Systems in the Presence of Hardware Impairments (HIs)

This sub-section summarizes the work detailed in [PWP+23].

Introduction

Due to the absence of power amplifiers, digital signal processing units, and multiple radio frequency chains, the main features of a RIS include a low implementation cost, low power consumption, and easy deployment, as well as the capability of reconfiguring the wireless environment.

Traditional wireless security methods encrypt the data at the network layer. RISs can be utilized for enhancing the security of wireless networks and have been recently amalgamated with PLS as well.

Thanks to the capability of reconfiguring the propagation environment in a desired manner, an RIS can change the phase of each incident signal so as to enhance the desired signal power at the legitimate users, while suppressing the signal received by the eavesdroppers.

The existing contributions on RIS-assisted PLS assume that the transceivers are constructed with ideal and perfect hardware components. In practical communication systems, low-cost hardware is often preferred even though such hardware may be subject to HIs, such as I/Q imbalances, amplifier non-linearities, quantization errors, and phase noise. If these HIs are ignored at the design stage, the performance usually degrades.

In this paper, we investigate the security performance of RIS-assisted multiuser multiple-input single-output (MISO) systems in the presence of HIs. By deploying an RIS, we aim to improve security performance under the premise of ensuring fairness among the users. By optimizing the BS precoding matrix and the RIS reflection coefficients, it is formulated a fairness-based joint optimization problem that maximizes the weighted minimum approximate ergodic secrecy rate (WMAESR), subject to transmit power and unit modulus constraints.

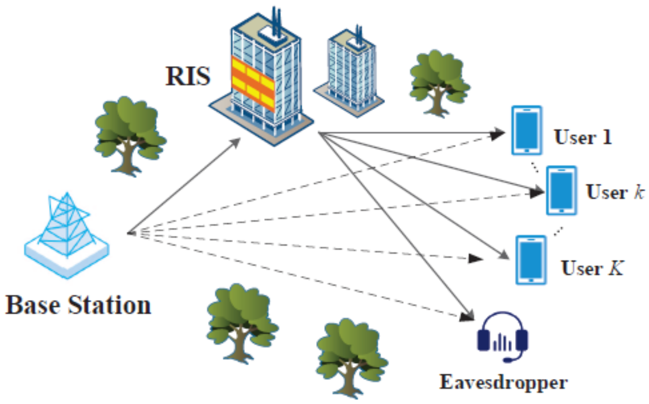

Figure 2-45 An RIS-assisted MISO downlink system with an N-antenna BS, a single-antenna eavesdropper and K single-antenna users.

System Model

We consider an RIS-assisted MISO downlink system with a BS, an eavesdropper, and K legitimate users, as illustrated in Figure 2-46. The BS is equipped with N > 1 transmit antennas to serve the legitimate users in the presence of the eavesdropper. In addition, an RIS consisting of M reflecting elements is deployed to ensure the secure transmission of data.

It is considered the worst-case assumption that the eavesdropper can eliminate most of the noise with the exception of the distortion noise due to the hardware at the transmitter. Also, it is assumed that the eavesdropper can decode and cancel the interference from other users. In addition, the eavesdropper is assumed to actively attack the communication system. Specifically, by pretending to be a legitimate user sending pilot signals to the BS during the channel estimation phase, the eavesdropper can mislead the BS to send signals to the eavesdropper.

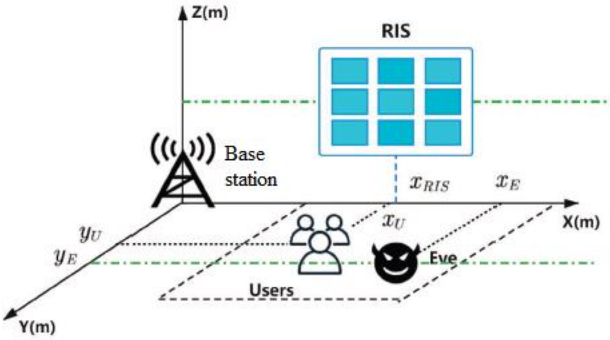

Figure 2-46 The simulated RIS-assisted MISO communication scenario.

Results

Figure 2-47 illustrates the impact of the maximum transmit power on the WMAESR. In this context, it is worth recalling that the distortion noise at the transceiver is assumed to be proportional to the signal power. Hence, increasing the signal power improves the SNR, but it increases the performance loss caused by the presence of HIs as well. It is observed that the security performance gap between the Non-Robust and the proposed algorithms gradually increases as the transmit power increases. This is because the Non-Robust algorithm does not account for the HIs by design, and its performance degradation is more prominent.

Name	Symbol	Value
The number of BS antennas	*M*	16
The number of RIS elements	*N*	4

Table 2-14 Simulation Parameters.

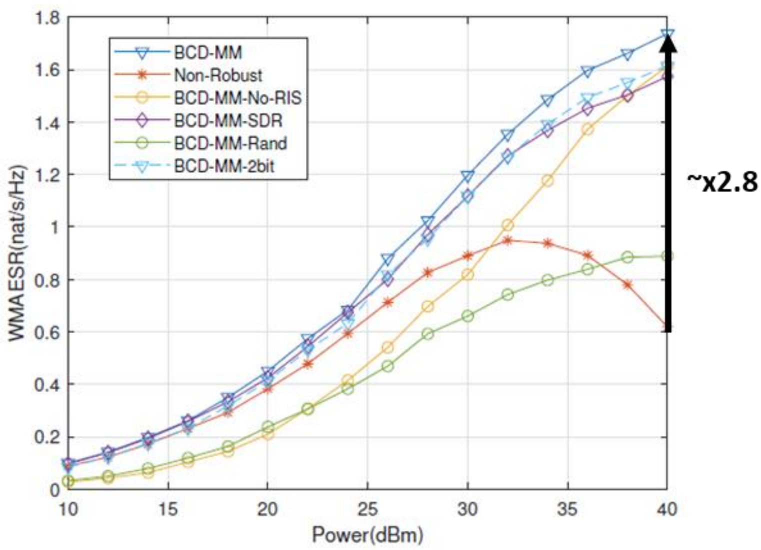

Figure 2-47 Achievable WMAESR versus the maximum transmit power.

Compared WMAESR (which is a RIS-aided scheme) of the proposed algorithm to that of the Non-Robust algorithm when the transmit power 40 dBm, we can obtain the performance gain of about x2.8. **Compared to a scheme without RIS**, the proposed algorithm who provide a gain in SSE larger than x2.8.

Conclusion

In this work, it is studied the AESR of an RIS-aided multi-user (MU) wireless network in the presence of hardware impairments. It is demonstrated that the deployment of an RIS can energy-effectively increase the AESR of legitimate users through appropriate adjustment of the RIS phase shifts and the precoding matrix of the BS. Simulation results demonstrated the advantages of the proposed robust transmission design that accounts for the hardware impairments. **Compared to a scheme without RIS, the proposed scheme provides an SSE gain larger than x2.8. This gain is reported in the summary Table 2-1.**

2.6 Category F: EE boosting

2.6.1 F1: EE maximization of MMIMO communications with dynamic metasurface antennas

This section summarizes the work detailed in papers [YXA+21-1][YXA+21-2].

Introduction

In this study, we investigate the optimization of the EE performance of Dynamic Metasurface Antennas (DMA)-assisted [SAI+21] MMIMO wireless communications on the UL direction. We consider the joint design of the transmit precoding of each multi-antenna user and the DMA tuning strategy at the BS to maximise the EE performance, considering the availability of either instantaneous or statistical CSI. Specifically, the proposed framework is shaped around Dinkelbach's transform, AO, and deterministic equivalent methods. In addition, we obtain a closed-form solution to the optimal transmit signal directions for the statistical CSI case, which simplifies the corresponding transmission design for the multiple-antenna case.

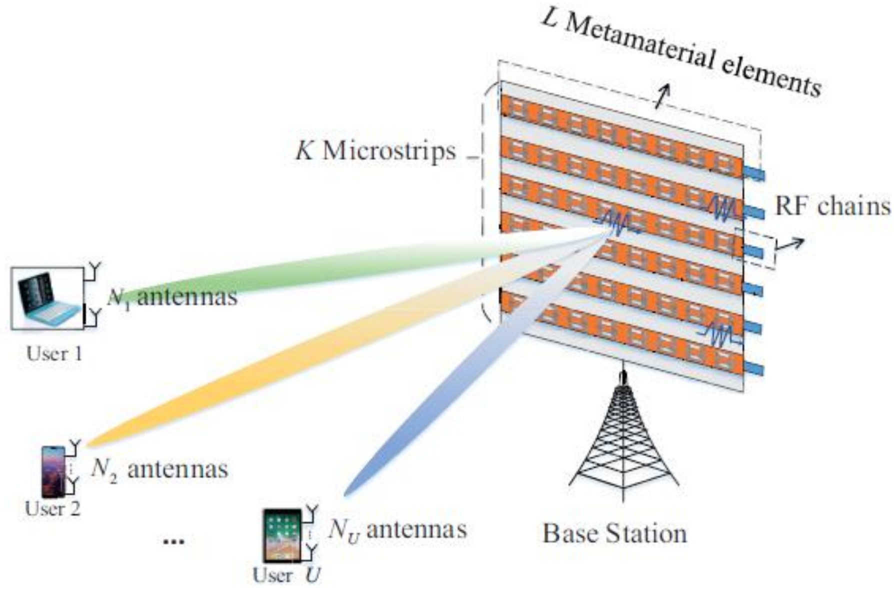

Figure 2-48 The considered DMA-assisted MMIMO UL system.

System Model

We consider a single-cell MMIMO UL system where the BS simultaneously receives signals from multiple users. In the following, we illustrate the input-output relationship of DMAs and the channel model. The considered system is composed of a DMA-based BS and U users. The BS is equipped with a planar array consisting of M metamaterial elements, and each user is equipped with N_u conventional antennas in a fully digital architecture. We assume that the DMA array consists of K microstrips, e.g., the guiding structure whose top layer is embedded with metamaterials, and each microstrip consists of L metamaterial elements, that is, $M = KL$. Each metamaterial element observes the radiations from the channels, adjusts, and transmits them along the microstrip to the corresponding RF chain independently. The output signal of each microstrip is the linear combination of all the radiations observed by the corresponding L metamaterial elements. The output signals of DMAs can be formulated as

$$\boldsymbol{z} = \boldsymbol{QHy} \tag{2.7.1}$$

where $\boldsymbol{y}$ denotes the DMA input signals, $\boldsymbol{H}$ is a diagonal matrix with entries the filter coefficients of the lth metamaterial in the kth microstrip, and $\boldsymbol{Q}$ is the configurable weight matrix of DMAS. In particular,

$$(\boldsymbol{Q})_{\{k_1,(k_2-1)L+l\}} = \begin{cases} q_{\{k_1,l\}}, k_1 = k_2 \\ 0, \ k_1 \neq k_2 \end{cases}, \tag{2.7.2}$$

where $q_{\{k_1,l\}}$ is the gain of the lth metamaterial in the k_1th microstrip. We also define $\boldsymbol{x}_u$ as the transmit signals from user u with zero mean and the transmit covariance matrix $E\{\boldsymbol{x}_u\boldsymbol{x}_u^H\} = \boldsymbol{P}_u$. Additionally, $\boldsymbol{x}_u$ satisfies $E\{\boldsymbol{x}_u\boldsymbol{x}_{u'}^H\} = \boldsymbol{0}, \forall\, u \neq u'$, which indicates that the signals from different users are independent of each other. Then, the channel output signal $\boldsymbol{y}$ is given by

$$\boldsymbol{y} = \sum_{u=1}^{U} \boldsymbol{G}_u\boldsymbol{x}_u + \boldsymbol{n}\,, \tag{2.7.3}$$

where $\boldsymbol{G}_u$ denotes the channel between user u and the BS, and $\boldsymbol{n}$ denotes the independently and identically distributed (i.i.d.) noise with covariance $\sigma^2 \boldsymbol{I}_M$, where σ^2 denotes the noise power.

Problem Formulation with Instantaneous CSI

The objective of this section is to design the transmit covariance matrices $\boldsymbol{P}_u$, and the DMA weight matrix $\boldsymbol{Q}$ to maximize the system EE performance, considering instantaneous CSI [VAT18], [VAT19]. To define the system EE, we start with the Spectral Efficiency (SE) definition of the DMA-assisted UL system. Assume that all metamaterial elements have the same frequency selectivity, then $\boldsymbol{H}$ can be expressed as the identity matrix multiplied by a constant. Therefore, the achievable system SE is given by

$$R = \log_2 \left| I_K + \frac{1}{\sigma^2} \sum_{u=1}^{U} \boldsymbol{Q}\, \boldsymbol{G}_u \boldsymbol{P}_u \boldsymbol{G}_u^H \boldsymbol{Q}^H (\boldsymbol{Q}\boldsymbol{Q}^H)^{-1} \right|. \quad \textbf{(2.7.4)}$$

The whole power consumption of the DMA-assisted system is given by

$$W = \sum_{u=1}^{U} (\xi_u tr(P_u) + W_{c,u}) + W_{BS} + K W_S, \quad \textbf{(2.7.5)}$$

where $\xi_u = \rho_u^{-1}$ with ρ_u denoting the transmit power amplifier efficiency of user u. In addition, $W_{c,u}$ denotes the static circuit power dissipation of user u and W_S represents the dynamic power dissipation of each RF chain chain, including, e.g., power consumption in the ADCs, amplifier, and mixer. W_{BS} incorporates the static circuit power dissipation at the BS. With the system SE in (2.7.4) and power consumption in (2.7.5), the EE of our considered DMA-assisted UL system is defined as

$$EE = B \frac{R}{W}, \quad \textbf{(2.7.6)}$$

where B is the channel bandwidth. So far, the EE maximization problem of the DMA-assisted UL system by designing the transmit covariance matrices $\boldsymbol{P}_u, \forall\, u$, and DMA weight matrix $\boldsymbol{Q}$ is formulated as follows:

$$\max_{\mathbf{Q},\mathbf{P}} \; EE \quad \textbf{(2.7.7)}$$

$$s.t. \quad (2.7.2),$$

$$tr(\boldsymbol{P}_u) \leq P_{max}\, , \boldsymbol{P}_u \succcurlyeq \mathbf{0},$$

where P_{max} denotes the maximum available transmit power.

To solve the optimization problem (2.7.7), we adopt an AO method to design $\boldsymbol{P}$ and $\boldsymbol{Q}$ in an alternating manner. For the optimization of $\boldsymbol{P}$, we adopt Dinkelbach's transform to convert the concave-linear fraction in the constraint (2.7.2) into a concave one. For the optimization of $\boldsymbol{Q}$, we first neglect the second set of constraints (related to $\boldsymbol{P}$) to obtain the corresponding unconstrained **Q**, and then adopt an alternating minimization algorithm to reconfigure **Q** to be constrained by (2.7.2).

Problem Formulation with Statistical CSI

Channels might be fast time-varying in practical wireless communications, thus frequently tuning DMAs and reallocating transmit power with instantaneous CSI might be difficult. In such cases, utilizing statistical CSI to optimize the system EE performance is more efficient. In this section, we explore approaches to optimize the system EE by designing the transmit covariance matrices and DMA weight matrix via exploiting statistical CSI.

To formulate the corresponding EE maximization problem, we firstly describe the system SE and power consumption metrics. For the statistical CSI case, we adopt the ergodic achievable SE metric defined as:

$$\bar{R} = E\left\{\log_2\left|I_K + \frac{1}{\sigma^2}\sum_{u=1}^{U}\boldsymbol{Q}\,\boldsymbol{G}_u\boldsymbol{P}_u\boldsymbol{G}_u^H\boldsymbol{Q}^H(\boldsymbol{Q}\boldsymbol{Q}^H)^{-1}\right|\right\}, \quad \textbf{(2.7.8)}$$

where the expectation is taken over the channel realizations. In addition, we use (2.7.5) to model the overall power consumption. Then, the corresponding EE maximization problem can be formulated in a similar manner with the instantaneous CSI problem (2.7.7), using (2.7.8). However, it is challenging to tackle because the objective exhibits a concave-linear fractional structure. In addition, the expectation operation further increases the computational overhead. Nevertheless, this optimization problem can be solved by first deriving an optimal closed-form solution to the transmit signal directions of users. Then, we apply the deterministic equivalent method to asymptotically approximate the ergodic SE, aiming to reduce the computational overhead. Next, we adopt Dinkelbach's transform to obtain the users' power allocation matrices. Finally, we derive the weight matrix of DMAs with a similar method to the instantaneous CSI case.

Results

In our numerical analysis, we set the number of users as $U = 6$ and each user is equipped with 4 antennas, i.e., $N_u = 4, \forall u \in U$. The antennas of users are placed in uniform linear arrays spaced with half wavelength. We set the number of microstrips as $K = 8$ and each microstrip is embedded with $L = 8$ metamaterial elements. The space between metamaterial elements on the DMA array is set as 0.2 wavelength. We set the bandwidth as $B = 10\,MHz$, the amplifier inefficiency factor as $\rho = 0.3$, $\forall u$, and the noise variance as $\sigma^2 = -96\,dBm$. For the power consumption, we set the static circuit power as $W_{c,u} = 20\,dBm$, $\forall u$, the hardware dissipated power at the BS as $W_{BS} = 40\,dBm$, and the static power per microstrip as $W_S = 30\,dBm$. Additionally, the entries of the DMA weight matrix Q are selected from the following four sets [SDE+19]:

- UC: the complex plane, i.e., $Q = C$;
- AO: amplitude only, i.e., $Q = [0.001, 5]$;
- BA: binary amplitude, i.e., $Q = \{0, 0.1\}$;
- LP: Lorentzian-constrained phase, i.e., $Q = \left\{\frac{j+e^{j\phi}}{2} : \phi \in [0, 2\pi]\right\}$.

In Figure 2-49, the DMA weights are chosen from the complex-plane set. We compare the EE performance of the DMA-assisted UL system versus the power budget Pmax between the instantaneous and statistical CSI cases. As expected, the EE performance is better when the instantaneous CSI can be perfectly known in both the EE- and SE-oriented approaches. We also observe that the EE performance based on statistical CSI is quite close to that based on instantaneous CSI. Note that, the optimization process in the statistical CSI case is more computationally efficient than the instantaneous CSI one. Thus, in our DMA-assisted communication scenario, the statistical CSI is a good substitute for the instantaneous CSI to maximize the system EE.

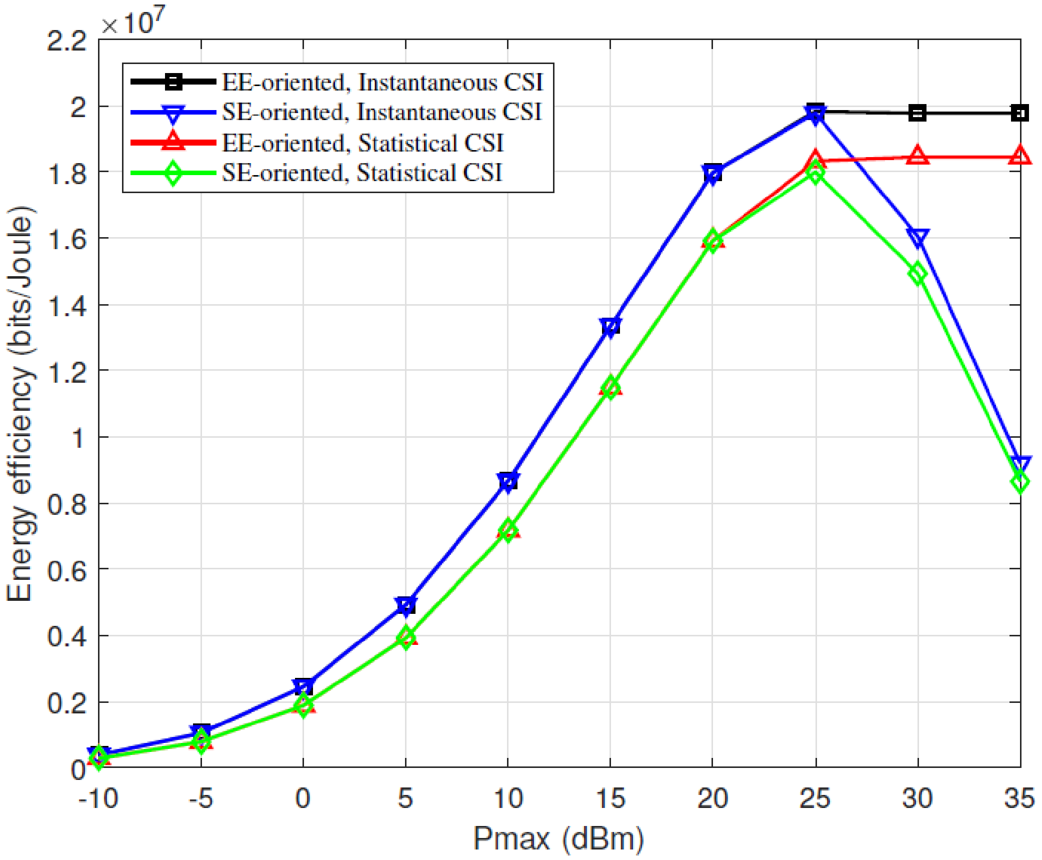

Figure 2-49 EE performance comparison between the instantaneous and statistical CSI cases versus the transmit power budget in both the SE- and EE-oriented approaches.

Conclusion

We studied the EE performance optimization of the DMA-assisted MMIMO UL communications, considering both the cases of exploiting the instantaneous as well as statistical CSI. Specifically, we developed a well-structured and low-complexity framework for the transmit covariance design of each user and the DMA configuration strategy at the BS, including the AO and deterministic equivalent methods, as well as Dinkelbach's transform. Based on our algorithm, the DMA-assisted communications achieved much higher EE performance gains compared to the conventional large-scale antenna array-assisted ones, especially in the high power budget region. **The proposed scheme improves the EE by 75% (x1.75) with respect to conventional fully digital and fully-connected hybrid A/D architectures at the BS. This gain is reported in the summary Table 2-1**.

2.6.2 F2: EE Maximization in RIS-aided Networks With Global Reflection Constraints

This sub-section summarizes the work detailed in [FZR+23].

Introduction

Besides providing a large number of degrees of freedom for signal transmission, RISs are particularly attractive from an energy-efficient point of view for their nearly passive behavior. EE was already considered a key performance indicator of 5G networks, and remains a major aspect of 6G networks, too. Indeed, recent studies argue that 5G has not achieved the promised 2000x EE increased, actually increasing the EE only by a factor four.

Only few contributions have started addressing the issue of radio resource allocation for EE maximization in RIS-based networks. In this work, it is analyzed the issue of EE maximization in an RIS-aided MU wireless network, by novel optimization methods. Unlike existing works, the optimization is performed assuming that the RIS is capable of global reflection, i.e. the constraint on the power reflected by the RIS is not applied to each reflecting element individually, but rather to the complete surface. Finally, EE optimization is tackled not only with respect to the transmit powers and RIS reflection coefficients, as it is customary in the literature, but also with respect to the linear receive filters.

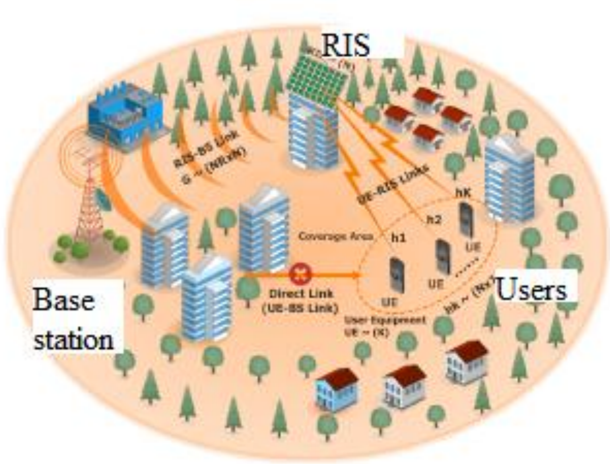

Figure 2-50 Considered wireless network.

System Model

It is considered the UL of a MU system in which K single-antenna mobile terminals communicate with a BS equipped with N_R antennas, through an RIS with N reflecting elements (Figure 2-50).

This work considers the more general scenario in which the RIS is characterized by a global reflection constraints, i.e. a constraint on the total power reflected by all of the RIS elements. In this case, the total power reflected by the RIS is equal to the total incident power. However, the global reflection constraint is more general, as it allows for the modulus of some reflection coefficients to be larger than one, while ensuring that the RIS is still nearly-passive from the global point of view, i.e. the total reflected power is not larger than the total incident power.

Results

Figure 2-51 shows the global EE achieved by: maximizing the global EE by the two proposed methods in this work; the resource allocation obtained by adapting the two proposed methods in this work for rate maximization; and uniform power allocation and random RIS phase shifts. As anticipated, the method from Section 4 in [FZR+23] significantly outperforms the approach from Section 3 in [FZR+23], thanks to the exploitation of the mathematical structure of the optimal receive filter, rather than simply updating the receive filter within the alternating maximization algorithm. Moreover, a large gain is obtained compared to Case, in which radio resources are not optimized.

Name	Symbol	Value
The number of mobile terminals	K	4
The number of RIS elements	N	100
The number of BS antennas	N_R	4
Bandwidth	B	20 MHz
Hardware power consumed by the BS/mobile terminal	P_0	40 dBm
Hardware power consumed by the RIS	$P_{0,RIS}$	20 dBm
Static power consumed by each RIS element	$P_{c,n}$	0 dBm
Noise power spectral density	N_0	-174 dBM/Hz
Path-loss exponent	η	4

Table 2-15 Simulation Parameters.

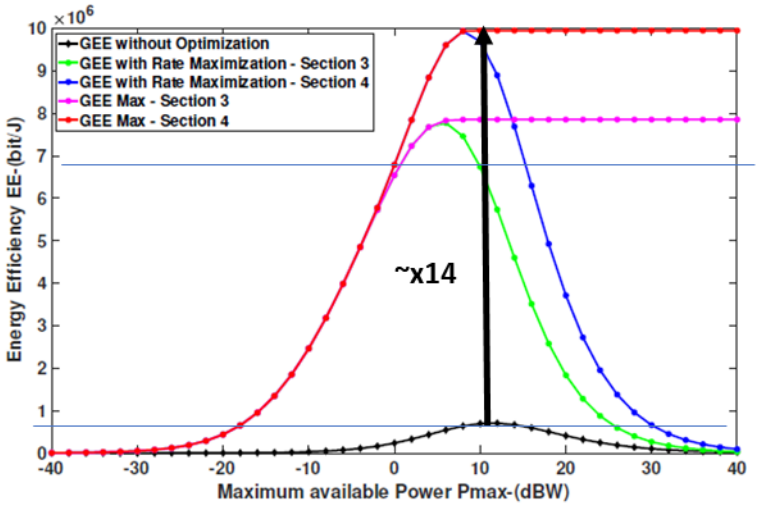

Figure 2-51 EE versus Maximum available Power Pmax.

Compared to the peak value of EE gains of the proposed algorithm to that of without optimization, we have the performance gain of about x14. **Compared to a system without RIS, the proposed scheme would therefore reach an even larger gain than x14.**

Conclusion

This work addressed the EE maximization problem in a multiuser network aided by an RIS endowed with global reflection capabilities. The results indicate that the proposed radio resource optimization algorithms provide large EE gains compared to heuristic random resource allocations. Compared to the peak value of EE gains of the proposed algorithm to that of without optimization, we have the performance gain of about x14. **Compared to a system without RIS, the proposed scheme would therefore reach an even larger gain than x14. This gain is reported in the summary Table 2-1.** Moreover, a careful optimization of the receive filters and exploitation of the RIS global reflection capabilities can provide significant performance improvements.

2.6.3 F3: ARES: Autonomous RIS solution with Energy Harvesting and Self-configuration towards 6G

This sub-section summarizes the work detailed in [ADS+23] on a novel RIS device that is energy-autonomous. Note that aspects relative to protocol, algorithms, and spectral efficiency, related to this contribution are explained in [D4.4], whereas current section focuses on the analysis of the energy-autonomy.

Introduction

The RIS paradigm transforms the propagation environment from an adversary to an optimizable communication ally actively contributing to improving performance, with the sole use of surfaces equipped with low-cost, and low-complexity electronics. However, being quasi-passive devices, channel estimation requires complex procedures performed on the entire transmitter-RIS-receiver path, which can hamper their agile deployment. To counter this drawback, the concept of hybrid RIS (HRIS) has been proposed, bringing built-in sensing capabilities to quasi-passive RISs. This kick-started the development of self-configuring RISs as the epitome of a plug-and-play (P&P) RISs integration solution into existing network deployments that eliminates the need for the control channel and operator management, paving the way to the massive and flexible deployment of RISs known as Internet-of-Surfaces (IoS).

As operational RISs may run on compact batteries, but calling for periodic maintenance. Alternatively, energy harvesting (EH) techniques may be implemented at the RISs to provide them with potentially unlimited energy availability, avoiding the need for servicing for long time periods and leading to a fully autonomous solution in terms of configuration, energy, and maintenance.

In this work, metasurface solution targeting the need for a power supply to devise a fully-autonomous, self-configuring, and energy self-sufficient, namely Autonomous RIS with Energy harvesting and Self-configuration (ARES), is proposed. ARES takes advantage of the key assets, namely the new channel estimation model lato-sensu at the HRIS and the autonomous HRIS configuration methodology based only on the CSI available at the HRIS, and establishes the following main contributions: i) the design of a fully integrated radio frequency EH technology to empower off-the-grid operations, ii) an accurate model of the battery charging and discharging processes based on an irreducible Markov chain, iii) a battery dimensioning strategy that guarantees the availability of the HRIS for the desired time period. ARES is shown to provide near-optimal performance when compared to the full-CSI-aware and power-grid-enabled approaches while facilitating energy self-sufficient IoS deployments.

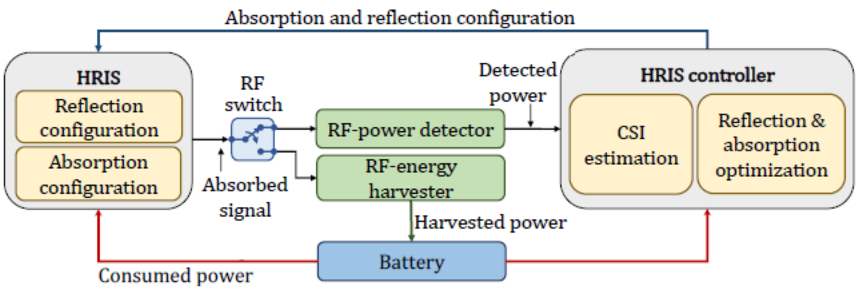

Figure 2-52 Overview of ARES's architecture and functional blocks.

System Model

It is considered a scenario in which a BS equipped with M antennas serves K single-antenna user equipments (UEs) with the aid of an HRIS. The BS has a uniform linear array, and the HRIS has a planar linear array equipped with N meta-atoms. It is assumed that the inter-distance of the BS and HRIS array elements is the half of the carrier wavelength. The joint reflection and absorption capabilities of the HRIS are realized through directional couplers whose operation is determined by the fraction of the received power that is reflected for communication. Here, the amount of absorbed power is measured at the power detector or harvested at the energy harvester.

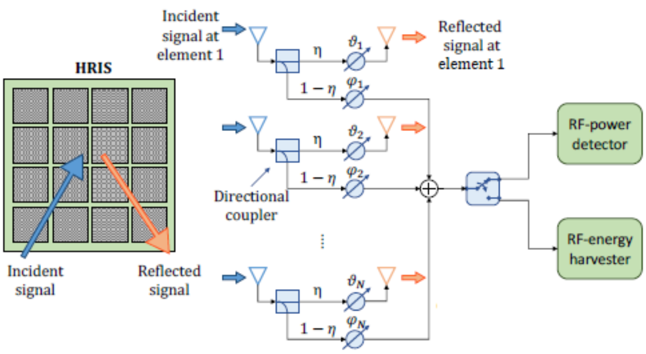

Figure 2-53 System model diagram of a hybrid RIS.

Results

The performances of ARES in terms of energy self-sufficiency, starting from the evaluation of the harvested and consumed power, and considering a low state-of-charge (SoC) threshold of 10% is assessed in Figure 2-54. This figure shows the average harvested (left) and consumed (right) power with different HRIS hardware configurations, and in different traffic conditions. The average harvested power has a monotonic increasing behavior concerning the number of meta-atoms composing the surfaces, as the larger the number of elements, the higher the HRIS ability to focus towards the signal sources, which, in turn, grows the harvested power. Compared the harvested power for HRIS elements is 5 to that for HRIS elements is 60, we can obtain the performance gain of about 10 dB when traffic is 0.8. Similarly, more quantization levels Q allow for finer granularity in the phase shift selection, further improving the harvesting performance. However, higher values of N and Q increase the complexity of the HRIS hardware, inflating the corresponding overall power consumption. As a result, a novel trade-off arises between the harvested and the consumed powers, whose deviation needs to be compensated by the battery in order to keep the HRIS alive with the desired the probability of loss of charge.

Name	Symbol	Value
Frame duration	T	10 ms
RIS elements	N	100
Low state-of-charge threshold	Γ	10 %
The number of user	K	75
The network area	A	50m X 50m

Table 2-16 Simulation Parameters.

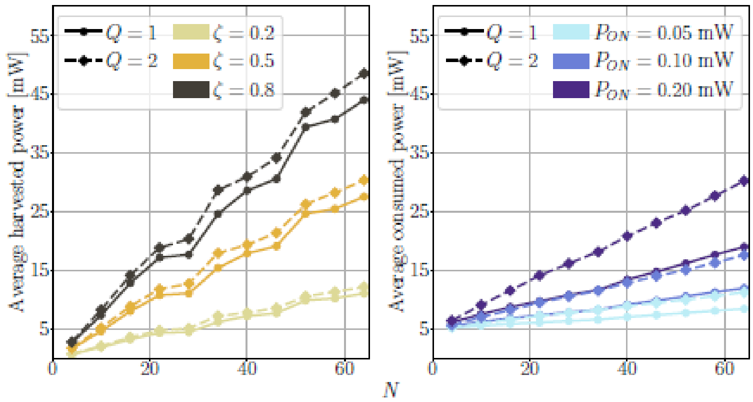

Figure 2-54 ARES average harvested and consumed power against the number of HRIS elements N for different values of traffic, PIN diode activation consumption PON, and phase quantization Q.

Conclusion

In this work, it is introduced ARES solution towards 6G, which dismisses the need for a complex ad-hoc control channel and a power supply to operate RISs, bringing up a fully-autonomous RISs solution with no deployment constraint. ARES is built upon i) a new low-complexity hardware design providing HRISs with both sensing and energy harvesting capabilities, ii) a channel estimation model lato-sensu at the HRISs, iii) an autonomous HRISs configuration methodology operating both on the reflection and on the EH properties of the HRISs, which is based only on locally estimated CSI, without a control channel. ARES achieves communication performance comparable with fully CSI-aware benchmark while demonstrating the feasibility of EH for RISs power supply in future deployments.

Therefore, compared to a device that requires an external power source or a battery that must be charged or substituted manually (i. e. requires **non-zero energy**), the present novel device removes these requirements (i.e. requires **zero energy**). Hence, in terms of external energy requirement, the gain is **infinite (non-zero divided by zero external energy requirement)**. In this case, the RIS is an **enabler** of energy-autonomous RIS. **This advantage is reported in the summary Table 2-1.**

3 Novel assessment methods of EE, EMFEU and SSE Improvements

This section summarizes the work performed within Task 6.3. For each of the various new models to assess EE, SSE or EMFEU that were proposed by WP6, Task 6.3, the following brief description is provided:

- Introduction.
- System model or measurement method.
- Results.
- Conclusion.

Note that for more mature models, the detailed description of the proposed models and their performance is available in submitted/accepted papers. For other schemes, at an earlier stage of study, only initial views on expected performance are provided.

3.1 Battery recharging time models for RISs-assisted wireless power transfer systems

This section summarizes a study that is detailed in [MMA+22].

3.1.1 Introduction

Wireless power transfer (WPT) has been highly recognized in both academia and industry as a promising technology to address the energy sustainability problem of wireless nodes and has rapidly gained a growing interest in the research of B5G communication networks. The studies reported in [WZ20] [P+20][WZ19] assume battery free RF energy harvesting (RFEH) energy receivers (ERs), whose harvested energy is directly used for future transmissions. In this case, the amount of the received RF signals, and consequently, the amount of harvested energy, is considered to be sufficient and predictable over a certain period of time. However, in scenarios where RFEH nodes are equipped with batteries [AK14], the harvested energy is stored first in the battery before being used for future transmissions. Since the power of the received RF signal depends on the distribution of the probabilistic wireless fading channel between the transmitter and the receiver, the RFEH process and similarly, the time required to recharge the battery of an RFEH node, called the battery recharging time (BRT), become stochastic processes. To the best of our knowledge, the statistical characterization of BRT is not yet studied in the open literature. Motivated by this, the main focus of this work is to develop a novel theoretical framework to characterize the statistical properties of BRT for RIS-assisted WPT systems, consisting of ERs with limited battery capacity.

3.1.2 System Model

In this paper, we consider a single-antenna RF source node, S, and a single-antenna energy-constrained ER, as depicted in Figure 3-1. The ER could be a low-power sensor node equipped with a battery with a finite capacity. In order to extend the operational range of the ER, while ensuring that its harvested energy is sufficient for real-life operation, we propose WPT assisted by an RIS. The end-to-end (E2E) channel gain between S and ER characterizes the power received at the ER, and accordingly, defines the behavior of the overall RFEH process, including the instantaneous BRT at ER.

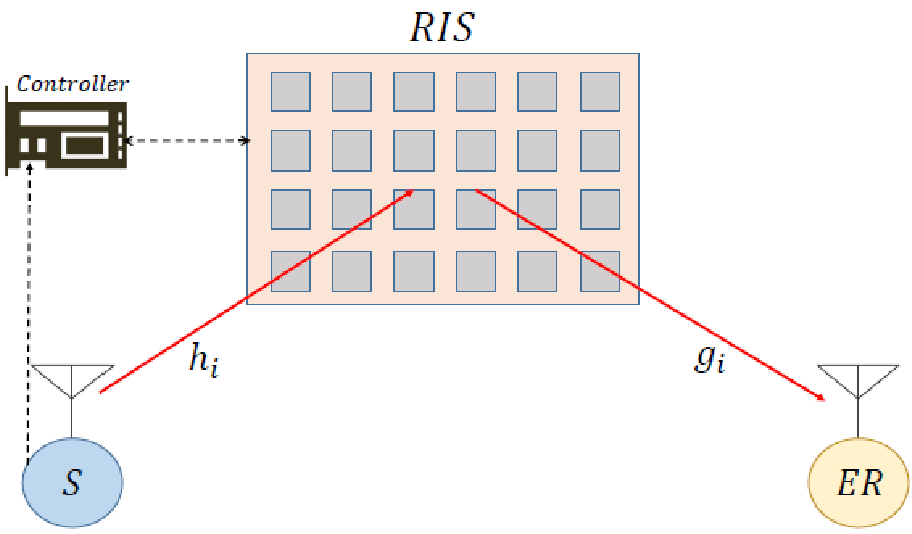

Figure 3-1 RIS-assisted WPT system model.

We further assume that a direct link does not exist between S and ER, WPT can be achieved only via the RIS. In our setup, we consider an RIS of N reflecting elements (REs). Each of the elements can be reconfigured by a communication-oriented software through a controller. The power transmitted from S, being either a BS or an RF source, which is reflected by the RIS towards the ER, is harvested and stored in a battery with a limited capacity before being used in future signal transmissions. h_i and g_i denote the small scale complex channel fading coefficients of the $S \rightarrow$ RIS and RIS $\rightarrow$ ER links, respectively, where $|h_i|$, $|g_i| \sim \mathcal{CN}(0,2\sigma^2)$ for $i \in \{1, \dots, N\}$.

Let P_s denote the transmit wireless power of the source node. The instantaneous total power received at ER through the RIS is expressed as

$$P_r = \frac{P_s}{d_1^\delta d_2^\delta} B^2 \quad \textbf{(3.1.1)}$$

where $B = \sum_{i=1}^{N} |h_i||g_i|$ is the E2E channel gain, d_1 and d_2 represent the distance between S and the center of the RIS and between the center of the RIS and ER, δ is the path loss exponent.

As previously mentioned, the BRT, T_r, is determined by the amount of power received and then harvested at ER

$$T_r = \frac{\alpha}{P_r} \quad \textbf{(3.1.2)}$$

where α is the conversion coefficient, which is a function of the battery and the RFEH circuit parameters.

For RIS-assisted WPT systems, the PDF of the battery recharging time at ER node is given as

$$f_{T_r}(\tau) \approx \frac{a_1 a_2}{2\tau} G_{1,2}^{2,0}\left[\frac{1}{a_2}\sqrt{\frac{\alpha}{\bar{P}_r \tau}}\,\middle|\,\begin{matrix} -;a_3+1 \\ a_5+1, a_4+1;- \end{matrix}\right], \quad \tau > 0 \quad \textbf{(3.1.3)}$$

We obtain the CDF of the BRT in a closed-form as

$$F_{T_r}(\tau_{th}) = 1 - a_1 a_2 G_{2,3}^{2,1}\left[\frac{1}{a_2}\sqrt{\frac{\alpha}{\overline{P_r}\tau_{th}}}\middle|_{a_4+1,a_5+1;0}^{1;a_3+1}\right], \quad \tau_{th} > 0 \tag{3.1.4}$$

$$a_1 = \frac{\Gamma(a_3+1)}{a_2\Gamma(a_4+1)\Gamma(a_5+1)}$$

$$a_3 = \frac{4\varphi_4 - 9\varphi_3 + 6\varphi_2 - \mu_1}{-\varphi_4 + 3\varphi_3 - 3\varphi_2 + \mu_1}$$

$$a_2 = \frac{a_3}{2}(\varphi_4 - 2\varphi_3 + \varphi_2) + 2\varphi_4 - 3\varphi_3 + \varphi_2$$

$$a_4 = \frac{a_6 + a_7}{2}$$

$$a_5 = \frac{a_6 - a_7}{2}$$

$$a_6 = \frac{a_3(\varphi_2 - \mu_1) + 2\varphi_2 - \mu_1}{a_2} - 3$$

$$a_7 = \sqrt{\left(\frac{a_3(\varphi_2 - \mu_1) + 2\varphi_2 - \mu_1}{a_2} - 1\right)^2 - 4\,\frac{\mu_1(a_3+1)}{a_2}}$$

$$\varphi_i = \frac{\mu_j}{\mu_{j-1}}, j > 1$$

$$\overline{P_r} = \frac{P_r}{d_1^{\delta} d_2^{\delta}}$$

Where $G_{:,:}^{:,:}[.|.]$ denotes the Meijer G-function, μ_j is the j-th moment of B and Γ is the gamma function.

The n-th order moment of the BRT, denoted by $\mu_{T_r}(n)$, is a very useful statistical tool, as it enables the characterization of the mean value of the BRT, in addition to other underlying useful properties such as its skewness and kurtosis.

$$\mu_{T_r}(n) = a_1 a_2^{(1-2n)}\left(\frac{\alpha}{\overline{P_r}}\right)^n \frac{\Gamma(a_4+1-2n)\,\Gamma(a_5+1-2n)}{\Gamma(a_3+1-2n)} \tag{3.1.5}$$

The mean value of the BRT when $N > 1$ converges to

$$\overline{T_r} = E[\tau_r] = \frac{4\alpha}{(N^2\pi^2 + N(16-\pi^2))\overline{P_r}} \tag{3.1.6}$$

3.1.3 Results

In this section, numerical and Monte Carlo simulation results are presented to validate the accuracy of the proposed theoretical framework. This section also focuses on characterizing the properties of the BRT in RIS-assisted WPT wireless systems. The term Monte Carlo simulations refers to the use of actual fading channel variates with a number of repetitions of 10^6 trials. Unless otherwise stated, the RFEH efficiency factor $\eta = 0.5$, as a worst case scenario, capturing the effects of low-cost hardware, and the total distance, d_{tot}, between the source node, S, and the ER node is set to $5\,m$. In order to ensure far-field WPT, we assume that the size of RIS is relatively smaller than the transmission distance. It is assumed that the RIS is located mid-way between S and ER, i.e., $d_1 = d_2 = d_{tot}/2$, and the path-loss exponent, $\delta = 2.7$. Also, it is recalled that P_s defines the total transmit power of the system.

To gain more insights about the effect of varying the transmit power on the statistical distribution of the BRT in RIS-assisted WPT systems, we provide in Figure 3-2 the CDF of the BRT threshold, T_r, of the RIS-assisted system. The examination is carried out for different N values and assuming two transmit power scenarios, namely low- ($P_s = 7\ dBm$) and high- ($P_s = 30\ dBm$) transmit power. The excellent fit between the simulation and the analytical results verifies the accuracy of our developed theoretical framework. As expected, for a fixed N, as the T_r increases, the CDF value increases. Additionally, for a given T_r value, as N increases, the CDF value improves. This indicates that the efficiency of the RFEH process is remarkably improved in an RIS-assisted WPT system by increasing the number of REs, N.

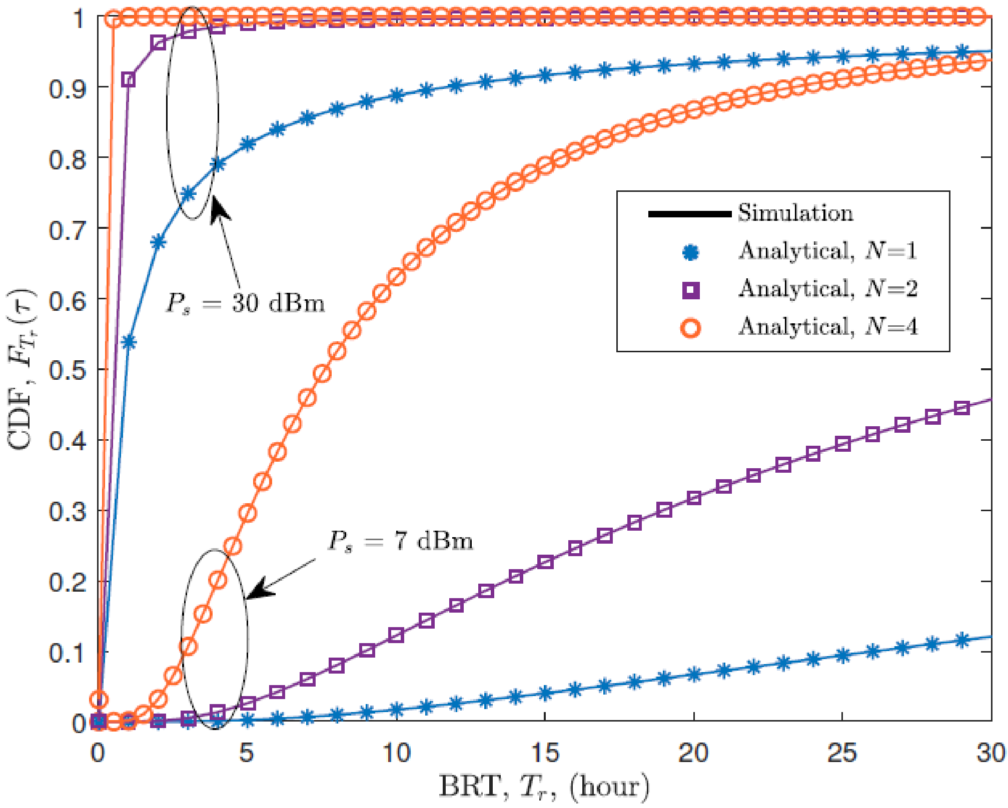

Figure 3-2 The CDF as a function of BRT threshold for RIS-assisted for low- and high- transmit power scenarios and for different values of N.

3.1.4 Conclusion

In this work, we developed a theoretical framework to investigate the energy sustainability of RIS-assisted WPT systems, from the BRT perspective of an RFEH node. We derived novel low complexity tight closed-form approximations for the PDF, CDF, and moments of the BRT as functions of the received power, battery parameters, and number of RIS REs. Besides being accurate and mathematically tractable, our results reveal that the proposed statistical tools provide an efficient means to evaluate RIS-assisted WPT systems and extract useful design insights. For example, our results show that doubling the number of RIS elements improves the predictability of the BRT of the RFEH nodes in the network and offers a 4-fold reduction in its mean value. Moreover, it is reported that the characteristics of the BRT are significantly impacted not only by the system parameters, such as the distance between the nodes, but also by the battery parameters of the RFEH node, such as the battery capacity. Finally, our results illustrated that significant performance gains in the BRT have been observed by locating the RIS close to the source or to the RFEH node.

3.2 Joint Metrics for EMF Exposure and Coverage in Real-World Homogeneous and Inhomogeneous Cellular Networks

This sub-section summarizes the work detailed in [GWW+23].

3.2.1 Introduction

Telecommunication operators are faced with the challenge of optimizing the coverage of their cellular networks while ensuring compliance with public EMF exposure limits. On the one hand, the signal-to-interference-and-noise ratio (SINR) enables the study of coverage, outage, data rate, interference level or spectral efficiency. On the other hand, the EMFE is subject to restrictions specified in terms of incident power density (IPD), or, equivalently, in terms of electric field strength. However, both quantities are still most often considered independently while their combination is necessary to fully address network optimization problems. Both metrics also strongly depend on the randomness in the network topology. To capture this aspect, stochastic geometry (SG) theory can be efficiently employed as an alternative to numerical simulations. Using this framework, BSs are modeled as spatial point processes (PP), for which closed-form expressions characterizing the average network performance can be derived.

Motivated by these considerations, the main aims are (i) to introduce an analytical framework for jointly evaluating the trade-offs between coverage and EMF exposure for two different PPs (motion-invariant and motion-variant) and (ii) to validate the proposed approach based on realistic datasets tailored to the large majority of urban and rural environments.

3.2.2 System Model

The proposed analytical approach is based on a β-Ginibre point process (β-GPP) for both urban and rural motion-invariant environments. This is motivated by the fact that the β-GPP allows for accurate and tractable modeling of many motion-invariant networks, in Western Europe. Previous analyses for β-GPP cellular networks are limited to the SINR CDF assuming Rayleigh fading channel for networks of finite size. Therefore, motion-invariant networks by introducing an inhomogeneous Poisson point process (I-PPP) model for motion-variant networks with a radial intensity measure is applied.

The β-GPP is characterized by its constant BS density λ and the β-parameter.

The I-PPP is characterized: Large European cities are often characterized by the presence of a densely populated historic center, with old buildings and an irregular street organization, leading to a high density of BSs to accommodate the large data traffic. As the distance to the center increases, the density of antennas decreases, leading to an almost radial density.

The propagation model is defined: the received power is a multiplication of the effective isotropic radiated power (EIRP) of the BS, the channel fading, and the path loss attenuation.

3.2.3 Results

The marginal distribution of the EMF exposure for several values of β is shown in Figure 3-3. Recalling that the limiting case $\beta = 0$ corresponds to a Homogeneous Poisson Point Process (H-PPP) and $\beta = 1$ corresponds to a GPP with more regularity, the EMF exposure is lower when the distributions of points is more random while the coverage is improved in networks that are more regularly deployed. This can be explained from three observations. First, in a more regular network, the typical user is on average closer to the serving BS but also to the most interfering BSs. Second, the *n*-th nearest BS gets closer on average as n is smaller. Third, the signal power decreases in $r^{-\alpha}$, where *r* is the distance between the user and the BS. As a consequence, the more regular the network, the greater the power of the useful signal and the greater this latter in comparison with the power of the interfering signals. To maximize both the coverage and the EMF exposure, the joint CDF of the EMF exposure and SINR can be analyzed. As can be seen in Figure 3-4, for some pairs of thresholds (*T*, *T'*), the higher, the better the performance of the network in terms of EMF exposure and coverage, but for other pairs, an opposite trend is obtained.

Name	Symbol	Value
Frequency	f	2.1 GHz
BS density	λ	6.17 BS/km²
Exponent of path loss	α	3.2
β-parameter	β	0.75
Radius of a cell	τ	3 km
Transmission power	P_t	66 dBm
Height of BS	z	33 m
Exclusion radius	r_e	0 m
Thermal noise power	σ^2	-94 dBm

Table 3-1 Simulation Parameters.

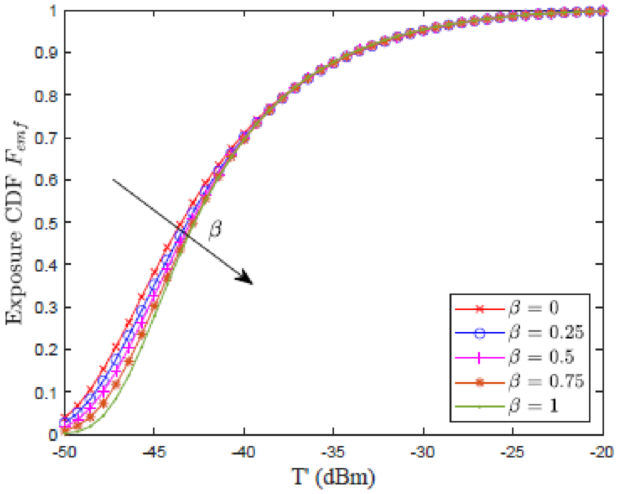

Figure 3-3 CDF of the EMF exposure for different values of β in a β-GPP network.

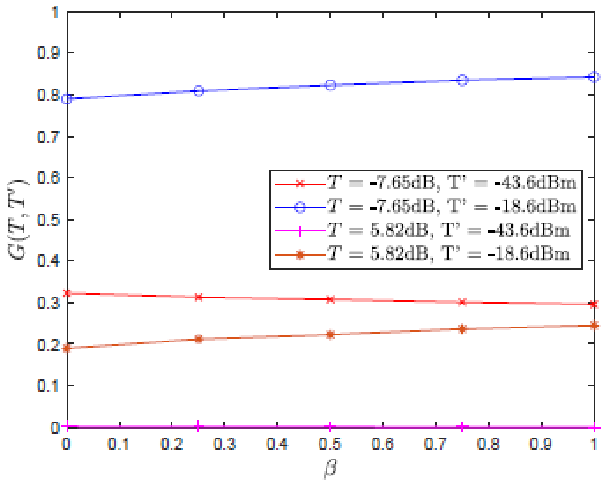

Figure 3-4 Joint CDF of the EMF exposure and SINR for several pairs (T,T') for different values of β in a β-GPP network.

3.2.4 Conclusion

Performance metrics are provided to simultaneously analyze the EMF exposure and the coverage in motion-invariant and motion-variant cellular networks. Based on network topologies usually encountered in European cities, the β-Ginibre point process is used as an example of tractable Point Process (PP) for motion-invariant networks. In motion-variant networks, the network is modeled by an I-PPP. An analysis of the network parameters is also provided and shows that an optimal value of these parameters can be found to maximize the coverage while minimizing the EMF exposure. Based on this study, studies to increase EE considering EMF exposure and SINR can be motivated.

3.3 Development of modelling tools by FDTD methods, and integration with framework provided by WP3

This section presents the numerical activity to model and simulate the RIS within our FDTD code.

3.3.1 Introduction

We begin to model the RIS within our 3D FDTD code. Basically, the RIS consists of a metasurface with a very thin thickness with respect to the wavelength at the operating frequency. Figure 3-5 a), b) represent a general RIS behaviour where an incident wave on the RIS surface can be transformed into a reflected and/or transmitted wave. We include the RIS in our numerical code by adopting the Generalized Sheet Transition Conditions (GSTCs). The GSTCs use an appropriate set of boundary conditions that allow to manage the **E** and **H** field discontinuities introduced by the metasurface within the FDTD scheme. This method allows us to simulate the RIS by a homogeneous sheet, see Fig. 3-3 a), by using the tensorial susceptibility function $\bar{\bar{\chi}}(x,y)$ [HKG+21][VCA+18][D6.2]. While we implemented this boundary conditions we encountered a stability issue in the FDTD simulation, investigation is still ongoing. To continue our activity, we modelled the RIS as a periodic structure made by Perfect Electric Conductor (PEC) square patches [FCB21][CBM23-1][CBM23-2].

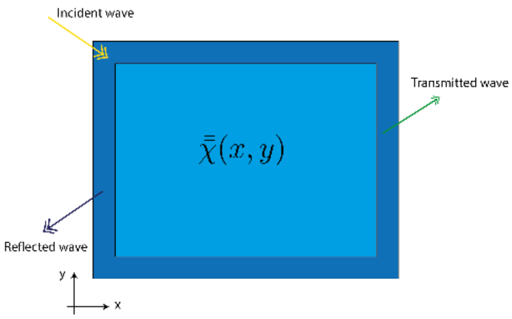

a) With GSTCs

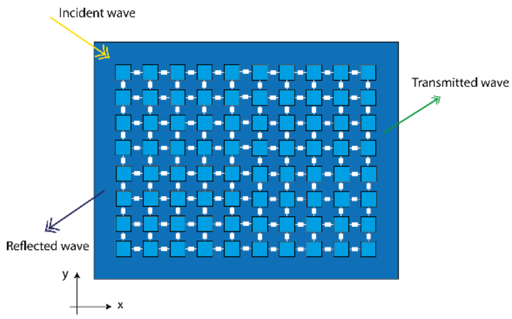

b) With PEC patches and varactors.

Figure 3-5 RIS Model

3.3.2 System Model

Focusing on the second case, the RIS is modelled by periodic PEC squares patches over a ground plane. Each metallic patch is interconnected with the others through a capacitor [FCB21]. The excitation is provided by a set of one or more plane waves [DAH98, MAP06]. More details concerning the set-up and the generation of plane wave(s) are reported in [D3.4]. The simulated RIS consists of 100 PEC patches and 180 varactor diodes with a capacitance of 1.0 pF and 0.1 pF, to emulate a short and an open circuit respectively.

3.3.3 Results

Figure 3-6 a) and b) report the distribution of the magnitude of the electric field on the RIS at

3.75 GHz, which corresponds to one of the 5G licensed operating frequency.

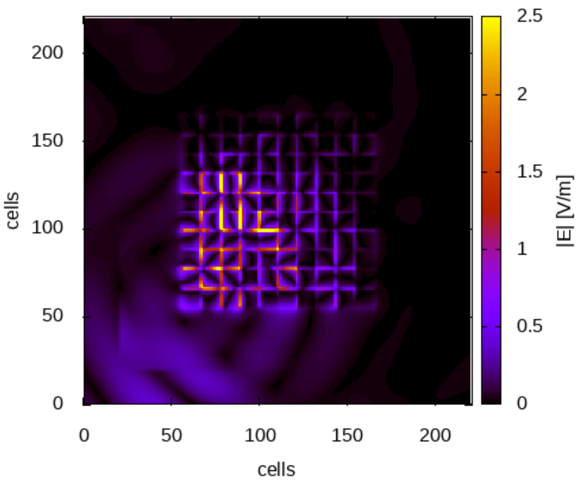

a) With C=1.0 pF.

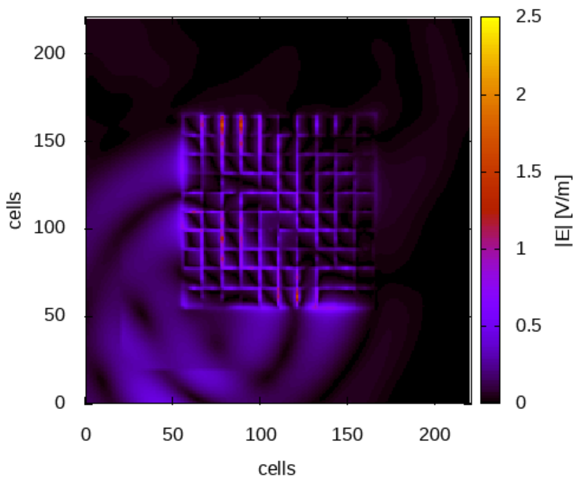

b) With C=0.1 pF.

Figure 3-6 Distribution of the magnitude of the electric filed on the RIS.

Beside to the two borderline cases such as RIS “OFF” state and “ON” state, i.e. all capacitors set to 0.1 pF and 1.0 pF respectively, we optimized the RIS configuration at 3.75 GHz.

In our case, with 180 varactors we have 2^180 configurations to test which constitutes a large parameter space for combinatorial and exhaustive search optimization algorithms. Thus, in our FDTD code we implemented an optimization algorithm based on GSL routines to maximize/minimize a function [D3.4].

We focused on the maximization of the received **E** field by maintaining a small variance level during the optimization procedure. Simulations are centred at 3.75 GHz and we also considered a cluster of diodes. Figure 3-7 shows the received **|E|** field before and after the optimization of the RIS. After the optimization there is an increment of the received signal where we place the receiver.

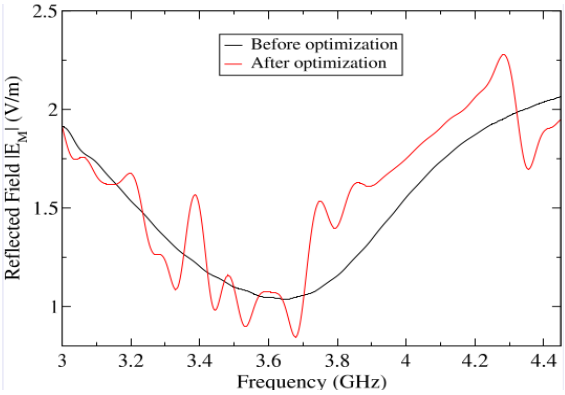

Figure 3-7 Received E field before and after the optimization

Figure 3-8 shows the 2D distribution of the **E** field on the configured RIS after the optimization procedure. Values of the capacitance are limited between the 0.1 pF and 1.0 pF range. The electric field strength is greater w.r.t. the non-optimized RIS.

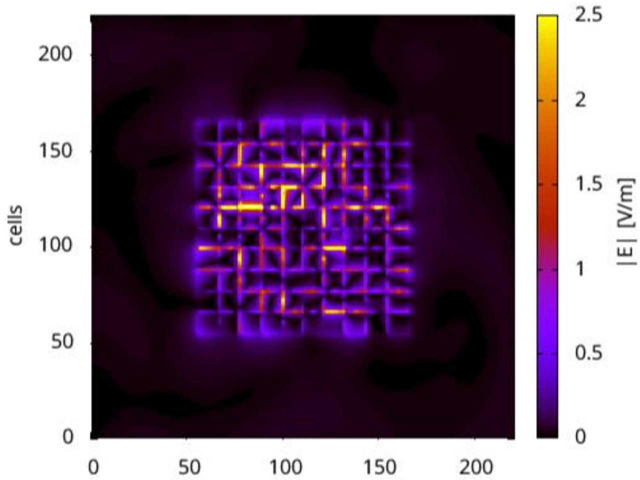

Figure 3-8 Distribution of the magnitude of the electric field along y-axis on the metasurface at the frequency 3.75 GHz with optimized values of the diodes.

By setting the diode states, we simulate the RIS. This procedure can also consider a scenario when an obstacle is within the simulation domain. The obstacle acts as a block that prevents the LOS path between the source, consisting by one or more plane waves, and the receiver. The source is random and is generated to be hidden by the obstacle.

The obstacle is modeled as a PEC plane or as an absorbing material by setting the conductivity and the electric permittivity in the FDTD scheme. Moreover, the PEC blockage can be also surrounded by one or more layers of absorbing material in order to reduce diffraction from its edges. Figure 3-9 shows the FDTD simulation domain with the RIS hit by a plane wave. We modeled the obstacle as a PEC covered by absorbing layer material and it blocks the LOS path to the receiver placed beyond the obstacle. The FDTD domain is: Lx = 231 mm, Ly = 271 mm, Lz = 231 mm.

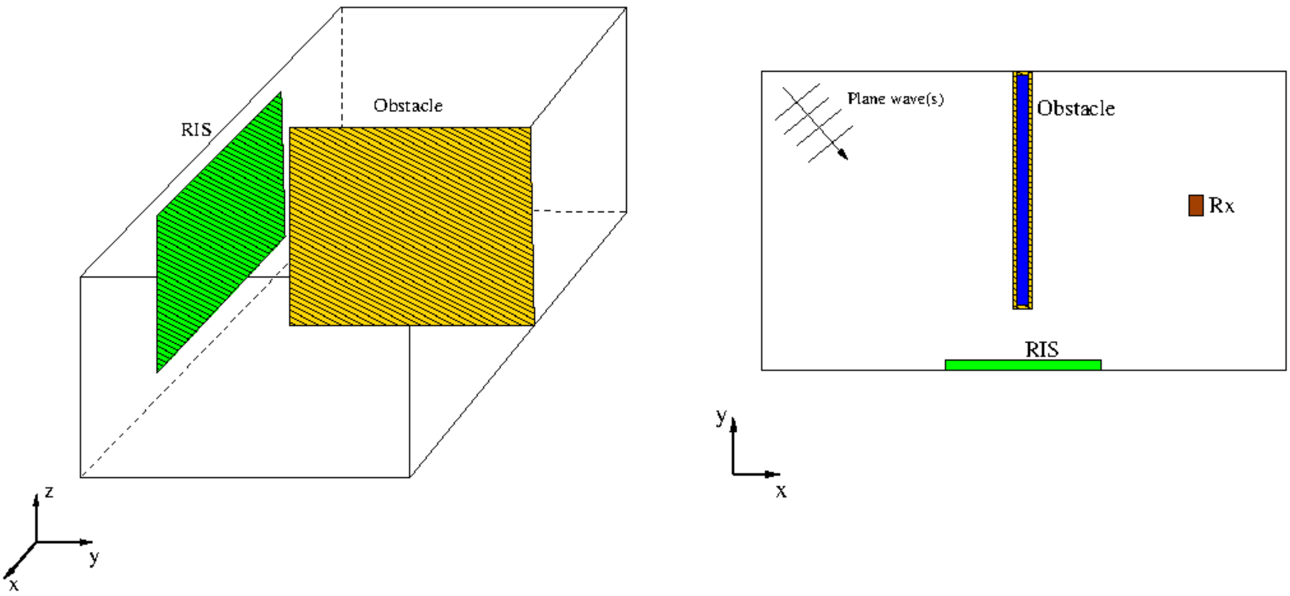

Figure 3-9 Sketch of the FDTD simulation domain with the presence of an obstacle; the golden frame surrounding the obstacle indicates the absorbing material layer. Front view on the left, top view on the right.

Figure 3-10 reports the magnitude of the received **E** field collected by the receiver behind the obstacle. Also in this case we applied the same optimization algorithm used before in order to try to improve the received signal. Also in this case we focused on maximization of the received signal by maintaining a small variance. The electric field after the optimization procedure exhibits an improved signal w.r.t. the initial condition.

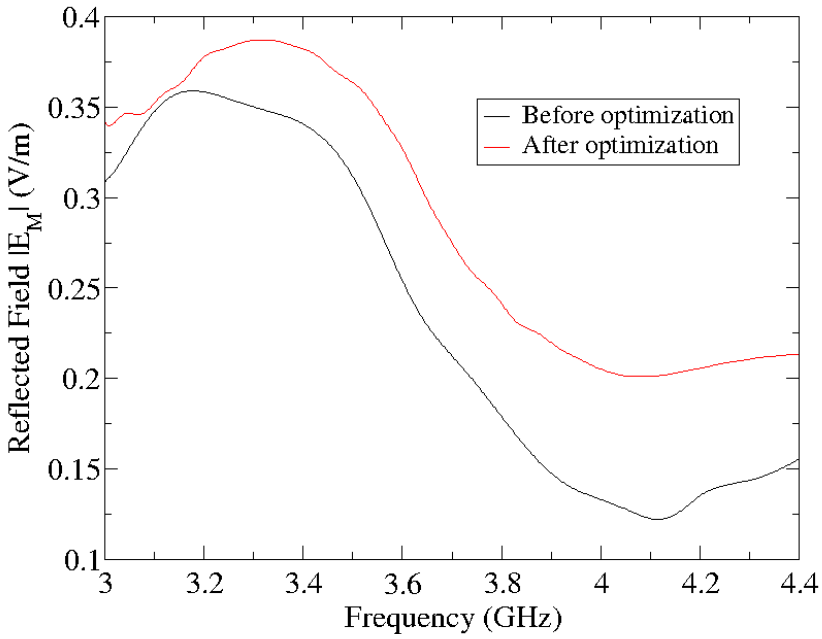

Figure 3-10 Received E field before and after the optimization with the presence of an obstacle.

3.3.4 Conclusion

We have integrated the modelled the RIS in our FDTD code starting from the GSTCs and then moved to adopting circuital elements such as varactors. The model allows us to simulate a RIS hit by one or more plane waves with a desired or random angle of incidence, polarization and intensity. For an RIS which consists of many elements an optimization procedure is required, even if we considered a group of diodes instead a single element.

We also simulated the scenario when radio waves are vulnerable to a blockage, e.g. walls, objects and so on. In the FDTD simulation this blockage can be made by different absorbing or reflecting material. In this case the RISs can be deployed to provide signal coverage to a desired target where there is no LOS path from the source. Also in this case the optimization procedure can be used to improve the signal strength.

Future work is devoted to increase the RIS dimensions and hereafter the whole simulation domain thus increasing the computational burden of a single run. We can simulate larger geometries that emulate complex propagation scenarios by using parallel supercomputers. This is made possible by the access provided through a recent award that we have received by the European High Performance Computing Joint Undertaking (EuroHPC JU) [EHP].

3.4 Self-consistent method for estimating the average EMFEU in complex scattering environments

This section presents a self-consistent model to estimate the EMFEU in RC, which is a controllable laboratory environment to emulate *Rician* multipath fading. The RC structure and basic operation have been described in [D6.2] and [D3.1].

3.4.1 Introduction

We are concerned about the estimation of the average EMF in smart indoor electromagnetic environments assisted by the RIS. The problem requires considering the wave scattering and absorption from nearby objects and walls, and their influence on the dynamic optimization of the RIS reflection properties. The EMF energy is confined within the environment and decays through absorption (walls, objects, engineered surfaces), leakage (apertures, gaskets), and dissipation within receiver loads. Original scientific studies have tackled the optimization of the RIS when are almost exclusively operated in quasi-free-space conditions. Recent efforts have been devoted to model the multipath fading in RIS-assisted communication channels in order to evaluate the related MIMO performance metrics. However, the multipath fading is included in the channel model as additive or multiplicative random noise, without capturing the multiple interaction mechanisms between RIS and environment that change the behaviour of channel propagation. We extend an existing RC theory that is grounded on power balance methods. The RC is an electrically large, shielded metallic room with irregular geometry created by a movable paddle-like mechanical stirrer. The EMF inside an RC is best modelled through statistical methods. Inherently, it has been shown that a receiving antenna operating inside an RC is illuminated by both unstirred and stirred waves, whose coexistence give raise to field Rician field distributions. Here we propose a self-consistent model that accounts for the power balance between the power carried by LOS coherent beams generated by the RIS towards the users, and the power gathered by the NLOS stochastic EMF confined within the RC. The theory can be easily extended to predict the field received by multiple UE terminals, either addressed by the same or different RIS devices.

3.4.2 System Model

We model the system depicted in Figure 3-11 where the RIS is excited by a transmitting antenna in LOS and re-radiates towards multiple users.

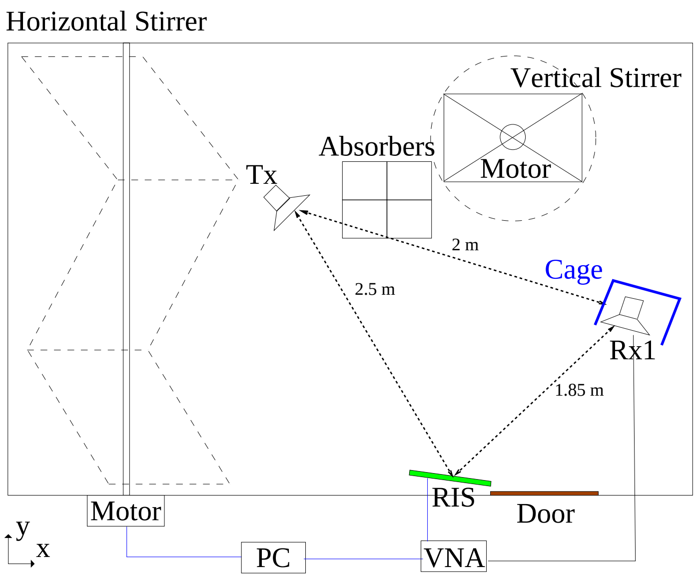

Figure 3-11 Experimental setup of a RIS-assisted reverberation chamber for indoor multipath fading emulation.

After a first reflection off the RIS, it is assumed the EMF arrives at the receivers and continues bouncing around the metallic cavity, encountering the stirrer, and thus becoming part of the reverberant background. This *single-bounce approximation* is effectively used to separate stirred from unstirred components. While there exist multiple unstirred components within an RC, we assume that the one operated by an (optimized) RIS becomes dominant at equilibrium. This assumption stands at the core of the power balance model previously formulated in [D6.2].

In order to estimate the EMFEU in RC we exploit the coexistence of coherent and incoherent components at UE, leading to a Rician distribution of the received EMF. Consequently, the mathematical expression of the statistical average of the EMF amplitude reads

$$\bar{P} = \sigma \sqrt{\frac{\pi}{2}}\, L_{1/2}(-K)$$

with $L_{1/2}$ is the Laguerre polynomial of order $1/2$, and which is valid for any user addressed by the RIS. For a single user, the associated Rician K factor is used to calculate the average signal-to-noise of the signal received by the UE

$$K = \frac{\upsilon^2}{2\sigma^2}$$

Here σ^2 coincides with P_{RC} that has been previously calculated through the power balance model, standing on equilibrium between the power transmitted and dissipated through the RC $P_0 = P_{\mathrm{T}}$, with P_0 power scattered through the RC and P_{T} power transmitted to the chamber through the RIS. The variance of the complex Cartesian component of the field inside an RC is given by [HMO+94]

$$\sigma^2 = \frac{\eta\, Q\, \lambda}{12\, \pi\, V}\, U_{\mathrm{Sk}}\, P_{\mathrm{T}}$$

Defining P_{RIS} as the power re-radiated by the RIS towards the UE, υ^2 is obtained by the Friis' transmission formula, and it is expressed through an improved path-loss model that accounts for realistic design and experimental imperfections [JOL+22]

$$\upsilon^2 = \frac{\eta\, \lambda^2}{16\, \pi^2\, \mathrm{r}_{\mathrm{TS}}^2\, \mathrm{r}_{\mathrm{SR}}^2}\, \mathrm{D}_{\mathrm{Sk}}\, \mathrm{G}_{\mathrm{T}}\, P_{\mathrm{T}}$$

where r_{TS} indicates the distance between the transmitting antenna and the centre of the RIS, while r_{SR} indicates the distance between the centre of the RIS and the receiving antennas, and which does not account for polarization mismatch of both the RIS and the UE antenna. The RIS directivity towards the user D_k depends on the local reflectivity phases of the individual unit cells φ_n, $n = 1, \cdots, \mathrm{N}$

$$\mathrm{D}_{\mathrm{Sk}} = \mathrm{G}_{\mathrm{TS}}\, R(\varphi_0, \cdots, \varphi_N)\, \mathrm{G}_{\mathrm{SR}}$$

Upon cascaded substitution in the expression of the Rician K factor gives, assuming that both the UE and the UE antenna are omnidirectional and polarization matched

$$K = \frac{3}{2} \frac{\lambda V}{Q U_{\mathrm{Sk}}} \frac{\mathrm{D}_{\mathrm{Sk}}\, \mathrm{G}_{\mathrm{T}}}{\mathrm{r}_{\mathrm{TS}}^2\, \mathrm{r}_{\mathrm{SR}}^2}$$

As pointed out in [HHL+06] for a device under test in the context of electromagnetic compatibility (EMC), we might need to generalize the model by considering polarization mismatch and directivity of the receiving antenna. Here, this process would involve both the RIS unit cells and the UE antenna. It is worth noticing, in presence of multiple UEs, that the RC field perceived by the two users would be the same, while the K factor would be different on account of the power balance equations. This is motivated by the fact that the stochastic field is generated by the fraction of power that is uncontrolled by the RIS and contributes to the field mixing through the metallic mode stirrer. The crucial part of the method is the self-consistent estimation of σ^2 and υ^2, which are related to each other through the power balance model introduced in [D6.2]. This resulted in an 'imbalance' term here represented as U_{Sk}. More precisely, the coherent and reverberant field amplitude are intertwined since: i) the excitation amplitude of the RIS is given by both direct and random (RC) illumination; ii) the RC field amplitude depends on the strength of the two LOS component generated by the RIS towards the users.

3.4.3 Results

Scattering parameter measurements obtained from the RC testbed adopted in WP7 are exploited to understanding the field statistics within complex propagation environments assisted by the RIS.

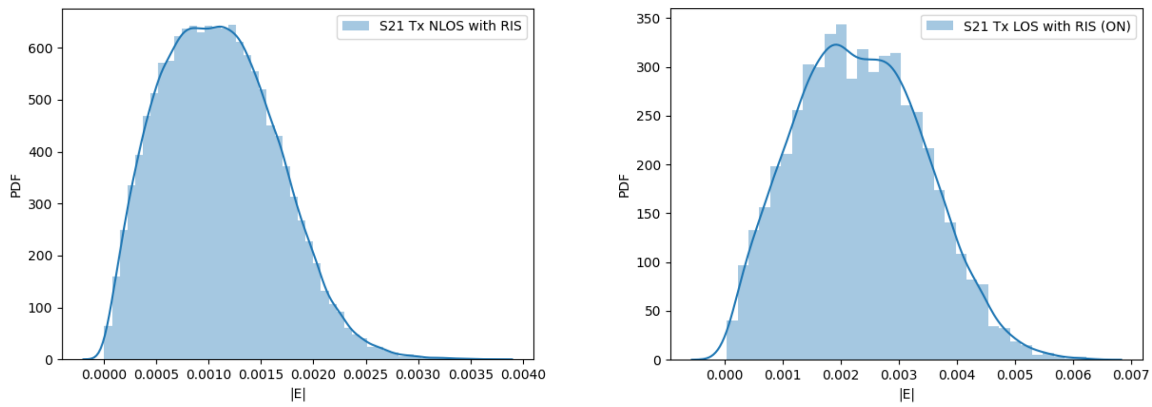

(a) **(b)**

Figure 3-12 Experimental setup of a RIS-assisted reverberation chamber for indoor multipath fading emulation.

The experimental set-up is depicted in Figure 3-11 and shows that: i) the transmitting horn antenna provides direct illumination of the RIS operating at 27 GHz and statistically independent samples have been collected within a narrow frequency bandwidth around the RIS operational frequency; ii) the receiving horn antenna points directly to the RIS and is in NLOS of the transmitting horn antenna iii) the RC metallic mode stirrer is positioned behind the RIS; vi) the two antennas and the RIS communicate in presence of environment (wall and stirrer) backscattering. We have observed that the predicted behaviour due to RIS illumination within an isotropic scattering environment follows a Rician distribution as predicted. Moreover, the received power becomes dominated by the LOS components upon optimization of the RIS. A weak LOS component is developed in any real-life RC where the field distribution is closer to a Rayleigh distribution since $\upsilon^2 \ll 2\sigma^2$. This is observed also for a non-optimal RIS operating in RC as well as for a transmitting antenna pointing towards the RC metallic mode stirrer. It is expected that a strong LOS component developed in RC by more effective RIS optimization and for larger RIS devices, i.e., with a higher number of controllable unit cells, that would create a non-central Gaussian distributed fading regime. The measured distributions depicted in Figure 3-12 (a) and (b) show the predicted transition between Rayleigh to Rician multipath fading.

3.4.4 Conclusion

We have completed the derivation of a self-consistent model for the estimation of the field received by users operated in complex scattering environments partially controlled by the RIS. We have studied the case where a single RIS control the transmission towards a UE antenna and have. The model predicts the change of EMF density function from Rayleigh to Rician distributed fading in presence of an optimized RIS creating a virtual LOS towards the UE. Preliminary WP7 measurements confirm this prediction. The power balance model developed in [D6.2] has been used to devise an expression of the Rician K factor, which is useful to predict and control the EMFEU in RIS-assisted indoor environments. Future work is devoted to verifying and improving this model through numerical simulations and laboratory experiments grounded on the RC facility.

3.5 RIS measurements in the reverberation chamber

This section presents the experimental activities performed in the CNIT lab with a commercial 5G BS, VNA, RIS in the RC.

3.5.1 Introduction

The experimental activity was preceded by the preparation of the measurement set-up, firstly arranged, and then investigated in WP3. Preparatory tasks alongside the project development have been completed to start the main activity in WP6 and in WP7. Preliminary tasks were: i) install and configure a commercial 5G BS within our laboratory; ii) reproduce a desired real-life environment by using the RC before adding the RIS in the set-up [HHL06], [BGM15]. Once the set-up was ready for measurements, we firstly began by using the Vector Network Analyzer (VNA) and horn antennas in order to configure the RIS. Set-up details are reported in [D3.4]. Subsequently, we replaced the VNA with the 5G BS and horn antenna with the UE. The UE is provided by the mobile operator. Both VNA, 5G BS, UE and horn antenna operate at 26.95 GHz, i.e. the licensed frequency [MDB23]. The measurements have been performed within the RC. The RC is able to emulate multipath channel for our tests and in contrast to the anechoic chamber it can stress the RIS operation by multiple reflections.

3.5.2 Measurements setup

Figure 3-13 a) and b) show the adopted set-up in the RC. In these measurements we used:

- VNA to collect scattering parameters;
- T_x and R_x horn antennas;
- PC to control the RIS;
- absorbers to tune the PDP and the time delay spread;
- 5G BS;
- UE_1 and UE_2;
- RIS.

The RC is opportunely loaded by absorbing material in order to: i) reproduce a real-life environment [ITU17] and ii) block the direct connection between the Tx and Rx antennas. Moreover, we place the Rx antenna within an absorbing box, we called it: “absorbing cage”, to reduce the multipath contributes due reflecting walls of the RC and to emphasize the main contribute due to the RIS.

a) RIS within the RC, behind the RC door.

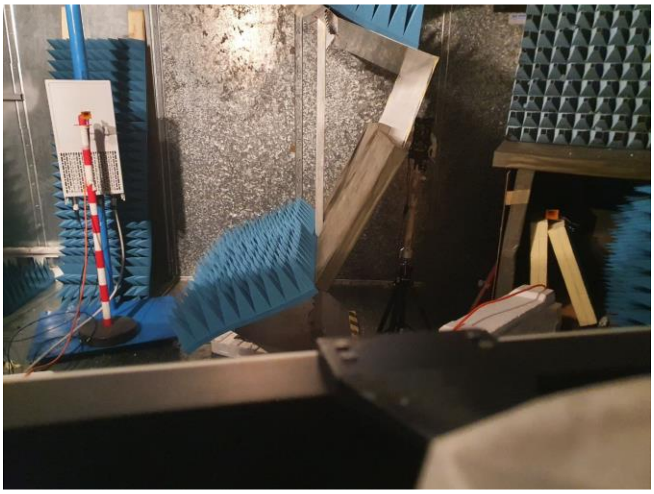

b) Picture of the setup.

Figure 3-13 Setup.

The scenario of Figure 3-13 has been explored in WP3 where we reported the comparison of the measured S21 when the RIS was optimized vs a random configuration. It has been shown the capability of the RIS to increase the received signal. The correct configuration of the RIS is given by a software provided by partner who designed and realized the RIS.

Hereafter, we added a second receiver to replicate an operating concept of the RIS-aided communication. More precisely, the selected receiver acts as an intended-user whereas the other receiver acts as a non-intended user. In some situation the presence of a non-intended user does not affect the RIS functionalities and the EMFEU to the desired target, e.g. the intended user. Detailed discussion of metrics can be found in [D2.3] (deployment scenarios and use cases), [D2.4] (metrics) and [D6.1] (initial views on architecture and control signaling aspects).

In our tests we assumed both LOS between T_x/RIS and between RIS/$R_{x1,2}$. The operation frequency is 26.95 GHz both with the VNA and the 5G BS. Figure 3-14 a) reports a schematic of the setup with two horn antennas as receivers. The two receivers of Figure 3-14 b) R_{x1}, within the absorbing cage, denotes the intended user whereas R_{x2} denotes the non-intended user respectively.

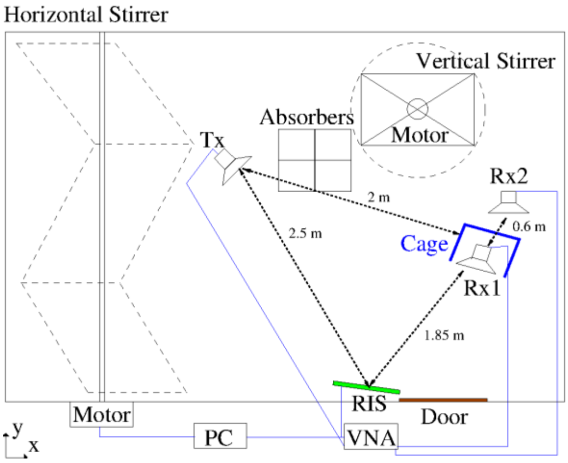

a) **Schematic**

b) **Picture**

Figure 3-14 Setup with VNA and two horn antennas as receivers.

3.5.3 Results

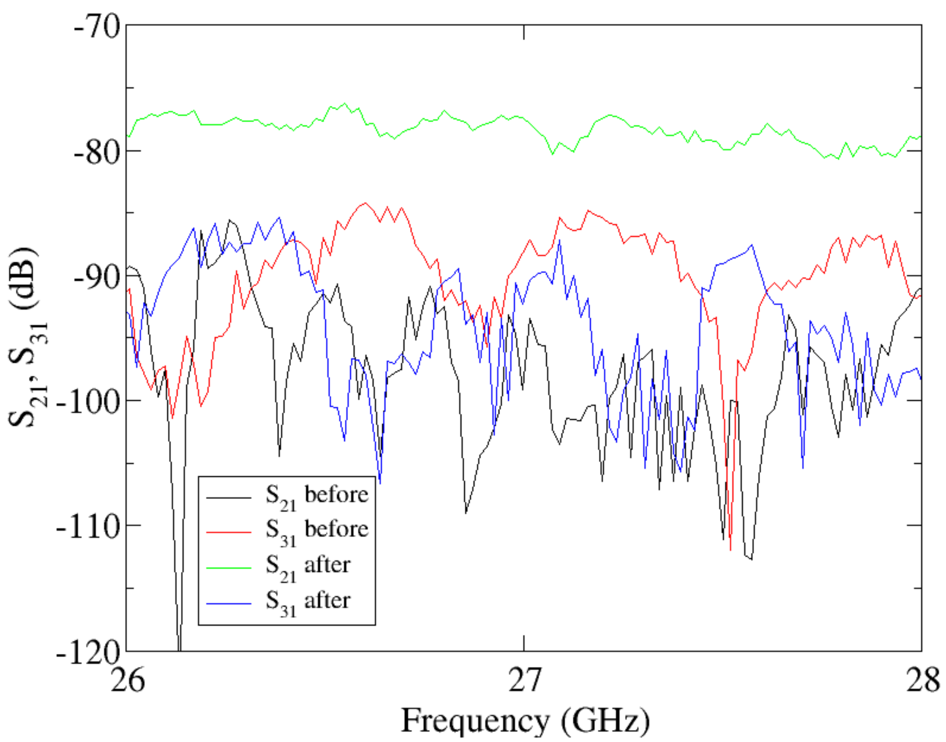

Figure 3-15 Comparison of S_{21} and S_{31} before and after RIS optimization.

Figure 3-15 shows the S_{21} and S_{31} when the RIS is randomly configured and when it is opportunely configured, labelled as “before” and “after” respectively. The S_{21} represents the signal transmitted by the horn antenna labelled as T_x, reflected by the RIS and then received by R_{x1}, whereas S_{31} refers to the receiver labelled as R_{x2} in Figure 3-14 b). We noticed that, starting with an S_{31} higher w.r.t. the S_{21}

when the RIS is optimized, it is able to focus the transmitting signal to the desired target, namely the R_{x1}.

Beside the VNA and horn antennas, we replaced them by the 5G BS and UEs respectively, as reported in Figure 3-16. Also in this case the RIS has been configured by running an optimization code which requires as input the coordinates of the T_x and angles of the UE_1 such as azimuth and elevation angle respectively. In these tests, we recorded the RSRP at the UE_1 side and UE_2 side. The RSRP is recorded by means of a proprietary software, namely the QXDM. During tests we generated data traffic to keep active the data link active.

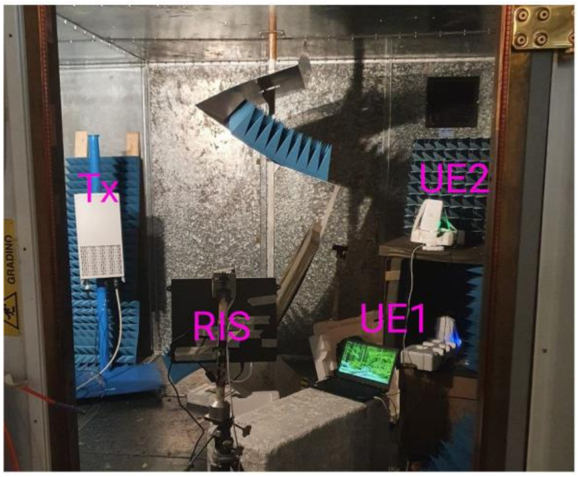

Figure 3-16 Picture of the setup previously used with VNA and horn antennas, here replaced by 5G BS and UEs respectively.

Considering two UEs, during the acquisition of the RSRP the steps are the following (as illustrated by Figure 3-17):

- starting from a random configuration of the RIS;
- after 30 s we loaded the RIS configuration which focus the signal to the UE1 (the intended-user);
- after 90 s we loaded a random configuration of the RIS.

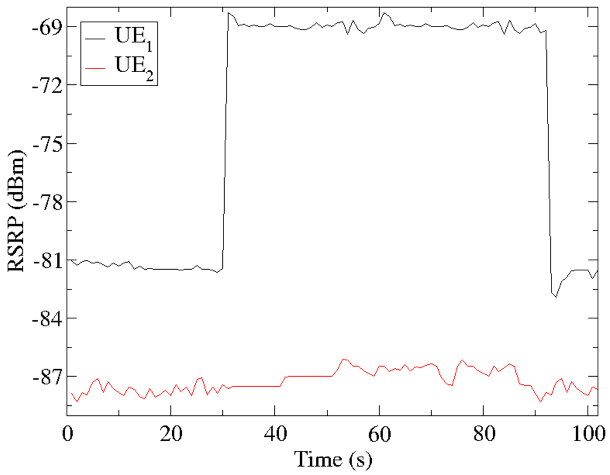

Figure 3-17 RSRP recorded by the UE_1 and UE_2.

Figure 3-17 shows the capability of the RIS, when it is properly configured, to increase the RSRP related to the intended user. At the same time, the choice to select the UE1 does not affect the UE2, i.e. the non intended user.

3.5.4 Conclusion

We tested the RIS at the mmWave (26.95 GHz) within the RC. We firstly adopted the VNA to find the configuration of the RIS and then we employed the 5G BS and UEs to test the RIS with a commercial 5G system. Despite the RC emulates a rich multipath environment, it does not affect the optimal RIS operation. The high directivity of both 5G devices and horn antennas ensure a good direct connection between T_x, RIS and R_x. We showed that the RIS is capable to focus the received signal to the intended user w.r.t. an undesirable user. This effect can be noticed by using both VNA and 5G BS.

4 Conclusions

In this deliverable, we summarize the final results of Task 6.2 on Sustainable RIS Solutions Design for EE, EMFEU and SSE and Task 6.3 on assessment methods of EE, EMFEU and SSE Improvements.

We present twenty solutions and innovations to boost the EE, EMFEU or SSE metrics and five new methods to assess these metrics.

5 References

The sign * indicates a reference which includes a contribution from RISE-6G project.

*	[AMC+22]	F. E. Airod, M. Merluzzi, A. Clemente and E. C. Strinati, "Blue Communications for Edge Computing: the Reconfigurable Intelligent Surfaces Opportunity," GLOBECOM 2022 - 2022 IEEE Global Communications Conference, Rio de Janeiro, Brazil, 2022, pp. 6396-6401, doi: 10.1109/GLOBECOM48099.2022.10001599. Available at: https://arxiv.org/pdf/2211.13053.pdf.
*	[ADS+23]	A. Albanese, F. Devoti, V. Sciancalepore, M. D. Renzo, A. Banchs, and X. Costa-Perez, “ARES: Autonomous RIS solution with Energy harvesting and Self-configuration towards 6G,” in ArXiv, 2023, arXiv:2303.01161v1. Available at: https://arxiv.org/pdf/2303.01161.pdf.
	[AK14]	D. Altinel and G. K. Kurt, "Statistical models for battery recharging time in RF energy harvesting systems," 2014 IEEE Wireless Communications and Networking Conference (WCNC), Istanbul, Turkey, 2014, pp. 636-641, doi: 10.1109/WCNC.2014.6952122.
*	[AKW+21]	G. C. Alexandropoulos, K. Katsanos, M. Wen and D. B. Da Costa, "Safeguarding MIMO Communications with Reconfigurable Metasurfaces and Artificial Noise," ICC 2021 - IEEE International Conference on Communications, Montreal, QC, Canada, 2021, pp. 1-6, doi: 10.1109/ICC42927.2021.9501003. Available at: https://arxiv.org/abs/2005.10062.
*	[AKW+23]	G. C. Alexandropoulos, K. D. Katsanos, M. Wen and D. B. Da Costa, "Counteracting Eavesdropper Attacks Through Reconfigurable Intelligent Surfaces: A New Threat Model and Secrecy Rate Optimization," in IEEE Open Journal of the Communications Society, vol. 4, pp. 1285-1302, 2023, doi: 10.1109/OJCOMS.2023.3282814. Available at: https://www.techrxiv.org/articles/preprint/Counteracting_Eavesdropper_Attacks_Through_Reconfigurable_Intelligent_Surfaces_A_New_Threat_Model_and_Secrecy_Rate_Optimization/21674759/1.
*	[APV+22-1]	N. Awarkeh, D. -T. Phan-Huy, R. Visoz and M. D. Renzo, "A Novel RIS-Aided EMF-Aware Beamforming Using Directional Spreading, Truncation and Boosting," 2022 Joint European Conference on Networks and Communications & 6G Summit (EuCNC/6G Summit), Grenoble, France, 2022, pp. 7-12, doi: 10.1109/EuCNC/6GSummit54941.2022.9815800. Available at: https://hal.science/hal-03838377/document.
*	[APV+22-2]	N. Awarkeh, D. -T. Phan-Huy and M. D. Renzo, "A Novel RIS-Aided EMF Exposure Aware Approach using an Angularly Equalized Virtual Propagation Channel," 2022 Joint European Conference on Networks and Communications & 6G Summit (EuCNC/6G Summit), Grenoble, France, 2022, pp. 500-505, doi: 10.1109/EuCNC/6GSummit54941.2022.9815608. Available at: https://hal.science/hal-03838367/document.
*	[APV21]	N. Awarkeh, D. -T. Phan-Huy and R. Visoz, "Electro-Magnetic Field (EMF) aware beamforming assisted by Reconfigurable Intelligent Surfaces," 2021 IEEE 22nd International Workshop on Signal Processing Advances in Wireless Communications (SPAWC), Lucca, Italy, 2021, pp. 541-545, doi: 10.1109/SPAWC51858.2021.9593226.
	[BGM15]	L. Bastianelli, L. Giacometti, V. Mariani Primiani and F. Moglie, "Effect of absorber number and positioning on the power delay profile of a reverberation chamber," 2015 IEEE International Symposium on Electromagnetic Compatibility (EMC), Dresden, Germany, 2015, pp. 422-427, doi: 10.1109/ISEMC.2015.7256199.
	[BRR+19]	E. Basar, M. Di Renzo, J. De Rosny, M. Debbah, M. -S. Alouini and R. Zhang, "Wireless Communications Through Reconfigurable Intelligent Surfaces," in IEEE Access, vol. 7, pp. 116753-116773, 2019, doi: 10.1109/ACCESS.2019.2935192.
	[C+19]	D. Colombi et al., "Assessment of Actual Maximum RF EMF Exposure from Radio Base Stations with Massive MIMO Antennas," 2019 PhotonIcs & Electromagnetics Research Symposium - Spring (PIERS-Spring), Rome, Italy, 2019, pp. 570-577, doi: 10.1109/PIERS-Spring46901.2019.9017343.
	[C+21]	M. R. Castellanos, D. Ying, D. J. Love, B. Peleato and B. M. Hochwald, "Dynamic Electromagnetic Exposure Allocation for Rayleigh Fading MIMO Channels," in IEEE Transactions on Wireless Communications, vol. 20, no. 2, pp. 728-740, Feb. 2021, doi: 10.1109/TWC.2019.2948916.
*	[CBM23-1]	E. Colella, L. Bastianelli, V. Mariani Primiani, “FDTD Full Wave Simulations of Reconfigurable Intelligent Surfaces”, in EMC Europe 2023, Sep. 2023. Available at: https://arxiv.org/abs/2309.12414.
*	[CBM23-2]	E. Colella, L. Bastianelli, F. Moglie, V. Mariani Primiani, “Near Field Optimization Algorithm for Reconfigurable Intelligent Surface”, in URSI GASS 2023, Aug. 2023. Available at: https://arxiv.org/abs/2309.12448.
	[CDS12]	A. Clemente, L. Dussopt, R. Sauleau, P. Potier and P. Pouliguen, ”Focal Distance Reduction of Transmit-Array Antennas Using Multiple Feeds,” in IEEE Antennas and Wireless Propagation Letters, vol. 11, pp. 1311-1314,2012, doi: 10.1109/LAWP.2012.2227105.
	[CEA21]	L. Chiaraviglio, A. Elzanaty and M. -S. Alouini, "Health Risks Associated With 5G Exposure: A View From the Communications Engineering Perspective," in IEEE Open Journal of the Communications Society, vol. 2, pp. 2131-2179, 2021, doi: 10.1109/OJCOMS.2021.3106052.
	[CLS+12]	A. Clemente, L. Dussopt, R. Sauleau, P. Potier and P. Pouliguen, ”Focal Distance Reduction of Transmit-Array Antennas Using Multiple Feeds,” in IEEE Antennas and Wireless Propagation Letters, vol. 11, pp.

		1311-1314, 2012, doi: 10.1109/LAWP.2012.2227105.
*	[D2.3]	RISE-6G Deliverable D2.3 “Reference system, scenarios and use cases analysis: final results”, Feb. 2022. Available at: https://rise-6g.eu/.
*	[D2.4]	RISE-6G Deliverable D2.4 “Metrics and KPIs for RISE wireless systems analysis: final results”, Feb. 2022. Available at: https://rise-6g.eu/.
*	[D3.1]	RISE-6G Deliverable D3.1 “Preliminary RIS model and measurement campaigns”, May 2022. Available at: https://rise-6g.eu/.
*	[D3.4]	RISE-6G Deliverable D3.4 “Optimised RIS prototypes for PoCs and model assessment test”, June 2023. Available at: https://rise-6g.eu/.
*	[D4.4]	RISE-6G Deliverable D4.4 “Multi-user techniques and connectivity of RIS based communication and mobile edge computing (Final Specifications)”, Sept. 2023. Available at: https://rise-6g.eu/.
*	[D6.1]	RISE-6G Deliverable D6.1 "Network architectures & deployment strategies with RIS for enhanced EE, EMFEU, and SSE (Intermediary Specifications)" May 2022. Available at: https://rise-6g.eu/.
*	[D6.2]	RISE-6G Deliverable D6.2 “Sustainable RIS solutions design for EE, EMFEU and SSE (Intermediary Specifications)”. Available at: https://rise-6g.eu/.
	[DAH98]	D. A. Hill, “Plane wave integral representation for fields in reverberation chambers,” IEEE Trans. Electromagn. Compat., vol. 40, no. 3, pp. 209-217, Aug. 1998.
	[DTT16]	E. Degirmenci, B. Thors and C. Törnevik, "Assessment of Compliance With RF EMF Exposure Limits: Approximate Methods for Radio Base Station Products Utilizing Array Antennas With Beam-Forming Capabilities," in *IEEE Transactions on Electromagnetic Compatibility*, vol. 58, no. 4, pp. 1110-1117, Aug. 2016, doi: 10.1109/TEMC.2016.2550611.
*	[DVR+22]	V. Degli-Esposti, E. M. Vitucci, M. D. Renzo and S. A. Tretyakov, "Reradiation and Scattering From a Reconfigurable Intelligent Surface: A General Macroscopic Model," in IEEE Transactions on Antennas and Propagation, vol. 70, no. 10, pp. 8691-8706, Oct. 2022, doi: 10.1109/TAP.2022.3149660. Available at: https://arxiv.org/pdf/2107.12773.pdf.
	[EHP]	The European High Performance Computing Joint Undertaking (EuroHPC JU). https://eurohpc-ju.europa.eu/index_en.
	[F+19]	B. Feng et al., “Secure transmission strategy for intelligent reflecting surface enhanced wireless system,” in Proc. IEEE WCSP, Xi’an, China, Oct. 2019, pp. 1–6.
	[FCB21]	F. Costa and M. Borgese, "Electromagnetic Model of Reflective Intelligent Surfaces," in IEEE Open Journal of the Communications Society, vol.2, pp. 1577–1589, 2021, doi: 10.1109/OJCOMS.2021.3092217
*	[FZR+23]	R. K. Fotock, A. Zappone, and M. D. Renzo, “ENERGY EFFICIENCY MAXIMIZATION IN RIS-AIDED NETWORKS WITH GLOBAL REFLECTION CONSTRAINTS”, in ArXiv, 2023, arXiv: 2303.03239v1. Available at: https://arxiv.org/pdf/2303.03239.pdf.
*	[GPHS22]	H. Guo, D. -T. Phan-Huy and T. Svensson, "Electromagnetic Field Exposure Avoidance thanks to Non-Intended User Equipment and RIS," 2022 IEEE Globecom Workshops (GC Wkshps), Rio de Janeiro, Brazil, 2022, pp. 1537-1542, doi: 10.1109/GCWkshps56602.2022.10008663. Available at: https://arxiv.org/pdf/2209.10367.pdf.
*	[GPHS23]	H. Guo, D-T. Phan-Huy, and T. Svensson, “Integrated Sensing and Communication System with Non-collaborative Electromagnetic Field Exposure-constrained Users Assisted by RIS”, journal under preparation.
*	[GWW+23]	Q. Gontier, Charles Wiame, S. Wang, M. D. Renzo, J. Wiart, F. Horlin, C. Tsigros, C. Oestges, and P. D. Doncker, “Joint Metrics for EMF Exposure and Coverage in Real-World Homogeneous and Inhomogeneous Cellular Networks,” in ArXiv, 2022, arXiv:2302.03559. Available at: https://arxiv.org/pdf/2302.03559.pdf.
	[Hexa-X-D7.2]	Hexa-X, Deliverable D7.2 “Special-purpose functionalities: intermediate solutions”. Available at: https://hexa-x.eu/wp-content/uploads/2022/05/Hexa-X_D7.2_v1.0.pdf.
	[Hexa-X-D7.3]	Hexa-X, Deliverable D7.2 “Special-purpose functionalities: final solutions”. Available at: https://hexa-x.eu/wp-content/uploads/2023/06/Hexa-X_D7.3_v1.0.pdf.
	[HHL+06]	C. L. Holloway, D. A. Hill, J. M. Ladbury, P. F. Wilson, G. Koepke and J. Coder, "On the Use of Reverberation Chambers to Simulate a Rician Radio Environment for the Testing of Wireless Devices," in IEEE Transactions on Antennas and Propagation, vol. 54, no. 11, pp. 3167-3177, Nov. 2006, doi: 10.1109/TAP.2006.883987.
	[HKG+21]	C. L. Holloway, E. F. Kuester, J. A. Gordon, J. O'Hara, J. Booth and D. R. Smith, "An Overview of the Theory and Applications of Metasurfaces: The Two-Dimensional Equivalents of Metamaterials," in IEEE Antennas and Propagation Magazine, vol. 54, no. 2, pp. 10-35, April 2012, doi: 10.1109/MAP.2012.6230714.
	[HMO+94]	D. A. Hill, M. T. Ma, A. R. Ondrejka, B. F. Riddle, M. L. Crawford and R. T. Johnk, "Aperture excitation of electrically large, lossy cavities," in IEEE Transactions on Electromagnetic Compatibility, vol. 36, no. 3, pp. 169-178, Aug. 1994, doi: 10.1109/15.305461.
	[HPR+20]	S. Hong, C. Pan, H. Ren, K. Wang and A. Nallanathan, "Artificial-Noise-Aided Secure MIMO Wireless Communications via Intelligent Reflecting Surface," in IEEE Transactions on Communications, vol. 68, no. 12, pp. 7851-7866, Dec. 2020, doi: 10.1109/TCOMM.2020.3024621.

	[ICN20]	"ICNIRP guidelines for limiting exposure to electromagnetic fields (100 kHz – 300 GHz)," https://www.icnirp.org/cms/upload/publications/ICNIRPrfgdl2020.pdf
	[IEA+22]	H. Ibraiwish, A. Elzanaty, Y. H. Al-Badarneh and M. -S. Alouini, "EMF-Aware Cellular Networks in RIS-Assisted Environments," in IEEE Communications Letters, vol. 26, no. 1, pp. 123-127, Jan. 2022, doi: 10.1109/LCOMM.2021.3120688.
	[ITU17]	Report ITU-R P.2406-0: Studies for short-path propagation data and models for terrestrial radiocommunication systems in the frequency range 6 GHz to 100 GHz",ITU-R Radiocommunication, 09/2017. Available at: https://www.itu.int/dms_pub/itu-r/opb/rep/R-REP-P.2406-2017-PDF-E.pdf.
	[J+21]	Z. Ji et al., "Secret Key Generation for Intelligent Reflecting Surface Assisted Wireless Communication Networks," in IEEE Transactions on Vehicular Technology, vol. 70, no. 1, pp. 1030-1034, Jan. 2021, doi: 10.1109/TVT.2020.3045728.
	[JOL+22]	J. Jeong, J. H. Oh, S. Y. Lee, Y. Park and S. -H. Wi, "An Improved Path-Loss Model for Reconfigurable-Intelligent-Surface-Aided Wireless Communications and Experimental Validation," in IEEE Access, vol. 10, pp. 98065-98078, 2022, doi:10.1109/ACCESS.2022.3205117.
	[JYL+20]	X. Jia, F. Yang, X. Liu, M. Li and S. Xu, "Fast Nonuniform Metasurface Analysis in FDTD Using Surface Susceptibility Model," in IEEE Transactions on Antennas and Propagation, vol. 68, no. 10, pp. 7121-7130, Oct. 2020, doi: 10.1109/TAP.2019.2957317.
*	[KA23]	K. D. Katsanos and G. C. Alexandropoulos, "Spatial secrecy spectral efficiency optimization enabled by reconfigurable intelligent surfaces," EUSIPCO, Helsinki, Finland, 4–8 September 2023, pp. 1–5. Available at: https://arxiv.org/pdf/2306.11024.pdf.
	[L99]	T. K. Y. Lo, "Maximum ratio transmission," in IEEE Transactions on Communications, vol. 47, no. 10, pp. 1458-1461, Oct. 1999, doi: 10.1109/26.795811.
	[LLS+21]	X. Lu, J. Lei, Y. Shi, and W. Li, "Intelligent reflecting surface assisted secret key generation," IEEE Signal Process. Lett., vol. 28, pp. 1036–1040, 2021.
*	[LSX+22]	G. Li, C. Sun, W. Xu, M. D. Renzo and A. Hu, "On Maximizing the Sum Secret Key Rate for Reconfigurable Intelligent Surface-Assisted Multiuser Systems," in IEEE Transactions on Information Forensics and Security, vol. 17, pp. 211-225, 2022, doi: 10.1109/TIFS.2021.3138612. Available at: https://hal-centralesupelec.archives-ouvertes.fr/hal-03506039.
	[MAP06]	F. Moglie, A. P. Pastore, "FDTD analysis of plane wave superposition to simulate susceptibility tests in reverberation chambers", in IEEE Transactions on Electromagnetic Compatibility, vol. 48, no. 1, pp. 195—202, Feb. 2006, doi: 10.1109/TEMC.2006.87.07.93
	[MBC22]	M. Merluzzi, S. Bories and E. C. Strinati, "Energy-Efficient Dynamic Edge Computing with Electromagnetic Field Exposure Constraints," 2022 Joint European Conference on Networks and Communications & 6G Summit (EuCNC/6G Summit), Grenoble, France, 2022, pp. 202-207, doi: 10.1109/EuCNC/6GSummit54941.2022.9815625.
	[MBM16]	F. Moglie, L. Bastianelli and V. M. Primiani, "Reliable Finite-Difference Time-Domain Simulations of Reverberation Chambers by Using Equivalent Volumetric Losses," in IEEE Transactions on Electromagnetic Compatibility, vol. 58, no. 3, pp. 653-660, June 2016, doi: 10.1109/TEMC.2016.2548520.
*	[MDB23]	D. Micheli, R. Diamanti, L. Bastianelli, E. Colella, V. Mariani Primiani, F. Moglie, A. Allasia, M. Crozzoli, M. Colombo, "Test of 5G System in the Reverberation Chamber at mm-wave", 17th European Conference on Antennas and Propagation (EuCAP), 26-31 March 2023 DOI: 10.23919/EuCAP57121.2023.10133586. Available at: https://arxiv.org/pdf/2302.14710.pdf.
	[MHM+18]	Morgado, K. M. S. Huq, S. Mumtaz and J. Rodriguez, "A Survey of 5G Technologies: Regulatory, Standardization and Industrial Perspectives," Digital Comm. and Net., no. 4, pp. 87-97, 2018.
*	[MMA+22]	L. Mohjazi, S. Muhaidat, Q. H. Abbasi, M. A. Imran, O. A. Dobre and M. D. Renzo, "Battery Recharging Time Models for Reconfigurable Intelligent Surfaces-Assisted Wireless Power Transfer Systems," in IEEE Transactions on Green Communications and Networking, vol. 6, no. 2, pp. 1173-1185, June 2022, doi: 10.1109/TGCN.2021.3120834. Available at: https://arxiv.org/abs/2007.05227
	[MP+20]	V. M. Primiani et al., "Reverberation chambers for testing wireless devices and systems," in IEEE Electromagnetic Compatibility Magazine, vol. 9, no. 2, pp. 45-55, 2nd Quarter 2020, doi: 10.1109/MEMC.2020.9133241.
	[P+20]	C. Pan et al., "Intelligent reflecting surface aided MIMO broadcasting for simultaneous wireless information and power transfer," IEEE J. Sel. Areas Commun., 2020.
	[PCE+18]	S. Persia, C. Carciofi, S. D'Elia and R. Suman, "EMF evaluations for future networks based on Massive MIMO," 2018 IEEE 29th Annual International Symposium on Personal, Indoor and Mobile Radio Communications (PIMRC), Bologna, Italy, 2018, pp. 1197-1202, doi: 10.1109/PIMRC.2018.8580893.
*	[PBH+22]	D. -T. Phan-Huy, Y. Bénédic, S. H. Gonzalez and P. Ratajczak, "Creating and Operating Areas With Reduced Electromagnetic Field Exposure Thanks to Reconfigurable Intelligent Surfaces," 2022 IEEE 23rd International Workshop on Signal Processing Advances in Wireless Communication (SPAWC), Oulu, Finland, 2022, pp. 1-5, doi: 10.1109/SPAWC51304.2022.9833964.
	[PM10]	Primiani, V.M. and Moglie, F., 2010. "Numerical simulation of LOS and NLOS conditions for an antenna inside a reverberation chamber. Journal of Electromagnetic Waves and Applications," 24(17-18), pp.2319-2331.
*	[PWP+23]	Z. Peng, R. Weng, C. Pan, G. Zhou, M. Di Renzo and A. Lee Swindlehurst, "Robust Transmission Design for RIS-assisted Secure Multiuser Communication Systems in the Presence of Hardware Impairments," in IEEE Transactions on Wireless Communications, doi: 10.1109/TWC.2023.3252046. Available at: https://arxiv.org/pdf/2202.11860.pdf.

	[R+13]	F. Rusek et al., "Scaling Up MIMO: Opportunities and Challenges with Very Large Arrays," in IEEE Signal Processing Magazine, vol. 30, no. 1, pp. 40-60, Jan. 2013, doi: 10.1109/MSP.2011.2178495.
	[R+19]	M. D. Renzo, et al. “Smart Radio Environments Empowered by Reconfigurable AI Meta-Surfaces: an Idea whose Time has Come,” EURASIP J. on Wireless Comm. and Net., May 2019.
*	[R+21-1]	R. Fara, D. -T. Phan-Huy, P. Ratajczak, A. Ourir, M. Di Renzo and J. De Rosny, "Reconfigurable Intelligent Surface-Assisted Ambient Backscatter Communications – Experimental Assessment," 2021 IEEE International Conference on Communications Workshops (ICC Workshops), Montreal, QC, Canada, 2021, pp. 1-7, doi: 10.1109/ICCWorkshops50388.2021.9473842. Available at: https://arxiv.org/ftp/arxiv/papers/2103/2103.08427.pdf.
*	[R+21-2]	R. Fara, P. Ratajczak, D. -T. Phan-Huy, A. Ourir, M. Di Renzo and J. de Rosny, "A Prototype of Reconfigurable Intelligent Surface with Continuous Control of the Reflection Phase," in IEEE Wireless Communications, vol. 29, no. 1, pp. 70-77, February 2022, doi: 10.1109/MWC.007.00345. Available at: https://arxiv.org/ftp/arxiv/papers/2105/2105.11862.pdf.
	[RH10]	Randy L. Haupt, ”Antenna Arrays: A Computational Approach,” Wiley-IEEE Press, 2010
*	[S+21]	E. C. Strinati et al., "Wireless Environment as a Service Enabled by Reconfigurable Intelligent Surfaces: The RISE-6G Perspective," 2021 Joint European Conference on Networks and Communications & 6G Summit (EuCNC/6G Summit), Porto, Portugal, 2021, pp. 562-567, doi: 10.1109/EuCNC/6GSummit51104.2021.9482474. Available at: https://arxiv.org/pdf/2104.06265.pdf.
*	[SAI+21]	N. Shlezinger, G. C. Alexandropoulos, M. F. Imani, Y. C. Eldar, and D. R. Smith, “Dynamic metasurface antennas for 6G extreme massive MIMO communications,” IEEE Wireless Commun., vol. 28, no. 2, pp. 106–113, Apr. 2021. Available at: https://arxiv.org/pdf/2006.07838.pdf.
	[SDE+19]	N. Shlezinger, O. Dicker, Y. C. Eldar, I. Yoo, M. F. Imani, and D. R. Smith, “Dynamic metasurface antennas for uplink massive MIMO systems,” IEEE Trans. Commun., vol. 67, no. 10, pp. 6829–6843, Oct. 2019.
*	[SVK+23]	H. L. dos Santos, C. J. Vaca-Rubio, R. Kotaba, Y. Song, T. Abrao, and P. Popovski “EMF Exposure Mitigation in RIS-Assisted Multi-Beam Communications”, submit-ted to ICC 2023, available https://arxiv.org/abs/2305.05229.
	[TFC+17]	B. Thors, A. Furuskär, D. Colombi and C. Törnevik, "Time-Averaged Realistic Maximum Power Levels for the Assessment of Radio Frequency Exposure for 5G Radio Base Stations Using Massive MIMO," in IEEE Access, vol. 5, pp. 19711-19719, 2017, doi: 10.1109/ACCESS.2017.2753459.
	[TP16]	F. Talebi and T. Pratt, "Channel Sounding and Parameter Estimation for a Wideband Correlation-Based MIMO Model," in IEEE Transactions on Vehicular Technology, vol. 65, no. 2, pp. 499-508, Feb. 2016, doi: 10.1109/TVT.2015.2404571.
	[VAT18]	E. Vlachos, G. C. Alexandropoulos and J. Thompson, "Massive MIMO Channel Estimation for Millimeter Wave Systems via Matrix Completion," in IEEE Signal Processing Letters, vol. 25, no. 11, pp. 1675-1679, Nov. 2018, doi: 10.1109/LSP.2018.2870533.
	[VAT19]	E. Vlachos, G. C. Alexandropoulos and J. Thompson, "Wideband MIMO Channel Estimation for Hybrid Beamforming Millimeter Wave Systems via Random Spatial Sampling," in *IEEE Journal of Selected Topics in Signal Processing*, vol. 13, no. 5, pp. 1136-1150, Sept. 2019, doi: 10.1109/JSTSP.2019.2937633.
	[VCA+18]	Y. Vahabzadeh, N. Chamanara, K. Achouri and C. Caloz, "Computational Analysis of Metasurfaces," in IEEE Journal on Multiscale and Multiphysics Computational Techniques, vol. 3, pp. 37-49, 2018, doi: 10.1109/JMMCT.2018.2829871.
	[VGT14]	F. W. Vook, A. Ghosh and T. A. Thomas, "MIMO and beamforming solutions for 5G technology," 2014 IEEE MTT-S International Microwave Symposium (IMS2014), Tampa, FL, USA, 2014, pp. 1-4, doi: 10.1109/MWSYM.2014.6848613.
	[W+11]	M. Wang et al., "Evaluation and Optimization of the Specific Absorption Rate for Multiantenna Systems," in IEEE Transactions on Electromagnetic Compatibility, vol. 53, no. 3, pp. 628-637, Aug. 2011, doi: 10.1109/TEMC.2011.2109005.
	[W+20]	R. Wang et al., "Enabling Super-Resolution Parameter Estimation for mm-Wave Channel Sounding," in IEEE Transactions on Wireless Communications, vol. 19, no. 5, pp. 3077-3090, May 2020, doi: 10.1109/TWC.2020.2970401.
	[WK14]	Z. Wen and H. Kong, “mmWave MIMO channel sounding for 5G,” 1st International Conference on 5G for Ubiquitous Connectivity, Nov. 2014.
	[WZ19]	Q. Wu and R. Zhang, "Joint Active and Passive Beamforming Optimization for Intelligent Reflecting Surface Assisted SWIPT Under QoS Constraints," in IEEE Journal on Selected Areas in Communications, vol. 38, no. 8, pp. 1735-1748, Aug. 2020, doi: 10.1109/JSAC.2020.3000807. arXiv:1910.06220, 2019.
	[WZ20]	Q. Wu and R. Zhang, "Weighted Sum Power Maximization for Intelligent Reflecting Surface Aided SWIPT," in IEEE Wireless Communications Letters, vol. 9, no. 5, pp. 586-590, May 2020, doi: 10.1109/LWC.2019.2961656.
*	[XYH+23]	Jindan Xu, Chau Yuen, Chongwen Huang, Naveed Ul Hassan, George C. Alexandropoulos, Marco Di Renzo, Merouane Debbah, “Reconfiguring Wireless Environment via Intelligent Surfaces for 6G: Reflection, Modulation, and Security,” in ArXiv, 2023 arXiv:2208.10931 (SCIENCE CHINA. Accepted) Available at: https://arxiv.org/pdf/2208.10931.pdf.
	[XZY+19]	B. Xu, K. Zhao, Z. Ying, D. Sjöberg, W. He and S. He, "Analysis of Impacts of Expected RF EMF Exposure Restrictions on Peak EIRP of 5G User Equipment at 28 GHz and 39 GHz Bands," in IEEE Access, vol. 7, pp. 20996-21005, 2019, doi: 10.1109/ACCESS.2019.2897271.

*	[YIP22-1]	Y. Yu, R. Ibrahim and D. -T. Phan-Huy, "EMF-Aware MU-MIMO Beamforming in RIS-Aided Cellular Networks," GLOBECOM 2022 - 2022 IEEE Global Communications Conference, Rio de Janeiro, Brazil, 2022, pp. 2340-2345, doi: 10.1109/GLOBECOM48099.2022.10001691. Available at: https://arxiv.org/pdf/2209.14785.pdf.
*	[YIP22-2]	Y. Yu, R. Ibrahim and D. -T. Phan-Huy, "Dual Gradient Descent EMF-Aware MU-MIMO Beamforming in RIS-Aided 6G Networks," 2022 20th International Symposium on Modeling and Optimization in Mobile, Ad hoc, and Wireless Networks (WiOpt), Torino, Italy, 2022, pp. 383-390, doi: 10.23919/WiOpt56218.2022.9930548. Available at: https://arxiv.org/pdf/2210.00766.pdf.
*	[YXA+21-1]	J. Xu, L. You, G. C. Alexandropoulos, J. Wang, W. Wang and X. Gao, "Dynamic Metasurface Antennas for Energy Efficient Uplink Massive MIMO Communications," 2021 IEEE Global Communications Conference (GLOBECOM), Madrid, Spain, 2021, pp. 1-6, doi: 10.1109/GLOBECOM46510.2021.9685389. Available at: https://arxiv.org/pdf/1901.01458.pdf.
*	[YXA+21-2]	L. You, J. Xu, G. C. Alexandropoulos, J. Wang, W. Wang and X. Gao, "Energy Efficiency Maximization of Massive MIMO Communications With Dynamic Metasurface Antennas," in IEEE Transactions on Wireless Communications, vol. 22, no. 1, pp. 393-407, Jan. 2023, doi: 10.1109/TWC.2022.3194070. Available at: https://arxiv.org/pdf/2106.09442.pdf.
*	[Z+21]	A. Zappone, M. Di Renzo, F. Shams, X. Qian and M. Debbah, "Overhead-Aware Design of Reconfigurable Intelligent Surfaces in Smart Radio Environments," in IEEE Transactions on Wireless Communications, vol. 20, no. 1, pp. 126-141, Jan. 2021, doi: 10.1109/TWC.2020.3023578. Available at : https://arxiv.org/pdf/2003.02538.pdf.
	[ZHL14]	H. Zhou, L. M. Huie and L. Lai, "Secret Key Generation in the Two-Way Relay Channel With Active Attackers," in IEEE Transactions on Information Forensics and Security, vol. 9, no. 3, pp. 476-488, March 2014, doi: 10.1109/TIFS.2014.2301233.
*	[ZR22]	A. Zappone and M. D. Renzo, "Energy Efficiency Optimization of Reconfigurable Intelligent Surfaces With Electromagnetic Field Exposure Constraints," in IEEE Signal Processing Letters, vol. 29, pp. 1447-1451, 2022, doi: 10.1109/LSP.2022.3181532. Available at: https://arxiv.org/pdf/2104.06283.pdf.
*	[ZRF+22]	A. Zappone, M. D. Renzo, and R. K. Fotockt,"Surface-Based Techniques for IoT Networks: Opportunities and Challenges" in Reseachgate, 2022, DOI: 10.1109/IOTM.001.2200170.
*	[ZRS+21]	A. Zappone, M. Di Renzo, F. Shams, X. Qian, and M. Debbah, "Overhead-Aware Design of Reconfigurable Intelligent Surfaces in Smart Radio Environments," in IEEE Transactions on Wireless Communications, vol. 20, no. 1, pp. 126-141, Jan. 2021, doi: 10.1109/TWC.2020.3023578. Available at: https://arxiv.org/pdf/2003.02538.pdf.